In silico microfluidic chip design to mimic microbial lifelines

LM3901: Master Thesis Project

Loulotte Waling
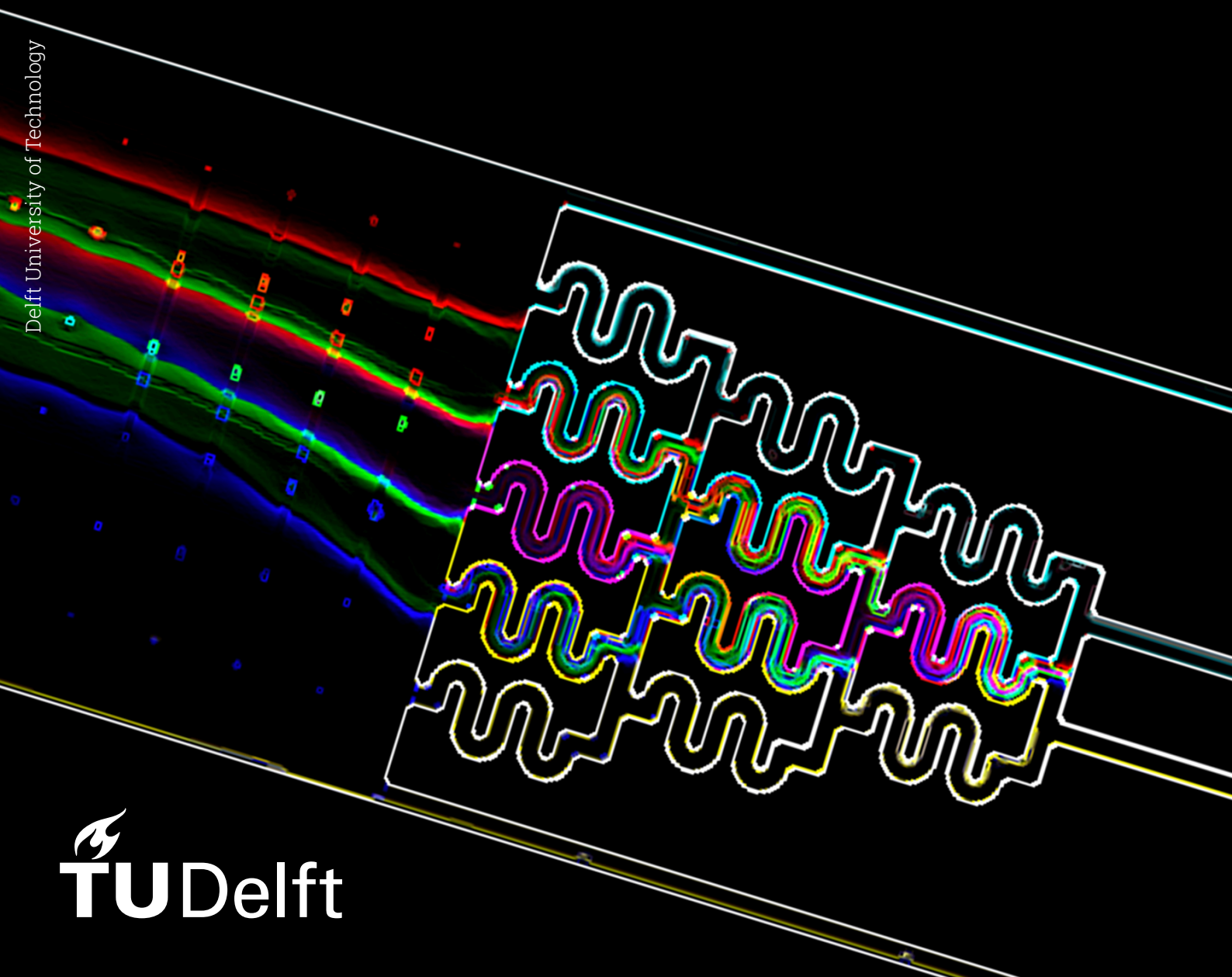
TUDelft

In silico microfluidic chip design to mimic microbial lifelines

by

Loulotte Waling

to obtain the degree of Master of Science
at the Delft University of Technology,
to be defended publicly on Monday June 1, 2023 at 09:30 AM.

TUDelft

Preface

With this thesis, titled *'In silico microfluidic chip design to mimic microbial lifelines'*, I am concluding an exciting seven-year period of studying at TU Delft and Leiden University. During this time, I have had the opportunity to meet amazing people that I can only hope to stay friends with for many more years.

This thesis was conducted with the Cees Haringa (CASE) group in the bioprocess engineering section of the Biotechnology Department at TU Delft. Before leaving you to read my thesis, I would like to thank my supervisor and prinicipal investigator Cees Haringa for all his help and supervision throughout the past months. I have very much enjoyed our interesting discussions on my thesis and of course his stories (and Terschellinger pofkes!) during the BPE coffee breaks. Furthermore, I would like to extend my gratitude to professors Volkert van Steijn and Rinke van Tatenhove-Pel for their discussions and the useful insights I gained during our meetings, which have resulted in the microfluidic prototype discussed in this work. Also, I have had the opportunity to fabricate and test this prototype in the laboratory. For this, I would like to thank Albert Santoso for all his time and effort he put into the fabrication of my master wafer and his time teaching me and supervising me with all experimental work. Regarding experimental work, I would also like to thank Kristin David, who offered her expertise which has been of great help and Tiago Picanço Castanheira da Silva for his useful insights into working with PDMS and microfluidic chip setups in the laboratory. I would also like to thank Ramon van Valderen and Rik Volger who have given valuable feedback during the final stages of writing. Finally, I would like to thank everyone in the CASE and BPE group and my friends in other sections at TNW Zuid for our daily 'bakkies' as well as my family and other friends for their support during the past months.

Loulotte Waling
Delft, May 2023

Abstract

In recent years, biotechnological processes have gained increased interest due to their potential for high-value compound production and waste recycling. This shift towards biotechnology is driven by global challenges such as food security, climate change, and the transition to renewable resources. To address the limitations of large-scale fermentations, scale-down approaches have been recommended to minimize microbial performance losses during scale-up procedures. Computational fluid dynamics (CFD) coupled with omics-based technologies offer valuable insights into the environmental and intra-cellular lifelines of cells. However, current laboratory-scale setups have certain limitations, emphasizing the need for dynamic microfluidic single-cell cultivation (dMSCC) devices. These devices enable the analysis of single-cell behavior in dynamic environments with high temporal resolution.

This thesis focuses on improving the amplitude control while maintaining temporal resolution in dMSCC devices. A new dMSCC device design was analyzed using a 2D model, which was experimentally validated. The results demonstrated that the design mechanism effectively generated concentration profiles resembling discrete and smooth lifelines, albeit with a relatively high response time (30 seconds). A mesh independence study indicated minimal deviations (2 %) in results for different mesh refinements, while complex geometric structures introduced greater variations.

The experimental validation of the 2D COMSOL Multiphysics model highlighted discrepancies between the experimental data and model predictions, both at the outlets of the microfluidic concentration gradient generator (μCGG) and inside the chamber (RMSE=0.1-0.75; >10% of experimental data). However, the observed trends of the concentration profiles inside the chamber were well-captured. Optimization studies were conducted based on these findings, leading to valuable conclusions. Narrowing the chamber width increased the chip's response time. Moreover, increasing the space between μCGG outlets as well as increasing fluid velocity inside the μCGG (while keeping the maximum velocity constant) improved gradient width. The latter approach is preferred to maintain temporal resolution. A comparison between COMSOL Multiphysics (RMSE=0.14) and Ansys Fluent (RMSE=0.15) models revealed that Ansys Fluent better captures experimental trends but has lower prediction accuracy.

Further investigations involved a Design of Experiments (DoE), which indicated that the current μCGG design is suitable for fluid velocities preferably lower than $1 \cdot 10^{-5}$ m/s and tracers with high diffusion coefficients. These conclusions provide insights into optimizing dMSCC devices and contribute to the broader understanding of mimicking microbial lifelines.

Contents

List of Figures

List of Tables

Nomenclature

Abbreviations

Abbreviation	Definition
ND	N dimensional
CAD	Computer-aided design
CFD	Computational fluid dynamics
FD	Finite differences
FEM	Finite element method
IPCC	Intergovernmental Panel on Climate Change
LSM	Laser scanning microscopy
MGC	Monolayer growth chamber
MSBR	Miniaturized stirred bioreactors
(d)MSCC	(Dynamic) microfluidic single-cell cultivation
NS	Navier Stokes
ODE	Ordinary differential equation
PDE	Partial differential equation
PDMS	Polydimethylsiloxane
RMSE	Root mean square error
STR	Stirred tank reactor
WF	Wide field
μCGG	Microfluidic concentration gradient generator

Symbols

Symbol	Definition	Unit
A_c	Cross-sectional area	m^2
c_i	Concentration of solute i	mol/m^3
c_0	Initial concentration	mol/m^3
D	Diameter	m
D_m	Diffusion coefficient	m^2/s
D^*	Aris-Taylor dispersion coefficient	m^2/s
D_{ax}	Axial dispersion coefficient	m^2/s
d_H	Hydraulic diameter	m
f	Frequency	Hz
F	Load vector	
I	Identity matrix	
J_i	Flux of solute i	kg/(m^2 s)
K	Stiffness matrix	
K_s	Half-velocity constant	mol/m^3
$k1, k2$	Fraction constants	
L	Length	m
L_{plug}	Amount or length of dispersion	m
n	Normal vector	
p	Pressure	Pa
p_0	Initial pressure	Pa
$\hat{p_0}$	Reference pressure	Pa

Symbol	Definition	Unit
P	Normalized ratio between maximum & minimum concentration	
P_w	Wetted perimeter	m
R	Radius	m
$r_{i,max}$	Maxmimum conversion rate of solute i	mol / (m^3 s)
S	Scalar	
$t_{consumption}$	Characteristic time consumption	s
$t_{convection}$	Characteristic time convection	s
$t_{diffusion}$	Characteristic time diffusion	s
t_{plug}	Characteristic time axial dispersion	s
u	Average velocity	m/s
u_{max}	Maximum velocity	m/s
u_{plug}	Average velocity of the dispersed volume	m/s
u_x, u_y	Average velocity in the x- and y-direction respectively	m/s
U_0	Velocity at the inlet	m/s
$u0$	Velocity at the inlets of the μCGG	m/s
$u1, u2$	Velocity at the top and bottom inlet respectively	m/s
z_{o_i}	Observed value	
z_{f_i}	Predicted value	
δ	Penetration depth	m
μ	Dynamic viscosity	Pa s
ρ	Density	kg/m^3
$\phi0$	Flow rate at the inlets of the μCGG	μL/min or nL/min
$\phi1, \phi2$	Flow rate at the top and bottom inlet respectively	μL/min or nL/min

Dimensionless numbers

Symbol	Name	Description	Equation
Re	Reynolds	Ratio of inertial forces and viscous forces	$\dfrac{\rho u L}{\mu}$

Introduction

1.1. Scale up of bioprocesses and the scale down approach

In recent years, biotechnological processes have gained increased interest as they can be used for the production of high-value compounds and recycling of waste (Bahnemann and Grünberger, 2022, Gupta et al., 2017). Furthermore, a global trend is observed where biotechnological approaches are preferred over chemical processes to tackle worldwide challenges such as food security and climate change (Timmis et al., 2017) and to replace fossil resources with renewable bio-based alternatives (Noorman and Heijnen, 2017). This is highlighted by a special report from the Intergovernmental Panel on Climate Change (IPCC), where biotechnology is mentioned as one of the key industries that will assist in reaching the United Nations' goals for 2050, which were set to decelerate climate change (de Coninck et al., 2022).

These biotechnological processes often involve large-scale fermentations to commercialize target products. During scale-up procedures from lab to industrial scale, loss of microbial performance is very common and may result in great economic losses (Oosterhuis, 1984). These performance losses are often caused by non-ideal mixing at large scale, causing concentration gradients throughout the reactor volume. Therefore, there is a need for methods to minimize the risks of microbial performance loss (Delvigne et al., 2017, Noorman and Heijnen, 2017).

The scale-down approach is highly recommended as a tool to minimize the negative impacts of scale-up procedures. This approach includes four stages: (i) the analysis of large-scale conditions, (ii) simulation of these conditions at a laboratory scale, (iii) testing in this laboratory setting to improve process parameters, set-up, and strains, and (iv) integration of new findings at large-scale (Oosterhuis, 1984, Delvigne et al., 2017). Computational fluid dynamics (CFD) may be used to analyze the different conditions present in large bioreactors. In addition, Euler-Lagrange simulations can be used to yield microorganisms' trajectories through the fluid. These microbial trajectories can then be used to assess the environmental conditions that single cells are subjected to in large bioreactors. The profiles of the environmental conditions over time are called environmental lifelines. Since cells are able to store metabolites and macromolecules for short periods of time, these environmental profile models are ideally coupled to models that represent the internal metabolism of cells. These coupled concentration profiles observed inside a cell are called intracellular lifelines. This yields a complete overview of the conditions that cells encounter during fermentation (Haringa et al., 2016, Haringa et al., 2017, Delvigne et al., 2017, Blöbaum et al., 2022).

To identify the effects of these (simulated) conditions on cell culture, ideally a large set of conditions is analyzed with laboratory-scale experiments. This can be done with a range of different laboratory set-ups, often containing one or more stirred tank reactors (STRs) (Täuber et al., 2022, Delvigne et al., 2017). During and after running such experiments, omics-based technologies can be applied to identify the mechanisms that cause reduced functionality at a large scale. Based on these results, targeted improvement of the strain and reactor design can be used to reduce and/or resolve the issues (Delvigne et al., 2017).

Conducting these laboratory-scale experiments to identify the limiting process(es) at a large scale can be extremely beneficial to improve production yields. Small-scale STRs used to be the conventional bioreactor setup for these scale-down experiments. However, in recent years, advancements in equipment and protocols have been made to reduce costs and increase throughput. These include set-ups using shake flasks, miniaturized stirred bioreactors (MSBRs), and microtiter plates (Delvigne et al., 2017, Tajsoleiman et al., 2019, Formenti et al., 2014). Furthermore, advanced pump systems have been developed to establish oscillations of multiple parameters in these milliliter-scale bioreactor systems (Gudiño, 2022). However, these scale-down bioreactor systems have a number of limitations. These systems only allow for bulk measurements, thereby limiting our understanding of the influence of lifelines on the single cell (Dusny and Grünberger, 2020). Furthermore, the oscillation profiles of certain parameters cannot be dissociated and the time scale is in the minute to the larger-second range (Formenti et al., 2014 Täuber and Grünberger, 2023).

The use of dynamic microfluidic single-cell cultivation (dMSCC) systems could pose a solution to these limitations of current scale-down reactor setups. dMSCC devices allow for the analysis of cellular behavior and physiological properties during the cultivation of single cells or microcolonies in dynamic environments with high temporal resolution (Täuber and Grünberger, 2023). The following sections, therefore, aim to address the overarching research question of this thesis:

What is necessary to mimic environmental lifelines at a microfluidic scale?

1.2. Mimicking microbial lifelines using microfluidics

Recent studies have investigated the effect of both static and dynamic environments on single-cell and microcolony cultivation with novel (d)MSCC devices (Leygeber et al., 2019). Here, cell traps with a range of different geometries were used, allowing single cells or microcolonies to grow in different sizes ranging from 0D to 3D (Grünberger et al., 2014, Ho et al., 2019). Most dMSCC studies investigated the fundamental behavior of cells, such as aging, gene expression and regulation, and growth behavior, fluctuating environmental conditions between two parameters within seconds or minutes. Only a few dMSCC devices have been developed for the analysis of bioprocess-relevant conditions (Täuber and Grünberger, 2023). These studies alternated between two discrete glucose concentration levels and three discrete pH levels respectively, with fluctuations ranging between 5 seconds to 20 minutes (Ho et al., 2022, Täuber et al., 2022). However, these devices are still subject to improvement, as they are not yet able to establish simultaneous multi-parameter fluctuations, continuous dynamic profiles, and gas, temperature, light, and pressure fluctuations. Furthermore, analytic techniques for cell growth and metabolite measurements are still restricted to image-based approaches (Täuber and Grünberger, 2023).

This work will focus on improving the amplitude control of the dynamic profiles while maintaining the high temporal resolution that is achieved by the current dMSCC devices. To this end, three subquestions will be addressed:

1. Which dMSCC device design could overcome current limitations with regard to amplitude control?
2. Can a model of the device be used as a proof-of-concept and design optimization tool?
3. Can this model be experimentally validated?

2

Time scale exploration

2.1. Alternative dMSCC device designs

Initially, three different designs were considered that could overcome amplitude control limitations while maintaining the frequency control of current dMSCC designs. The first design is based on mixing through a T-junction and possibly a serpentine channel to improve mixing (Haringa et al., 2018) (Figure 2.1a). A variation to this design is the dial-a-wave junction (Kaiser et al., 2018, Täuber and Grünberger, 2023). The second design is based on injection into a carrier fluid that is compartmentalized by a 'bubble train' (Haringa et al., 2018) (Figure 2.1b). The third design was ideated during this thesis in close collaboration with associate professor Dr. V. van Steijn[1], assistant professor Dr. R. van Tatenhove-Pel[2], and assistant professor Dr. C. Haringa[3]. This design is based on a microfluidic concentration gradient generator (μCGG) (Giridharan et al., 2012, Sweet et al., 2020), which generates a static gradient. This gradient may be pushed across the chamber by changing fluid velocities at either side of the μCGG, similar to the concept explored by Jeon et al. (2000) (Figure 2.1c). To identify which of these three design concepts is best at overcoming the amplitude control limitations, a regime analysis was conducted to identify the time scales of main processes inside the dMSCC devices.

(a) T-junction   **(b)** Bubble train injection   **(c)** Dynamic μCGG
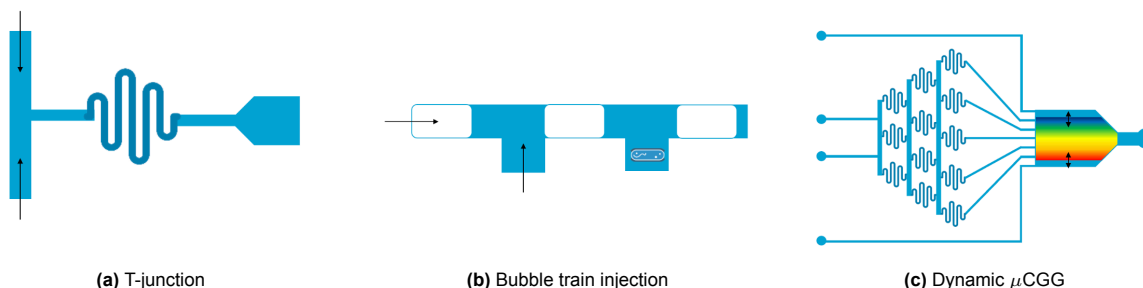
Figure 2.1: The three design concepts that are considered in this work. The T-junction and bubble train injection designs are adapted from Haringa et al., 2018. The dynamic μCGG design is a combination of concepts found in literature and was ideated in collaboration with Dr. Van Steijn, Dr. Van Tatenhove-Pel, and Dr. Haringa.

2.2. Regime analysis

To get a better understanding of the sub-processes inside a dMSCC device, the time-scales for convection, axial dispersion, diffusion, and substrate consumption were investigated. Based on this analysis, better informed design choices can be made.

2.2.1. Convection and axial dispersion

In most (d)MSCC devices, fluid flow, or convection, is established to supply the microorganisms with nutrients (Täuber and Grünberger, 2023). The characteristic time for convection is described by equa-

---

[1]Department of Chemical Engineering, TU Delft
[2]Department of Biotechnology, TU Delft
[3]Department of Biotechnology, TU Delft

tion 2.1 (Heijen et al., 2015), where L is the distance traveled by the fluid and u is the average velocity of the fluid.

$$t_{convection} = \frac{L}{u}$$
(2.1)

In the case of laminar flow, molecular diffusion in the axial direction may occur causing spread of the solute over time. This is called axial dispersion. The characteristic time for axial dispersion in straight channels and pipes is described by equation 2.2 (Heijen et al., 2015), where L_{plug} amount or length of 'smearing' and u_{plug} the velocity of this 'smeared out volume' through the channel. With an expression derived from penetration theory, L_{plug} can be calculated. Here, $t_{convection}$ is the characteristic time for convection and D_{ax} the axial dispersion coefficient (Picioreanu et al., 2019).

$$t_{plug} = \frac{L_{plug}}{u_{plug}} \quad \text{where} \quad L_{plug} = \sqrt{\pi D_{ax} t_{convection}}$$
(2.2)

The axial dispersion coefficient for flow in circular channels can be approximated using equation 2.3 for the Aris-Taylor dispersion coefficient D^* (Fogler, 2017). Here, u is the average velocity of the fluid, R is the radius of the channel, and D_m is the diffusion coefficient of solute A in solvent B. For this equation, $D^* \equiv D_{ax}$ may be assumed when considering a laminar flow regime.

$$D^* = D_m + \frac{u^2 R^2}{48 D_m}$$
(2.3)

A laminar flow regime may be assumed when $Re < 2100$. When $Re > 2100$, the flow may be considered turbulent and, for $Re << 1$, a creeping flow is considered. The equation for Reynolds number Re is given by equation 2.4, where ρ is the density of the fluid, u the average velocity of the fluid, d_H the hydraulic diameter, and μ the dynamic viscosity (Fogler, 2017). The hydraulic diameter can be calculated with $d_H = 4A_c/P_w$ with the wetted perimeter P_w and constant cross-sectional area A_c. Consequently, in case of a circular tube the hydraulic diameter is equal to the diameter ($d_H = D$).

$$Re = \frac{\rho u d_H}{\mu}$$
(2.4)

Often the channels in microfluidic devices do not have a tubular shape but are rectangular or trapezoidal, because of the commonly used soft lithography fabrication technique (Tang and Whitesides, 2010). Therefore, the Aris-Taylor expression for axial dispersion should be adjusted to apply to other geometries. Moreau et al. (2017) report a relation for the axial dispersion coefficient in the case of laminar flow in non-circular pipes, which is similar to the Aris-Taylor relation (equation 2.5). Here, R is substituted for d_H, to make the equation applicable to other geometries. It should be noted that this relation is only valid when the characteristic time for axial dispersion is much higher than that for tangential diffusion. However, in this work, it is assumed that the inlet concentration is homogeneous, thus tangential diffusion should not affect the system.

$$D_{ax} = D_m + \frac{u^2 d_H^2}{192 D_m}$$
(2.5)

Depending on the geometry of the microfluidic channel, D_{ax} can be calculated with either equation 2.3 or 2.5. In turn, this can be used to calculate the characteristic time for axial dispersion (equation 2.2).

Axial dispersion is a process that only occurs when $Re < 2100$. To characterize the flow in microfluidic channels, the Reynolds number was calculated for different fluid velocities (Figure 2.2a) and different hydraulic diameters (Figure 2.2b). Here, it was assumed that the solute was highly diluted in water, thus $\rho = 1000$ kg/m^3 and $\mu = 1$ mPa s. For the calculations of Re versus u (Figure 2.2a) a hydraulic diameter of 100 μm was assumed (Ho et al., 2019). For the calculations of Re versus d_H (Figure 2.2b) a fluid velocity of $6.66 \cdot 10^{-3}$ m/s was assumed (Ho et al., 2019).

Figure 2.2a shows that for a fluid velocity ranging between 0 m/s and 0.010 m/s with $d_H = 100$ μm, Re does not exceed 1.0. Figure 2.2b shows that for a hydraulic diameter ranging between 0 μm and 250 μm, Re does not exceed 1.50. This suggests that, under these conditions, the flow regime is either creeping or laminar, and axial dispersion is likely to occur.
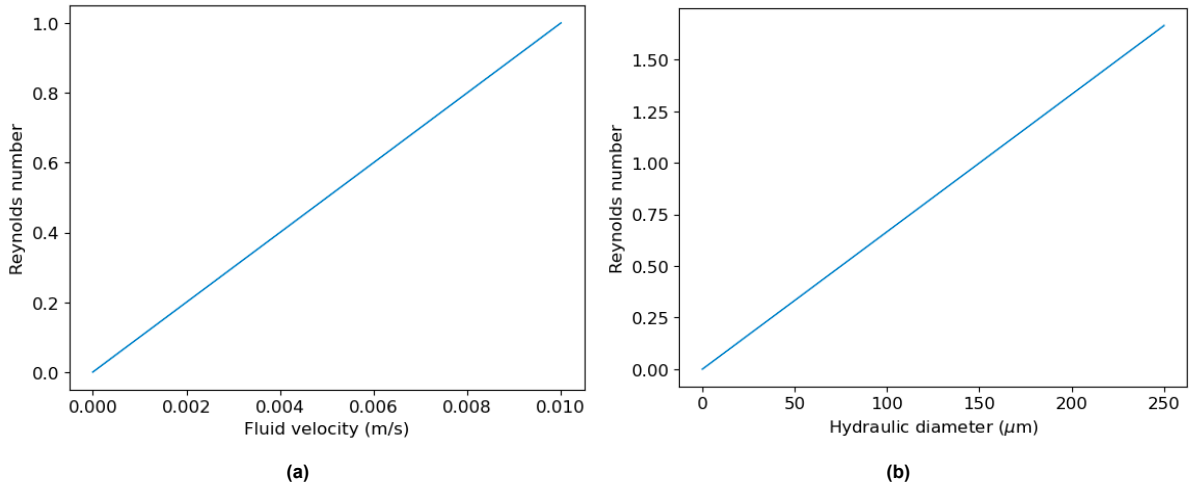
Figure 2.2: Characterization of flow regime. a) Reynolds number versus the fluid velocity with a constant hydraulic diameter ($d_H = 100$ μm). b) Reynolds number versus the hydraulic diameter with a constant fluid velocity ($u = 6.66 \cdot 10^{-3}$ m/s).

To analyze the effect of axial dispersion on solute transport, the characteristic times of convection and axial dispersion were calculated and compared. For the calculation of the characteristic time for convection (equation 2.1) and axial dispersion (equation 2.2), three different fluid velocities ($1.00 \cdot 10^{-2}$ m/s, $6.66 \cdot 10^{-3}$ m/s (Ho et al., 2019), and $1.00 \cdot 10^{-3}$) were compared over a channel with a length of 1000 μm and hydraulic diameter of 250 μm respectively. The calculation of the characteristic time for axial dispersion is dependent on the characteristic time for convection. Therefore, in these calculations, the convection time was taken at $L = 1000$ μm for each of the three velocities. The characteristic time for convection increases when the distance of the channel increases, and decreases when the fluid velocity increases (Figure 2.3a). It ranges from ranges between 0 s to 1.2 s, depending on the fluid velocity and channel length. The characteristic time for axial dispersion increases when the hydraulic diameter increases and also decreases when the velocity increases (Figure 2.3b). It ranges between 0 s to 1.3 s, depending on the hydraulic diameter and fluid velocity. Thus, the time scales for both processes are very similar, meaning that axial dispersion highly affects the concentration of the solute. A solution could be to decrease the hydraulic diameter, as this reduces the characteristic time for axial dispersion. However, the time scales will remain in a similar order of magnitude.
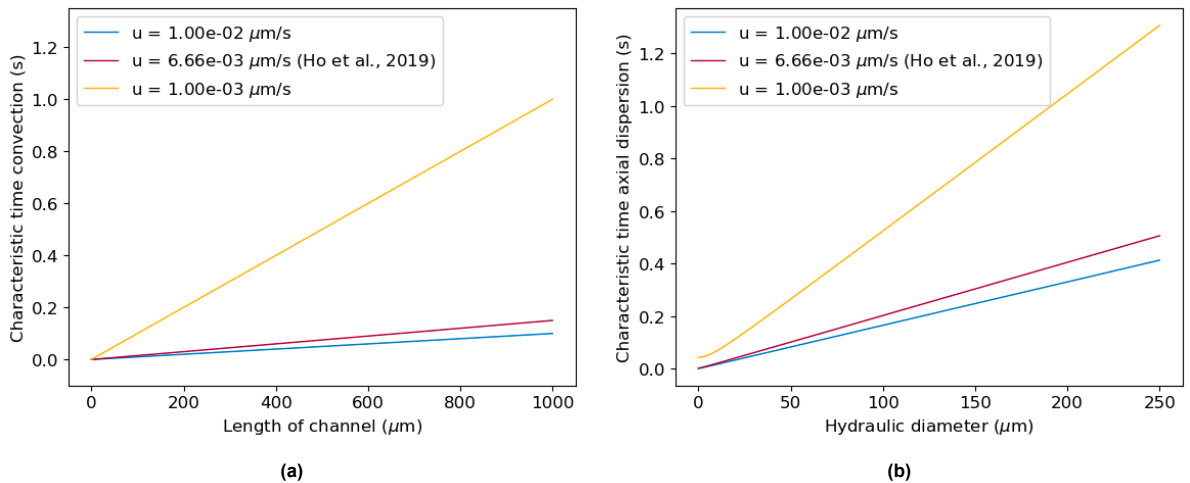
Figure 2.3: a) The characteristic time for convection versus the channel length for three different velocities. b) The characteristic time for axial dispersion versus the hydraulic radius at $L = 1000$ μm.

A 1D time-dependent convection-dispersion model was set up to get a better understanding of the impact of axial dispersion on the solute concentration observed at a given location inside a straight microfluidic channel. This model is given by equation 2.6, which describes a time-dependent partial

differential equation (PDE) system. This PDE system determines the change of concentration of solute i over time and distance due to convection and axial dispersion. Details about this 1D model can be found in Appendix A.

$$\frac{\partial c_i}{\partial t} = D_{ax}\frac{\partial^2 c_i}{\partial x^2} - u\frac{\partial c_i}{\partial x} \tag{2.6}$$

Figure 2.4 shows the results of the 1D model, where at $t = 0s$, 1 μg of glucose is injected into the system. This inlet concentration is modeled after a Dirac pulse (similar to the approach of Silavwe et al. (2019)). The figure shows the solute concentration observed over time at a given location inside the channel. Indeed a decrease in peak height is observed: as the peak moves through the channel, the solute spreads due to axial dispersion. This effect of axial dispersion should be taken into account (and corrected for) when considering the T-junction (Figure 2.1a) design since this design would carry the signal in a single phase through a channel to the microorganism(s).
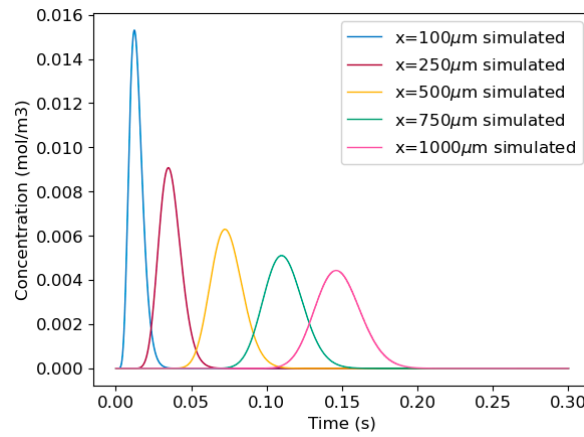
Figure 2.4: The results of the 1D time-dependent convection-dispersion model. At $t = 0$, 1 μg glucose is injected into the microfluidic channel. The model shows the concentration distribution over time observed at five locations (100μm, 250μm, 500μm, 750μm, and 1000μm) inside the channel.

2.2.2. Diffusion
In most dMSCC devices, the movement of solutes into and out of the cultivation chamber is a diffusion-driven process. Furthermore, in other parts of the chip, diffusive effects may play a role in the efficiency of the mechanism of the chip. The characteristic time for diffusion is also derived from penetration theory and given by equation 2.7, where δ is the penetration depth (Heijen et al., 2015).

$$t_{diffusion} = \frac{\delta^2}{\pi D_m} \tag{2.7}$$

Figure 2.5 shows the characteristic time for diffusion versus the penetration depth. The characteristic times for convection and axial dispersion were $\sim$1 second, thus it would be desirable to keep the time required for diffusion below that required for convection and axial dispersion. Therefore, the dimensions of the locations where the transport mechanism relies on diffusion should be smaller than 40 μm (Figure 2.5, dashed grey line). For example, the penetration depth of the cultivations chambers should not exceed 40 μm. If larger chambers are desired, one could select a design with openings on both sides of the chamber to reduce the penetration depth, similar to designs used by Ho et al. (2022) and Täuber et al. (2022).
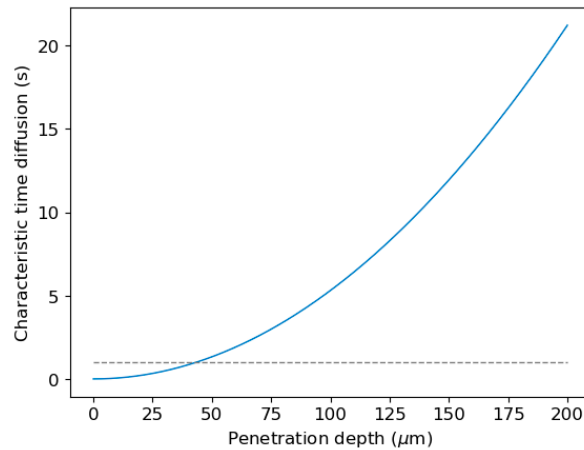
Figure 2.5: Characteristic time for diffusion. The grey dashed line indicates the 1-second mark. Above this line, the characteristic time for diffusion becomes larger than the characteristic time for convection and axial dispersion.

2.2.3. Conversion

Conversion is a sub-process that may describe reactions, substrate uptake, and (by-)product and biomass formation. To get an indication of the time required for the conversion of the substrate, the characteristic time for substrate consumption can be determined with equation 2.8 (Heijen et al., 2015).

$$t_{consumption} = \frac{\Delta c_s}{r_{max}} \tag{2.8}$$

Here, Δc_s is the change in substrate concentration. If unknown, the maximum uptake rate, $r_{s,max}$, can be determined with Monod's equation (2.9) from experimental data. Here, r_s is the substrate uptake rate, and K_s is the 'half-velocity' constant (Picioreanu, 2020).

$$r_s = r_{s,max}\frac{c_s}{c_s + K_s} \tag{2.9}$$

Figure 2.6 clearly demonstrates that substrate consumption is a slow process when compared to convection, axial dispersion, and even diffusion (when considering $\delta < 40\mu$m). Therefore, continuous systems would be preferred over batch or fed-batch systems when a dynamic lifeline profile is to be imposed on the microorganism(s). I.e. waiting for the microorganisms to consume all substrate before a new condition can be established would significantly reduce the oscillation capabilities of the dMSCC device. All three designs (Figure 2.1) comply with this requirement for a continuous system.
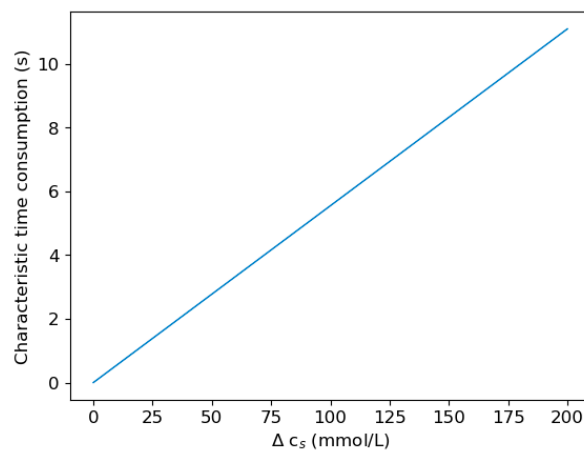
Figure 2.6: Characteristic time for substrate consumption versus an arbitrary substrate concentration difference Δc_s.

2.3. Design choice

To conclude, the time scale exploration showed that convection and axial dispersion have similar characteristic times. A 1D model revealed that indeed convective transport of the concentration profile along a channel inside a microfluidic system impacts the concentration profile observed at the end of such a channel. Furthermore, for diffusive processes, it was found that a penetration depth < 40 μm ensures that the characteristic time for diffusion does not exceed 1 second. This leaves enough room for microorganisms to grow and a larger chamber can even be used when multiple openings to the chamber are considered. Finally, it was found that complete consumption of substrate is a time-consuming process, and therefore continuous systems are preferred over batch or fed-batch systems to mimic lifelines. Taking these limitations and design requirements into account, the three designs (Figure 2.1) can be compared.

The T-junction design relies on diffusive mixing inside a serpentine channel. As some residence time would be required for proper mixing, the serpentine channel should be relatively long. This may result in large effects of axial dispersion on the concentration profile resulting in frequency limitations of the lifeline profile.

To avoid this, the bubble train injection design could be used, where the separation of the phases would stop the axial dispersion in the channel. However, this design does not allow for the production of a smooth lifeline as the concentration 'compartments' are separated by a different phase. Furthermore, if this design is considered, mass transfer may also affect the concentration profile. For the implementation of this bubble train injection design, this should be further investigated.

The dynamic μCGG design does not rely on the convective transport of the profile from the inlet to the cultivation chamber. In stead, the concentration profile is generated at the location of the cultivation chamber. Therefore, the limiting effects of axial dispersion are not relevant for this mechanism. Furthermore, conceptually, this design seems to be able to establish smooth concentration profiles (similar to Täuber et al. (2022) and Ho et al. (2022)). Therefore, this design was chosen to further explore the possibilities of mimicking lifelines at a microfluidic scale.

3

Materials and methods

3.1. The base case model

In collaboration with associate professor Dr. V van Steijn[1], assistant professor Dr. R. van Tatenhove-Pel[2], and assistant professor Dr. C Haringa[3] a new microfluidic chip geometry was ideated that may overcome current amplitude control limitations without compromising oscillation times.

3.1.1. Model set-up

Geometry

A 2D model was set up in COMSOL Multiphysics. The geometry design was drawn with computer-aided design (CAD) software Autodesk AutoCAD, and imported into the 2D model component in COMSOL Multiphysics. The new geometry design consists of a microfluidic concentration gradient generator (μCGG) that has 2 inlets and 5 outlets and has serpentine channels, each with two round bends (similar to μCGG designs by e.g. Jeon et al., 2000 and Sweet et al., 2020) (Figure 3.1). The gradient generator is flanked by a bottom and top inlet. All 7 channels are connected to the large chamber, which design is based on the work by the Grünberger group (Täuber et al., 2020 and Täuber et al., 2022). Inside the chamber, pillars are placed every 500 μm to avoid collapse during experimental work.

Behind the geometry design choices

The μCGG was first designed with the 3DμF web tool, which was developed by the CIDAR lab. This open-source web tool was developed to accelerate the design of microfluidic devices and contains numerous microfluidic channel constructions and components found in the literature (Sanka et al., 2019). The web tool has a function called 'gradient gen', which can be used to create a personalized gradient mixer as it allows for a whole set of parameters to be changed. However, it only creates gradient generators with square bends rather than round bends. Therefore, a gradient mixer was also designed from scratch in AutoCAD that does consist of round bends. Five different μCGG geometries were created: four μCGGs with round bends with 500 μm, 750 μm, 1000 μm, and 1500 μm between the outlets, and one μCGG with square bends with 500 μm between the outlets. The chamber, which connects the inlets and μCGG to the outlet and should eventually host the cultivation chambers, is designed after the microfluidic devices created by the Grünberger group. Six different chambers were designed that have different dimensions corresponding with the μCGG design. Each of these geometries can be found in Appendix B.

Physics, boundary conditions, and assumptions

The flow field is calculated using the laminar flow module from COMSOL Multiphysics. The fluid flow equations for stationary and time-dependent simulations are given in equations 3.2 to 3.5 (see table 3.1). There is no initial fluid velocity field and no initial pressure. Thus, $u_x = u_y = 0$ m/s and $p_0 = 0$ Pa. The boundary conditions that were applied are:

---

[1]Department of Chemical Engineering, TU Delft
[2]Department of Biotechnology, TU Delft
[3]Department of Biotechnology, TU Delft

- The walls are stationary, thus the 'no slip' boundary condition is $u = 0$ m/s.
- At the inlets, a normal inlet velocity is set as $u = -U_0 n$. Three different inlet velocities are defined: $U_0 = u0$, $U_0 = u1$, and $U_0 = u2$. The inlet velocity into the gradient generator ($u0$) is kept constant throughout the base case model simulations. The inlet velocities of the top ($u1$) and bottom ($u2$) inlets may be changed throughout the base case simulations. It is desired to keep the total flux into and out of the chamber constant for analytical purposes. Therefore, the top and bottom inlets are defined as:

$$u1 = k1 \, u_{max} \quad \text{and} \quad u2 = k2 \, u_{max} \quad \text{where} \quad k1 + k2 = 1 \tag{3.1}$$

  Thus, $k1$ and $k2$ are fractions of 1. Also, $u_{max} = 6.66 \cdot 10^{-3}$ m/s (similar to work by Ho et al., 2019) in the base case model.
- The outlet is defined as a pressure-based boundary condition. For both stationary and time-dependent studies $[-pI + K]n = -\hat{p_0}n$ where $\hat{p_0} \leq p_0$ and $p_0 = 0$ Pa. Here, backflow is suppressed.

The transport of species is then calculated based on this laminar flow field, with COMSOL's transport of diluted species module. For the stationary and time-dependent simulations, equations 3.8 to 3.9 were applied. The initial concentration in the chamber is $c_0 = 0$ mol/m^3. The boundary conditions regarding the transport of species that were applied in the simulations are as follows:

- The walls of the channels and chamber are assumed not to be permeable for the fluid components, thus the 'no flux' transport boundary condition is $-n \, J_i = 0$.
- The inlet concentrations at the top two inlets are set at the minimum $c_{min} = 0$ mol/m^3. The inlet concentrations at the bottom two inlets are set at the maximum $c_{max} = 200$ mol/m^3, similar to the work by Ho et al., 2019.
- The outlet is also defined as a 'no flux' boundary, where $J_i = n \cdot D_i \nabla c_i = 0$ for both stationary & time-dependent studies.

In all cases, the 3D geometry of the dMSCC was simplified to a 2D model, because the geometry is symmetric along the z-axis and a laminar flow may be assumed ($Re < 2100$ under the conditions of the base case model). Unless otherwise indicated, it is assumed that the solvent is water and the solute is glucose, a common substrate for microorganism growth. Furthermore, it is assumed the glucose is highly diluted, so $\mu = 1 \cdot 10^{-3} Pas$ (Hille, 2001) and $\rho = 1000$ kg/m^3 (Philips et al., 2009), similar to pure water. The diffusion coefficient of glucose in water is $D = 6 \cdot 10^{-10}$ m^2/s (Stein, 1990).

Mesh
COMSOL Multiphysics creates a mesh for the domain with a physics-controlled finite element method. Unless otherwise indicated, the 'normal' element size mesh is selected resulting in a mesh containing 165698 domain elements and 6467 boundary elements in this base case geometry. Figure 3.1 gives a graphic overview of the model set-up of the base case.

Discretization schemes and solver configurations
The discretization scheme that was used for the laminar flow equations is according to the linear P1+P1 method (COMSOL, 2022c). The discretization scheme that was used for the transport of species equations is also according to the linear method (COMSOL, 2022c). Increasing the complexity of the discretization scheme (i.e. by going from a linear to a quadratic or cubic problem) may increase accuracy but also severely increases computation time. In this thesis, only linear discretization schemes were used since proper convergence and results were thereby achieved. Hence, there was no necessity to increase complexity.

For both stationary and time-dependent studies, COMSOL Multiphysics couples the iterative Newton-Raphson method with the direct PARDISO solver. The PARDISO algorithm solves the linear system of equations that arises at each iteration of the Newton method. This coupled algorithm can take advantage of the efficient solving capabilities of the direct PARDISO method, while still maintaining the robustness and convergence properties of the Newton method (COMSOL, 2022a, COMSOL, 2022b). The relative tolerance of the error between iterations is set at 0.001.

Table 3.1: Overview of the flow and transport equations applied in the 2D model in COMSOL Multiphysics. In the laminar flow equations, ρ is the density of the fluid, u is the velocity vector, p is the pressure vector, I is the identity matrix used to store convection terms, K is the stiffness matrix used to store the viscous terms, and F the load vector used to store external forces such as the gravity (not applicable here), pressure gradients, etc. In the transport equations, c_i is the concentration of component i, J_i is the flux of component i, u is the velocity vector, R_i is a sink factor in case of reactions, conversions, etc. (not applicable here), and D_i is the diffusion coefficient of component i in the solvent.

Physics	Study type	Equation
Laminar flow	Stationary	

$$\rho(u \cdot \nabla)u = \nabla \cdot [-pI + K] + F \qquad (3.2)$$

$$\rho \nabla \cdot u = 0 \qquad (3.3)$$

Laminar flow	Time-dependent	

$$\rho \frac{\partial u}{\partial t} + \rho(u \cdot \nabla)u = \nabla \cdot [-pI + K] + F \qquad (3.4)$$

$$\rho \nabla \cdot u = 0 \qquad (3.5)$$

Transport of diluted species	Stationary	

$$\frac{\partial c_i}{\partial t} + \nabla \cdot J_i + u \cdot \nabla c_i = R_i \qquad (3.6)$$

$$J_i = -D_i \nabla c_i \qquad (3.7)$$

Transport of diluted species	Time-dependent	

$$\frac{\partial c_i}{\partial t} + \nabla \cdot J_i + u \cdot \nabla c_i = R_i \qquad (3.8)$$

$$J_i = -D_i \nabla c_i \qquad (3.9)$$

Post-processing results

Depending on the type of study, either post-processing of the results is done with the COMSOL Multiphysics software, or the raw data is exported and further analyzed using Python or Microsoft Excel. In the materials and methods sections for each study, it is elaborated on which data is evaluated and how this is done.

Figure 3.1: A summary of the model setup. a) The dimensions of the base case model given in μm. b) The dimensions of the geometry of the double-bend serpentine channel inside the μCGG base case model given in μm. c) A graphic overview of the boundary and initial conditions, components of the design, and the locations of concentration evaluations in the studies (highlighted in blue). The materials and methods section of each study will highlight the evaluation location in question. d) The normal-element mesh that is used in most studies.

3.1.2. Stationary study

To obtain a proof-of-concept of the new design, the model was solved for different ratios of the inlet velocities at the top and bottom inlet. This was done through a set of stationary studies applying a parametric sweep that varies u1 and u2 as defined in equation 3.1. Throughout the parametric sweep, the values of k1 and k2 were adjusted according to table 3.2, while $u_{max} = 6.66 \cdot 10^{-3}$ m/s (Ho et al., 2019). The concentration at point 1 (highlighted in blue in Figure 3.2) is evaluated against the ratio of u1/u2. This data is exported and interpolated using Scipys interp1d function to obtain a function of the concentration and corresponding ratio (see Appendix C for source code).
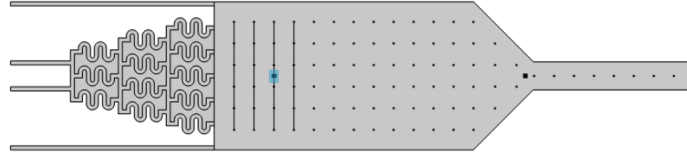
Figure 3.2: Geometry of the base case model. Point 1, where the concentration is evaluated in the stationary study, is highlighted in blue.

Table 3.2: Combinations of the values of k1 and k2 used in the parametric sweep, and the corresponding velocities u1 and u2. In all cases u_{max} = 6.66 · 10^{-3} m/s.

k1	u1 (m/s)	k2	u2 (m/s)
0.1	$6.66 \cdot 10^{-4}$	0.9	$5.99 \cdot 10^{-3}$
0.2	$1.33 \cdot 10^{-3}$	0.8	$5.33 \cdot 10^{-3}$
0.3	$2.00 \cdot 10^{-3}$	0.7	$4.66 \cdot 10^{-3}$
0.4	$2.66 \cdot 10^{-3}$	0.6	$4.00 \cdot 10^{-3}$
0.5	$3.33 \cdot 10^{-3}$	0.5	$3.33 \cdot 10^{-3}$
0.6	$4.00 \cdot 10^{-3}$	0.4	$2.66 \cdot 10^{-3}$
0.7	$4.66 \cdot 10^{-3}$	0.3	$2.00 \cdot 10^{-3}$
0.8	$5.33 \cdot 10^{-3}$	0.2	$1.33 \cdot 10^{-3}$
0.9	$5.99 \cdot 10^{-3}$	0.1	$6.66 \cdot 10^{-4}$

3.1.3. Mesh independence study

A mesh independence study was conducted to evaluate the effect of the mesh on the model outcome. In this study, three different combinations of $u0$, $u1$, and $u2$ were analyzed (see Table 3.3. The 'coarse'-, 'normal'-, 'fine'-, and 'finer'-sized element meshes were compared by evaluating the concentration across the line highlighted in blue in figure 3.3. The mesh sizes are summarized in Table 3.4. Figures of these meshes can be found in Appendix D. For this study, the data is exported and processed using Python (see Appendix C).

Table 3.3: Velocity combinations computed during the mesh independence study.

$u0$ (m/s)	$u1$ (m/s)	$u2$ (m/s)	ratio $u1/u2$
$6.66 \cdot 10^{-4}$	$5.99 \cdot 10^{-3}$	$6.66 \cdot 10^{-4}$	9.00
$6.66 \cdot 10^{-4}$	$3.33 \cdot 10^{-3}$	$3.33 \cdot 10^{-3}$	1.00
$6.66 \cdot 10^{-4}$	$6.66 \cdot 10^{-4}$	$5.99 \cdot 10^{-3}$	$1.11 \cdot 10^{-1}$
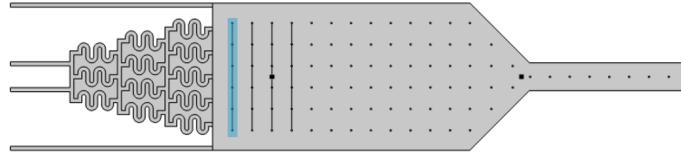
Figure 3.3: Geometry of the base case model. The line where the concentration is evaluated in the mesh study is highlighted in blue.

Table 3.4: Overview of mesh sizes.

Mesh	Domain elements	Boundary elements
Coarse	107312	5793
Normal	165698	6467
Fine	242743	7762
Finer	295871	9171

3.1.4. Time-dependent study

Constant inlet velocities

Next, a time-dependent study was performed with constant inlet velocities to identify the initialization time required to reach a steady state in the chamber and to analyze time delays between the beginning and the end of the chamber. For this, a time-dependent study was conducted between 0 and 180 seconds with 0.5 s time intervals. The data of the concentration in point 1 and point 2 (see Figure 3.4) was analyzed with Python.
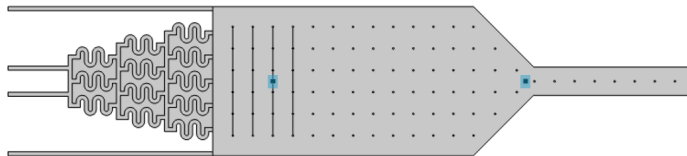
Figure 3.4: Geometry of the base case model. The points where the concentration is evaluated in the time-dependent study are highlighted in blue.

Changing inlet velocities

Finally, the inlet velocities of the top and bottom inlet were adjusted over time with the goal to obtain a desired concentration in point 1. First, an arbitrary step function of a desired concentration changing over time, resembling a discrete lifeline, was tested. The step function was created using the Python package matplotlib.pyplot's built-in step function. This step function takes into account the time delays that were identified in the previous section (resulting in required 'initialization time') and varies the concentration between 0 and 200 mmol/L. The step function can be divided into 6 sections where steps are taken of 50 mol/m^3, 100 mol/m^3, 75 mol/m^3, 25 mol/m^3, 200 mol/m^3, and 10 mol/m^3 respectively. Each of the steps is 30 s. Next, the interpolation function of the stationary study was used to obtain the required ratio over time.

The same approach was used to create a sine function, resembling a smooth lifeline. This sine function was obtained from Ho et al., 2019. Again, the function takes into account the initialization time and varies the concentration between 0 and 200 mmol/L. The initialization time is described with a step function set to 0 mol/m^3 for 80 s, while the sine function is described by equation 3.10. Here, c_i is the concentration of component i in mol/m^3, f the frequency in Hz, and t the time in s. The same interpolation function from the stationary study was used to obtain the required ratio over time. These

step and sine functions of concentration over time and their corresponding ratio over time functions are given in Figure 3.5. Both the complete step and the complete sine function descriptions can be found in Appendix E.

$$c_i = 200 \ \left(\frac{1}{2} \cdot sin \left(2\pi \cdot f \cdot t - \frac{\pi}{2} \right) + \frac{1}{2} \right) \tag{3.10}$$

Knowing that $ratio = u1/u2$ and $u_{max} = u1 + u2$, the inlet velocities at the top ($u1$) and bottom ($u2$) were set to equations 3.11 and 3.12 in the COMSOL Multiphysics base case model. Here, ratio(t) is the aforementioned ratio necessary to establish the desired concentration step function or sine function in point 1 (see Figure 3.5c and 3.5d). Again, $u_{max} = 6.66 \cdot 10^{-3}$ m/s (Ho et al., 2019).

$$u1 = \frac{u_{max}}{1 + \frac{1}{ratio(t)}} \tag{3.11}$$

$$u2 = \frac{u_{max}}{1 + ratio(t)} \tag{3.12}$$
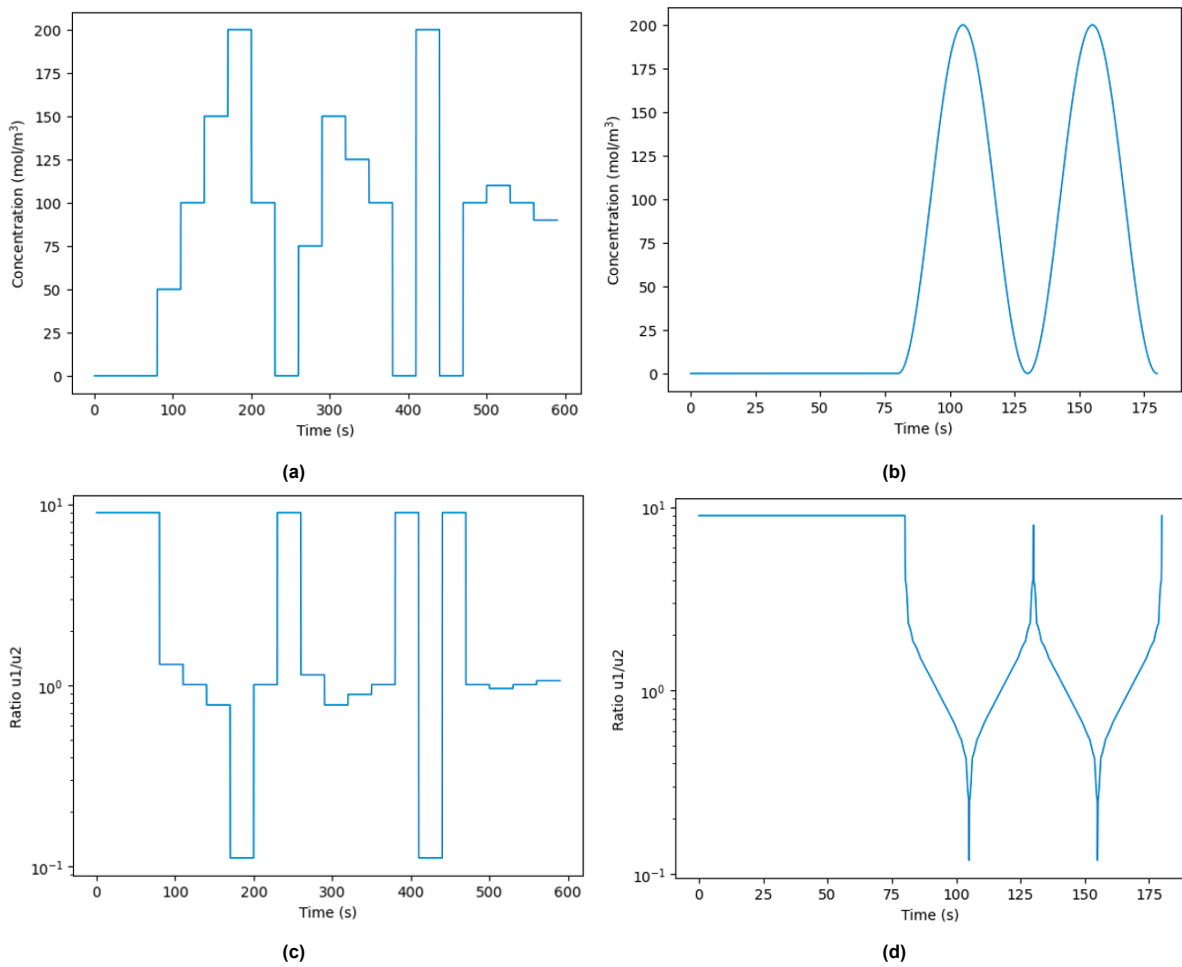
Figure 3.5: The step (a) and sine (b) function over time, which represent a discrete and smooth lifeline respectively. Their corresponding ratio over time functions are shown in c and b.

3.2. Experimental validation
To verify the results from the 2D model, the microfluidic device was fabricated using CAD, soft-lithography, and polydimethylsiloxane (PDMS) molding. Experiments were conducted with a laser scanning confocal microscopy set-up and results were analyzed and compared to the model.

3.2.1. Wafer fabrication
For the production of the wafer, which is used as the master mold for the devices, the desired geometry of the microfluidic channels was designed with Autodesk's AutoCAD software. Six different geometry designs were made: one is the base case from the previous section, and the other five geometries are variations of this design. To this base case geometry, inlets and outlets are added to connect the channels to the tubing during experiments. The inlets and outlets have diameters of 4 mm, to leave enough space to make a hole with the 2 mm puncher. The wafer was made by Albert Santoso[4] with soft-lithography technique.

To avoid the PDMS getting stuck onto the wafer, the wafer was covered with a saline layer. For this, a glass slide was placed into the desiccator and 1-2 droplets of the salinizing agent (1H,1H,2H,2H-perfluorooctyl trichlorosilane) were added on top of the glass slide. The wafer was placed in the desiccator (above the glass slide) for approximately 15 minutes. This procedure was only done once, before the fabrication of the first chips.

3.2.2. PDMS device fabrication
The PDMS elastomer and the curing agent were mixed in a ratio of 10:1. Subsequently, the solution was well mixed and placed into a desiccator for approximately 30 minutes to remove all air bubbles.

Glass microscope slides served as the support layer of the chip. To avoid any effect on the flow profile resulting from the difference in material properties between PDMS and glass, the microscope slides (Epredia) were spin-coated with PDMS. For spin coating, a 1 cm wide droplet of PDMS was added to the center of the microscope slide. The spin coater was set to rotate at 2000 rpm for 1 minute and 10 seconds with an acceleration rate of 400 rpm/s. The coated microscope slides were placed in the oven at 70 °C overnight. The remainder of the PDMS (after spin coating) was poured on top of the salinized wafer, which was placed in the oven at 70 °C overnight.

The PDMS layer was carefully removed from the wafer and the six chip designs were cut out from the PDMS layer. A hole puncher (2 mm diameter) was used to create the inlets and outlets. The upper layers of the chips were cleaned with ethanol and compressed air and placed in the oven at 70 °C for at least 2 hours.

Subsequently, the top (upside down) and bottom parts of the chips were placed in the plasma chamber (Harrick Plasma - Plasma cleaner). Upon reaching a stable pressure between 0.2-0.4 atm, the chamber is turned on to 'high' for 2 minutes and 20 seconds. Next, the plasma chamber is opened and the top parts were gently placed onto the bottom parts. The assembled devices were placed in the oven again at 70 °C for at least 30 minutes.

3.2.3. Stock solution preparation
Initially, a 0.5 M rhodamine B stock solution was made. Note that all rhodamine B solution containers should be covered with aluminum foil to avoid decolorization by light. To obtain a well-mixed stock, the solution was stirred overnight and was subsequently sonicated (VWR Ultrasonic Cleaner USC-TH) at 24 °C for 10 minutes.
From this stock solution, a range of dilutions was prepared. Each dilution was filtered twice (Whatmann 1 μm syringe filters) to remove any particles that may obstruct the microfluidic channels. The final dilution that was used in the experiments had a rhodamine B concentration of 0.1 mM.

3.2.4. Experimental set-up
For the experiments, three syringe pumps (Harvard Apparatus, Pump 11 Pico Plus Elite) were positioned on standards. Four 10 mL syringes (BD Plastipak) were filled with either water or 0.1 mM rhodamine B solution. The air bubbles were removed from the syringes and the syringes were subsequently connected to individual inlet tubes each with an inner diameter of 300 μm and a length of 20-40 cm (N.B. all tubing has an equal length). All the pumps were turned on to 100 μL/min to fill all tubing

---
[4]PhD candidate in the Department of Chemical Engineering, TU Delft

with liquid (and thereby remove the air).

First, as much air as possible was removed from the chip by washing with 70-100% ethanol (which has a better wetting angle with PDMS than water-based solutions (Yu et al., 2016). This was done by pipetting ethanol into the inlets and outlets by hand. The chip was then fixed on the microscope slide holder and the tubes (attached to the syringes) were connected to the chip. To remove any remaining air bubbles from the chip the pumps containing water were turned on to 100-200 μL/min and the pump containing rhodamine B only to 10-5 μL/min. This high difference between the different fluxes was chosen to avoid staining the PDMS with rhodamine B as much as possible. An overview of the experimental set-up can be found in Appendix F.

Both wide field and confocal images of the chip were taken and analyzed with a laser scanning microscope (Zeiss LSM 710) and ZEN Blue software. The microscope settings for the experiments are depicted in Table 3.5

Table 3.5: Confocal laser scanning microscope settings.

Setting	Value
Rhodamine B channel	415-797 nm
Laser	543 nm
Laser line attenuator transmission	10%
Pinhole	34.2 AU (Airy unit; 1 AU $\equiv$ 99.7 μm)
Gain	600
Digital offset	0
Digital gain	1.0

3.2.5. Experimental data processing

Before experimentation or whenever the view from the microscope was shifted, a wide field (WF) image was taken as a reference (since the channels themselves are not visible from the LSM image). During experiments, an LSM image was taken of the desired part of the chip. The intensity of the fluorescent dye in the picture is calculated by the ZEN Blue software. An intensity profile or histogram of choice can be drawn by hand using this software. This data was then exported to Microsoft Excel for initial data analysis: for every experiment, the average over two duplicates (and respective absolute errors) is calculated and visualized. Next, the data is visualized and compared to the model data. For this data analysis, it is assumed that the measured intensity is proportional to the concentration of rhodamine B at that location. Furthermore, the intensity is normalized between 0 and 1 according to equation 3.13, to compare results with those from the model.

$$I_{norm} = \frac{I - I_{min}}{I_{max} - I_{min}}$$ (3.13)

In this equation, I is the measured intensity, I_{min} is an average of the minimum intensity measured in the PDMS (where there are no channels) corresponding with noise in the image, and I_{max} is the average of the maximum intensity measured in the bottom inlet (where only the maximum concentration of rhodamine B should be flowing). Unfortunately, no corrections could be performed for the difference in measured intensity between the center of the images and the borders and corners of the images. PDMS staining with rhodamine B cause 'high intensity' outliers, which would interfere with such corrections.

3.2.6. μCGG velocity study

The velocities used during experimentation differed from the velocities used in the base case model due to calculation errors (see Appendix F). Therefore, also a μCGG velocity study was conducted because of these velocity discrepancies. In this study, a fluid velocity that results in acceptable mixing in

the μCGG while still maintaining syringe pump handleability was identified.

A set of seven different flow rates on the pump connected to the μCGG were tested (see Table 3.6). During all experiments, the flow rates on the pumps connected to the top inlet (with water) and bottom inlet (with rhodamine B) were 25.2 μL/min and 2.8 μL/min respectively (to prevent severe staining of the PDMS chamber). Upon changing to a new flow rate on the pump, at least 30-60 seconds were taken to ensure a steady state flow in the device was established, before capturing WF and LSM images. All experiments were conducted in duplicate. The results were analyzed with ZEN by drawing intensity profiles across the five outlets of the μCGG (similar to the locations highlighted in Figure 3.6).

Furthermore, the characteristic times of diffusion (the mixing mechanism) and the characteristic time for convection (the residence time in the serpentine channels) were calculated as shown in equations 3.14 and 3.15. Assuming two fluids 'meet' each other at the center of the channel (like with a T-junction), the penetration depth is half the width of the channel (δ = 50 μm). The average length is assumed to be the distance traveled in the center of the serpentine channels for a double-bend (L = 2357 μm). Also, the diffusion coefficient of rhodamine B (D_{RB}) is used for the calculations. With these characteristic times, possible geometric adjustments to the μCGG can be derived.

$$t_{diffusion} = \frac{\delta^2}{\pi D_{RB}} = \frac{(50 \cdot 10^{-6})^2}{\pi \cdot 3.6 \cdot 10^{-10}} = 2.21s \tag{3.14}$$

$$t_{convection} = \frac{L}{u} = \frac{2357}{9.33 \cdot 10^{-3}} = 0.24s \tag{3.15}$$

Table 3.6: Flow rates and corresponding velocities (assuming the rectangular cross-section of the microfluidic channels - Appendix F) used for the μCGG velocity study.

ϕ (μL/min)	$u0$ (m/s)
8.4	$2.80 \cdot 10^{-2}$
2.8	$9.33 \cdot 10^{-3}$
1.4	$4.67 \cdot 10^{-3}$
0.5	$1.67 \cdot 10^{-3}$
0.2	$6.67 \cdot 10^{-4}$
0.05	$1.67 \cdot 10^{-4}$
$12 \cdot 10^{-3}$	$4.00 \cdot 10^{-6}$

To compare the model with the experimental data, some adjustments were made to the base case model setup as described in section 3.1.1. First, in the base case glucose was assumed to be the solute. However, during experiments, rhodamine B was used. Therefore, the diffusion coefficient of rhodamine B, $3.6 \cdot 10^{-10}$ m^2/s, was used (Abdul et al., 2005).

For the velocity study in the μCGG, a stationary parametric sweep was performed using the adjusted velocities as mentioned in Table 3.6, while the velocity of the top and bottom inlet are $8.40 \cdot 10^{-2}$ m/s and $9.33 \cdot 10^{-3}$ m/s, respectively. After running the simulation, the concentration across the five lines that correspond with the outlets of the μCGG was evaluated (see blue highlighted lines in Figure 3.6). The concentrations measured were normalized between 0 and 1 according to equation 3.16 to compare the results with the experimental data.

$$c_{norm} = \frac{c - c_{min}}{c_{max} - c_{min}} = \frac{c}{c_{max}} \tag{3.16}$$

In this equation, c is the calculated concentration in the model, c_{min} is the minimum concentration, and c_{max} the maximum concentration. Since the minimum concentration is equal to zero, the equation can

be simplified.

To measure the prediction accuracy of the model for concentration in the specified locations (see Figure 3.6), the root mean square error was calculated with equation 3.17. Here, z_{f_i} is the prediction value from the model and z_{o_i} the observed experimental value. The sum of all errors on every position at the specified evaluation locations is incorporated into the calculations.

$$RMSE = \sqrt{\frac{\sum_{i=1}^{N}(z_{f_i} - z_{o_i})^2}{N}} \tag{3.17}$$
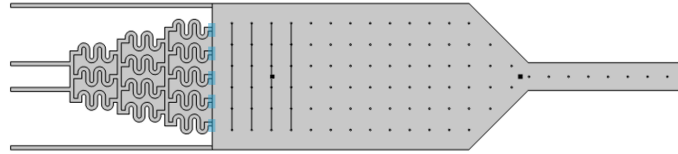
Figure 3.6: Geometry of the base case model. The channel lengths where the concentration is evaluated in the mixer velocity study are highlighted in blue. In the results section, the bottom μCGG outlet is denoted as channel 1, the upper outlet as channel 5.

3.2.7. Velocity ratio ($u1$ / $u2$) study

In this study, it was decided to continue with a mixer velocity $u0 = 1.67 \cdot 10^{-3}$ m/s (or ϕ = 0.5 μL/min). For these experiments, the different velocity ratios mentioned in section 3.1.2 were tested. Again, for this study, there were errors in the conversion calculations from velocities (model) to flow rates (pumps) (Appendix F). This may affect the width of the gradient as will be further elaborated in section 4.2. However, since the ratio between the two velocities will remain the same, these were still valid for validation of the gradient shift mechanism. The flow rates and corresponding velocities that were tested are shown in Table 3.7. Again, at least 30-60 seconds were taken before capturing WF and LSM images, and all experiments were conducted in duplicate. The results were analyzed with ZEN by drawing intensity profiles across the four lines in the chamber (similar to the locations highlighted in Figure 3.7).

Table 3.7: Combinations of the flow rates of the top and bottom inlets and corresponding velocities (assuming the rectangular cross-section of the microfluidic channels - Appendix F) used for the velocity ratio study.

$\phi1$ (μL/min)	$u1$ (m/s)	$\phi2$ (μL/min)	$u2$ (m/s)
25.2	$8.40 \cdot 10^{-2}$	2.8	$9.33 \cdot 10^{-3}$
22.4	$7.47 \cdot 10^{-2}$	5.6	$1.87 \cdot 10^{-2}$
19.6	$6.53 \cdot 10^{-2}$	8.4	$2.80 \cdot 10^{-2}$
16.8	$5.60 \cdot 10^{-2}$	11.2	$3.73 \cdot 10^{-2}$
14.0	$4.67 \cdot 10^{-2}$	14.0	$4.67 \cdot 10^{-2}$
11.2	$3.73 \cdot 10^{-2}$	16.8	$5.60 \cdot 10^{-2}$
8.4	$2.80 \cdot 10^{-2}$	19.6	$6.53 \cdot 10^{-2}$
5.6	$1.87 \cdot 10^{-2}$	22.4	$7.47 \cdot 10^{-2}$
2.8	$9.33 \cdot 10^{-3}$	25.2	$8.40 \cdot 10^{-2}$

In this study, the same adjustments were made to the base case model setup as for the μCGG velocity study (section 3.2.7). A stationary parametric sweep was performed using the adjusted velocities as mentioned in Table 3.7, while the new μCGG velocity is $1.67 \cdot 10^{-3}$ m/s. After running the simulation, the concentration was evaluated across the four lines in the chamber of the device (see blue highlighted lines in Figure 3.7). These lines correspond with the following distance from the μCGG and will be

further referred to as such: 520 μm, 1060 μm, 1600 μm, and 2140 μm. Again, the concentrations were normalized between 0 and 1 according to equation 3.16. Again, the RMSE (equation 3.17) is calculated to measure the prediction accuracy of the model in the evaluation locations (Figure 3.7).
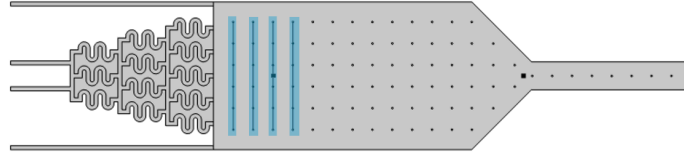
Figure 3.7: Geometry of the base case model. The lines where the concentration is evaluated in the velocity ratio study are highlighted in blue. These are further referred to as line 520, line 1060, line 1600, and line 2140.

3.3. Optimization of the system

3.3.1. Adjusting the width of the chamber

To reduce the switching frequency between discretized concentration levels, an early iteration of the current base case model was analyzed. In this geometry, the width of the chamber was smaller because the μCGG was not yet incorporated. The inlets (to be connected to the μCGG) had a width of 100 μm and were spaced 100 μm apart resulting in a chamber width of 1300 μm (see Figure 3.8 A). The following concentrations were used at the inlets: $c1 = c2 = 0$ mol/m^3, $c3 = 50$ mol/m^3, $c4 = 100$ mol/m^3, $c5 = 150$ mol/m^3, and $c6 = c7 = 200$ mol/m^3. The μCGG velocity $u0 = 0.1u_{max}$ with $u_{max} = 6.66 \cdot 10^{-3}$ m/s (Ho et al., 2019). The velocities at the top and bottom inlet ($u1$ and $u2$) are governed by the same equations as in the time dependent study (equations 3.11 and 3.12).

A stationary study was conducted, and the resulting interpolation function was used to create an arbitrary step function of a desired concentration in point 1 (Figure 3.8 B), similar to the approach for the base case model in section 3.1.2. This interpolation function was used to convert an arbitrary concentration step function (Figure 3.8 C and Appendix E) into the corresponding ratio of u1 and u2 (Figure 3.8 D). Here, each step corresponds with a concentration change of 50 mol/m^3, and the steps were 4 seconds long with an initialization time of 8 seconds. Note that this initialization time is much shorter than described in section 3.1.4 because of the absence of the μCGG.
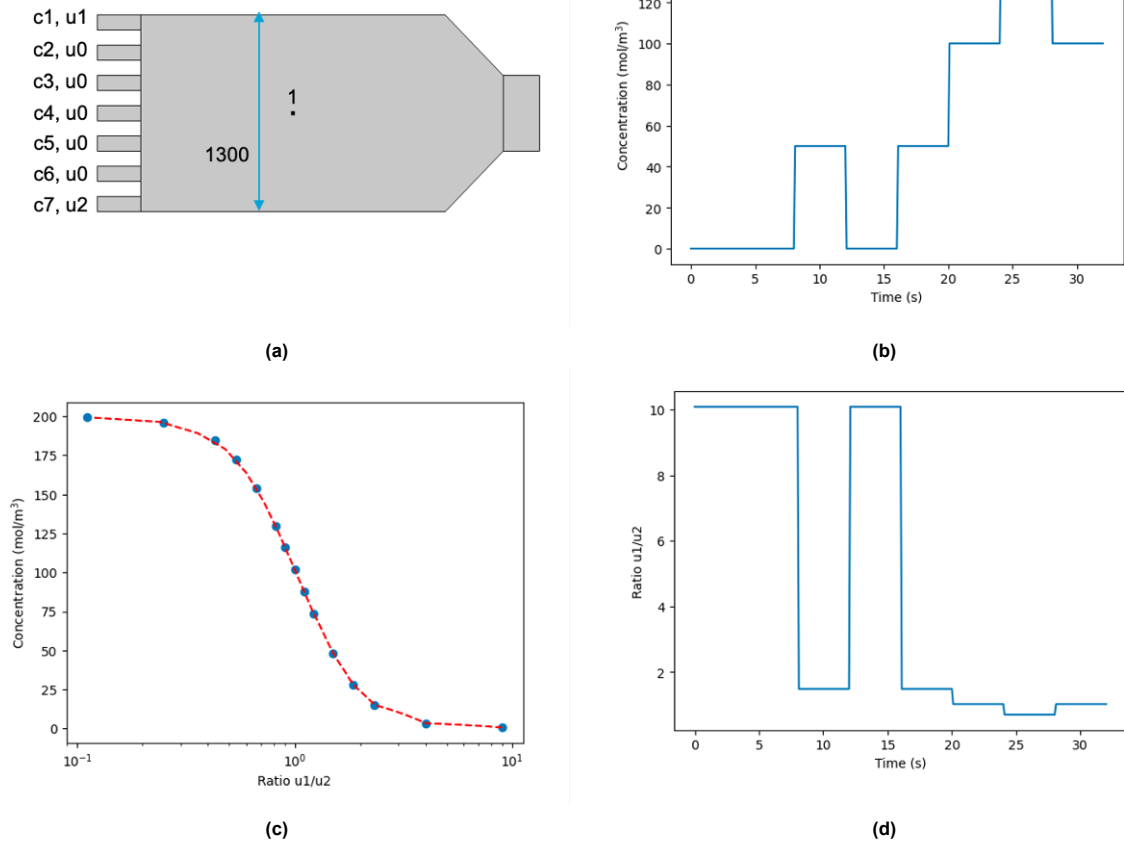
Figure 3.8: a) The geometry of a previous design of the chamber that has a width of 1300 μm, the concentration is evaluated in point 1. b) The results from a stationary parametric sweep (blue) and the interpolation function (red). c) The step function of the desired concentration over time in point 1. d) The corresponding step function of the ratio (u1/u2) over time.

3.3.2. Adjusting the spacing between the μCGG outlets

The base case model, where outlets of the μCGG are 500 μm apart, was compared to an alternative geometry that has 750 μm between every μCGG outlet, to see if a wider gradient could be established. This geometry can be found in Appendix B. The same model set-up as discussed for the base case model (section 3.1.1) was applied to this adjusted geometry in COMSOL Multiphysics. Again, a stationary study was conducted where $u1 = u2 = 0.5u_{max}$ and $u0 = 0.1u_{max}$ with $u_{max} = 6.66 \cdot 10^{-3}$ m/s (Ho et al., 2019). The concentration was evaluated in line 2140 for both geometries, highlighted in blue in Figure 3.9.
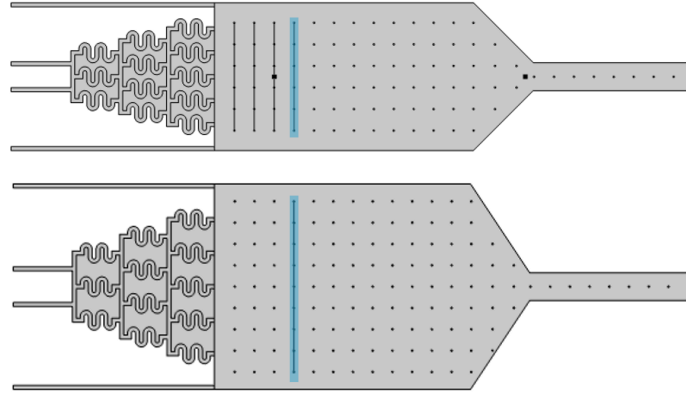
Figure 3.9: Geometry of the base case model with 500 μm spacing (top) and that of the model with 750 μm spacing (bottom). The lines where the concentration is evaluated in the adjusted spacing study are highlighted in blue.

3.3.3. Adjusting the ratio between velocities $u0$ and u_{max}

An alternative solution to the gradient width limitation could be to increase the ratio between the velocity inside the μCGG ($u0$) and the velocity at the top and bottom inlets ($u1$ and $u2$). Knowing that $u1 + u2 = u_{max}$, a stationary study was conducted with the base case model where the ratio between $u0$ and u_{max} were varied. In this study, u_{max} is kept constant while three different $u0$ are tested. The ratio $u1/u2$ is kept constant: $u1 = 0.9u_{max}$ and $u2 = 0.1u_{max}$. The different combination of $u0$, $u1$, $u2$, and u_{max} are summarized in Table 3.8. The concentration is evaluated in line 4 (see Figure 3.10).

Table 3.8: Combinations of the flow rates and velocities tested in the ratio study of $u0$ and u_{max}.

$u0$ (m/s)	u_{max} (m/s)	$u1$ (m/s)	$u2$ (m/s)
$9.33 \cdot 10^{-3}$	$6.66 \cdot 10^{-3}$	$5.99 \cdot 10^{-3}$	$6.66 \cdot 10^{-4}$
$6.67 \cdot 10^{-3}$	$6.66 \cdot 10^{-3}$	$5.99 \cdot 10^{-3}$	$6.66 \cdot 10^{-4}$
$1.67 \cdot 10^{-3}$	$6.66 \cdot 10^{-3}$	$5.99 \cdot 10^{-3}$	$6.66 \cdot 10^{-4}$
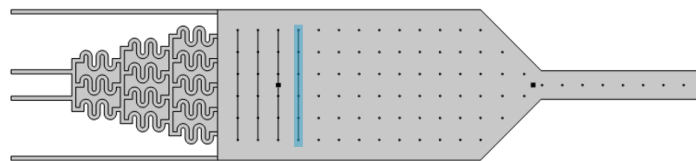
Figure 3.10: Geometry of the base case model. The line where the concentration is evaluated in the ratio study between $u0$ and u_{max} is highlighted in blue.

3.3.4. μCGG modelling in Ansys Fluent

A model of the μCGG was set up in both COMSOL Multiphysics and Ansys Fluent. The geometry used in the 2D COMSOL Multiphysics model is shown in Figure 3.11. The model set-up in COMSOL Multiphysics was similar to the set-up of the base case model. Both laminar flow and transport of diluted species are calculated. In this model, the two inlets were defined that have similar fluid velocities ($u0$), and where the top inlet has a maximum concentration of 1 mol/m^3 while the bottom inlet has a minimum concentration of 0 mol/m^3. The model has five outlets similar to the base case model. The mesh, solver and initial and boundary conditions were also the same as that of the base case model.
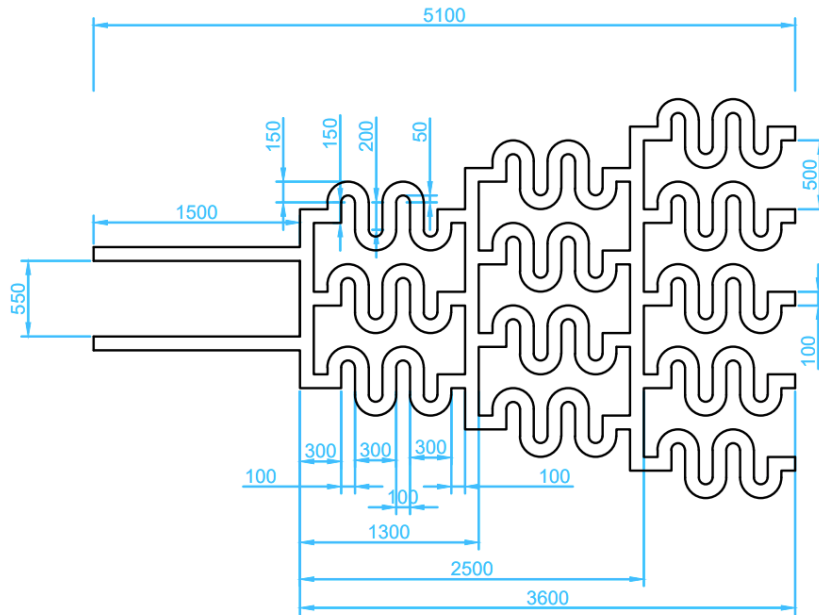
Figure 3.11: Dimensions of the μCGG geometry given in μm.

The Ansys model used the same geometry as the COMSOL Multiphysics model. In this model, laminar flow and species transport were selected. For the latter, a tracer (with rhodamine B properties) was created. Similar to the model in COMSOL Multiphysics, the two inlets were set as velocity inlets, and the outlets as pressure outlets. The system of equations of the model was discretized according to third order MUSCL scheme.

A stationary study was conducted with both models for the following conditions: $u0 = 9.33 \cdot 10^{-3}$ m/s and $D_{RB} = 3.6 \cdot 10^{-10}$ m²/s. The concentration at the boundary of all five outlets of the mixer were analyzed for both models and compared to the concentration profiles from the experimental results (see Figure 3.12). Similar to the experimental validation studies, the RMSE (equation 3.17) is calculated for both models in the evaluation locations (Figure 3.12) to measure the prediction accuracy (compared to the experimental data).
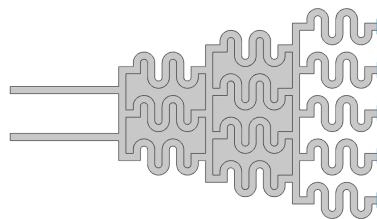
Figure 3.12: Geometry of the mixer model. The boundaries of all five outlets are the locations where the concentration is evaluated in this μCGG geometry study and is highlighted in blue. From bottom to top, the channels are referred to as channel 1, 2, 3, 4, and 5.

Design of experiments (DoE)

In the design of experiments (DoE), the model was served for a range of design points between $u0 = 1 \cdot 10^{-5} - 1 \cdot 10^{-2}$ m/s and $D = 1 \cdot 10^{-11} - 1 \cdot 10^{-9}$ m²/s. The degree of homogeneity was calculated as the normalized ratio between the maximum and minimum concentration at the third outlet boundary (see Figure 3.13). The expression for this normalized ratio is given by equation 3.18. In this equation, S is the array scalars of concentrations calculated at the boundary of the third outlet. The results were analyzed by interpolating the P data with a 2D interpolation function that makes use of Scipys nearest

neighbour interp1d function (see Appendix C).

$$P = \frac{minimum(S_{channel3})}{maximum(S_{channel3})}$$

(3.18)
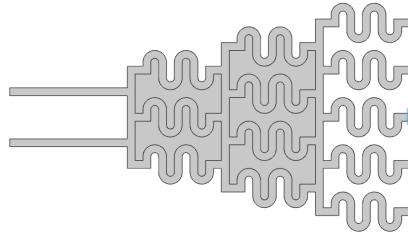
Figure 3.13: Geometry of the mixer model. The boundary of the third outlet is the location where the concentration is evaluated in this μCGG geometry study and is highlighted in blue.

4

Results and discussion

4.1. The new geometry: a 2D model

A 2D model of the new geometry was created in COMSOL Multiphysics and a stationary study, mesh independence study, and time-dependent study were conducted to analyze the capabilities and limitations of the new design.

4.1.1. Stationary study

A stationary study was conducted to see whether the dynamic mechanism does indeed move the gradient across the chamber. In this study, the top and bottom inlet velocities were varied according to the ratios mentioned in Table 3.2. The value of the concentration was measured in point 1 (see Figure 3.2). The graph in Figure 4.1 shows that, by varying this ratio between 10^{-1} and 10^1, a whole range of concentrations between the minimum (0 mol/m^3) and maximum (200 mol/m^3) concentration can be achieved in point 1. The three surface plots on the right in Figure 4.1 graphically show this shift of the concentration gradient across the chamber. It can be seen that at a given inlet velocity ratio, indeed a steady gradient can be established throughout the chamber although the shape of the gradient is somewhat wider or more dispersed at the far end of the chamber compared to the center of the chamber. It can also be seen that some distance is required before the steady gradient is reached that can be seen across the chamber.
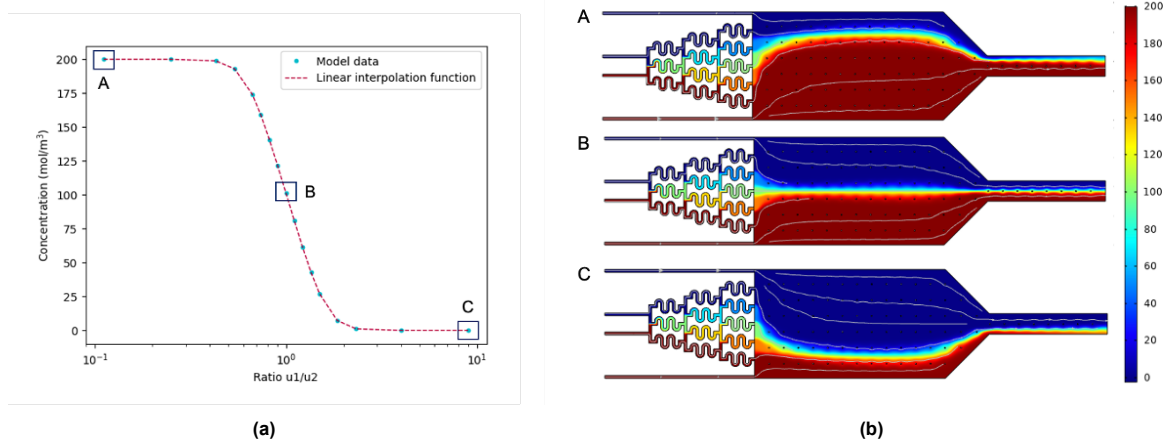
Figure 4.1: The results of the stationary study. a) The concentration data from the parametric sweep versus the corresponding ratio on a logarithmic scale. b) The surface plots A through C, corresponding with the three data points where the ratio is $1.11 \cdot 10^{-1}$, 1, and 9 respectively in Figure 4.1a.

4.1.2. Mesh independence study

A mesh independence study was conducted to validate that the results from the base case model do not rely on the mesh that was used. Therefore, a stationary simulation for the three ratios highlighted in the previous section (see surface plots A-C in Figure 4.1) was run using four different meshes: the

coarse-element mesh, the normal-element mesh, the fine-element mesh, and the finer-element mesh. A summary of their sizes is given in section 3.1.3 and Appendix D. The concentration was evaluated across the first line (see Figure 3.3) for every mesh. To compare the meshes, the error was calculated between the concentration of each mesh and the concentration of the most refined mesh (the finer-element mesh). These errors are plotted in Figure 4.2. In these graphs, it can be seen that the error between the concentration calculated with the coarse-element mesh and the finer-element mesh is the highest. As the mesh becomes more refined, this error decreases. However, the highest calculated error is approximately 4 mol/m^3, which is only 2% of the maximum concentration. Thus, the results obtained with all the meshes are similar to that of the finer-element mesh. Furthermore, it can be seen that the highest errors are obtained at locations where a pillar is located. These locations correspond with the peaks in the graphs in Figure 4.2. This is to be expected since the mesh becomes more complex in the neighborhood of more complex geometric structures. Thus, if a mesh is less refined, more information is lost in these complex geometric areas. Based on these results, it was decided to continue simulations with the normal-element mesh, since results do not improve significantly by refining the mesh while computation time does increase.
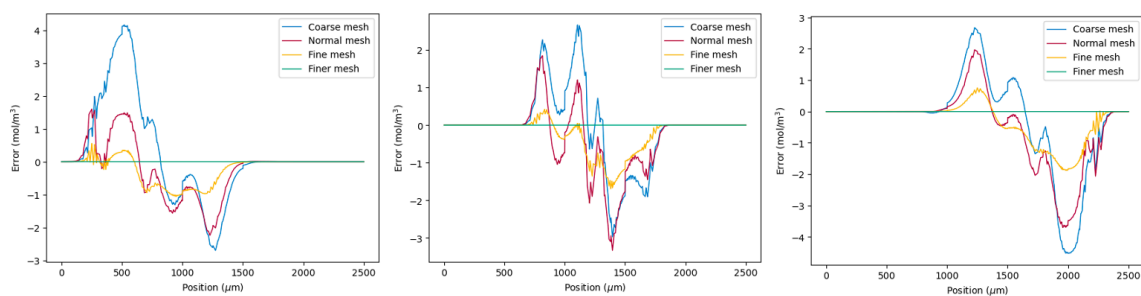
Figure 4.2: The results of the mesh independence study. Three conditions were tested: from left to right the ratio of u1 and u2 was 9, 1, and $1.11 \cdot 10^{-1}$. The concentration observed on line 1 under each of the three conditions for every mesh was subtracted from the concentration here observed with the most refined finer-element mesh. In each graph, these resulting errors across line 1 are plotted for every mesh.

4.1.3. Time-dependent study

Next, a time-dependent study with constant inlet velocities was conducted to assess the time necessary to reach a steady state gradient at the evaluation points in the chamber. Also, a study was conducted where the inlet velocities at the top and at the bottom of the device varied over time to assess the feasibility of mimicking lifelines with this system.

Constant inlet velocities

A constant inlet velocity at each of the four inlets of the model was applied, with $u1 = u2 = 0.5u_{max}$ and $u0 = 0.1u_{max}$. The concentration change over time in point 1 and point 2 is depicted in Figure 4.3. In this graph, for both points, the time at which the concentration starts to change and the time at which a steady state is achieved is indicated with a dashed line. At point 1, the concentration starts to change after 32 s, and a steady state is reached after 70 s. At point 2, the concentration starts to change earlier, after 29 s, while the steady state is achieved later, after 84 s. Also, at point 2, a stabilization of the concentration can be seen between 40 s and 60 s. This earlier concentration change and the stabilization of the concentration are caused by the short time required for the fluid leaving the bottom inlet to reach the chamber. The distance traveled by the fluid from this inlet is much shorter than that by the fluid from the μCGG. Therefore, the fluid from the bottom inlet reaches point 2 first, causing a quick increase in concentration (as this fluid contains the maximum solute concentration). Then, the concentration stabilizes as this fluid flow (counteracted by the flow from the top inlet) reaches a steady state. Around 60 s, the fluid from the μCGG reaches point 2 and causes a second period of quick increase of the concentration. This effect is not visible at point 1, as point 1 lies much closer to the μCGG. The fluid coming from the μCGG prevents the high concentration from the bottom inlet to reach point 1 through convection. Thus, the solute can only reach point 1 through diffusion. As diffusion is a slower process (see equations 2.7 in chapter 2), there is no concentration increase of the solute before the gradient from the μCGG reaches point 1. This results in the 'smooth' concentration

increase observed in point 1 (Figure 4.3). These effects can be easily observed from an animation of the concentration surface plot (Appendix G).
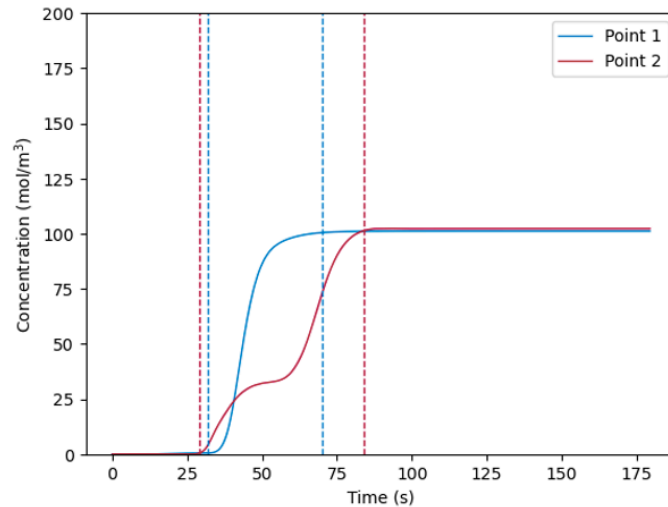
Figure 4.3: The results of the time-dependent study with constant inlet velocities ($u1 = u2 = 0.5u_{max}$ and $u0 = 0.1u_{max}$). The concentration in point 1 and point 2 are plotted over time. The dashed lines indicate the moments when the concentration starts to change and the moment a steady state is reached.

Changing inlet velocities

A time-dependent study was conducted where the velocity of the top and bottom inlet varied over time. First, an arbitrary step function of the concentration (within the range 0-200 mol/m^3) over time was created that mimics a discrete lifeline. The interpolation function was used to calculate the corresponding ratio that should be established over time. The top and bottom inlet velocities were varied accordingly. This yielded the concentration profile in Figure 4.4a. Here, no delays in the overall profile are observed, thus the time taken for initialization is sufficient. However, analyzing each of the steps themselves, there is a delay before the desired concentration of that step is reached. For steps where the desired concentration lies within the gradient (between 0 and 200 mol/m^3) this delay is longer than for steps that have a desired concentration equal to the maximum (200 mol/m^3) or minimum (0 mol/m^3) concentration. This is likely caused by the fact that the desired ratio that corresponds with the minimum or maximum concentration is either the highest or lowest possible ratio from the interpolation function (Figure 4.1). However, there is a range of ratios that correspond with the minimum concentration and a range of ratios that correspond with the maximum concentration, as can be easily seen from Figure 4.5. Here, these 'ratio regions' are shaded in blue. Thus, when changing the ratio in the step function to the minimum or maximum, the desired concentration is reached earlier than expected.

The height of the step also impacts the time necessary to establish the desired concentration. The delay for steps of 50, 75, and 100 mol/m^3 is ∼30 seconds, while the delay for steps of 25 mol/m^3 is ∼20 seconds, and for steps of 10 mol/m^3 the delay is only ∼15 seconds. This effect is to be expected since the more distance must be traveled by the gradient the longer it takes while the total velocity remains constant (for velocity surface plots corresponding with this time-dependent study, refer to Appendix H). However, again note that this does not apply to steps where the desired concentration is 0 mol/m^3 (minimum) or 200 mol/m^3 (maximum), for which the delay is ∼5 seconds.
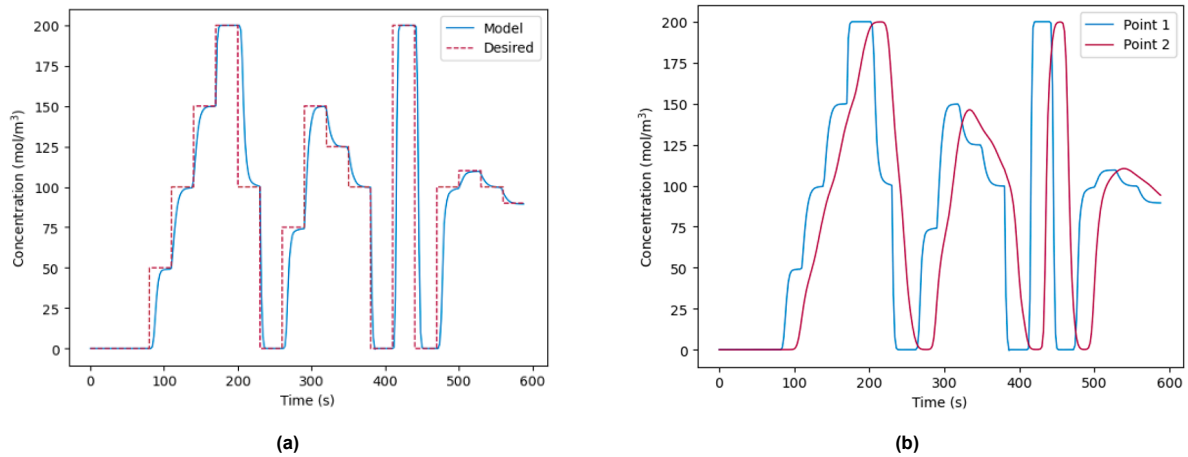
Figure 4.4: The results of the time-dependent study with a varying step-wise inlet velocity at the top and at the bottom. (a) A comparison between the desired concentration (described by the arbitrary step function in section 3.1.4). (b) A comparison between the observed concentration at point 1 and point 2.

In Figure 4.4b the concentration profile observed in point 1 and the profile observed in point 2 are compared. Here, it is immediately visible that there is a significant delay in the signal between these two points, which severely affects the resolution of the step function. Thus, if a change of concentration should be established across the entire length of the chamber, more than 30 seconds is necessary per step. For future studies, it is therefore recommended to perform the interpolation on a parametric sweep from results in point 2 and generate a new step function for this second point.
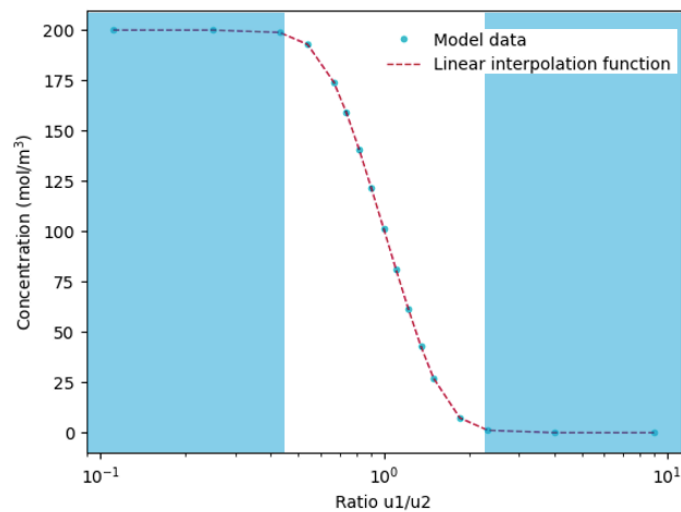
Figure 4.5: The regions of ratios of u1/u2 that correspond with the minimum and maximum concentration, highlighted in blue.

A time-dependent study was also performed with a sine function that mimics a smooth lifeline. Figure 4.6a shows this desired and observed concentration change in the time-depended study at point 1. Here, a delay of the concentration change in point 1 is observed when compared to the desired concentration profile. This delay is only a few seconds, and is likely also present in the results from the time-dependent study with the step-function, although not as visible due to the higher time scale. It is suggested for future studies to increase the initialization time with a few seconds to avoid these slight delays. The graphs shape of the observed concentration at point 1 in the model and that of the desired concentration is similar, showing that a sine concentration profile can be achieved at point 1. When comparing point 1 and point 2, again resolution of the intended sine function is lost. The same recommendation as with the step function time-dependent study applies here.
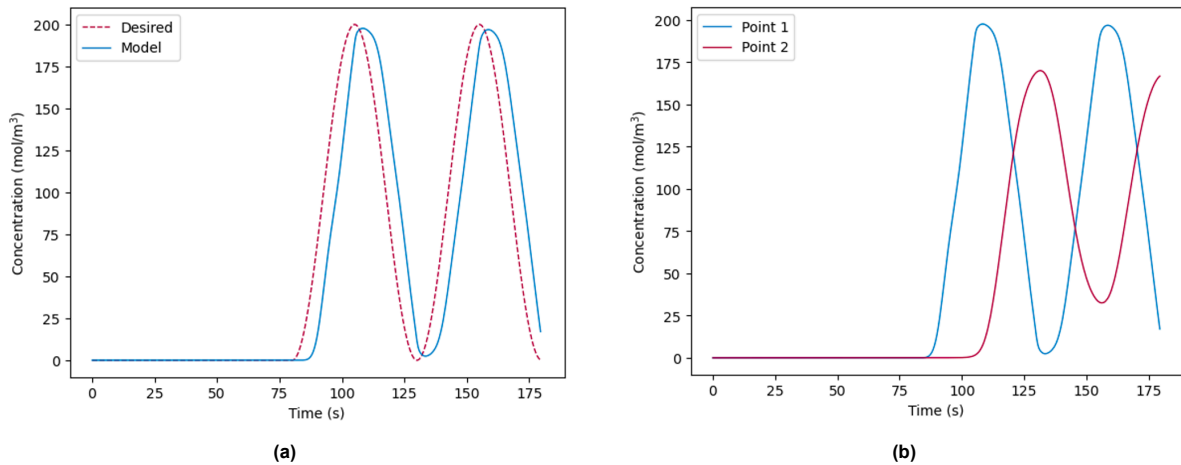
Figure 4.6: The results of the time-dependent study with a varying sine function inlet velocity at the top and at the bottom. (a) A comparison between the desired concentration (described by the arbitrary step function in section 3.1.4). (b) A comparison between the observed concentration at point 1 and point 2.

From these studies it can be seen that with this specific geometry, and depending on the height of the concentration step or slope, the maximum response time observed in point 1 is approximately 30 seconds. For point 2, this time is approximately 15 seconds longer. This is relatively long when compared to the oscillation times established by the dMSCC devices in Ho et al. (2022) and Täuber et al. (2022). To improve this response time, an optimization study on the chamber geometry was conducted which is further elaborated in section 4.3.1.

4.2. Experimental validation of the 2D model

4.2.1. μCGG velocity study

First, a velocity study in the μCGG was conducted to identify the flow rate at which the best mixing is established without compromising on the experimental ease of use of the pump system. Initial calculations determined the flow rate in the μCGG ($\phi0$) to be 2.8 μL/min. However, as can be seen from Figure 4.7, this velocity showed poor mixing: the top two outlets of the μCGG have a similar very low intensity, the bottom two outlets of the μCGG have a similar very high intensity, and the middle outlet of the μCGG shows a sharp divide between a high and low intensity.
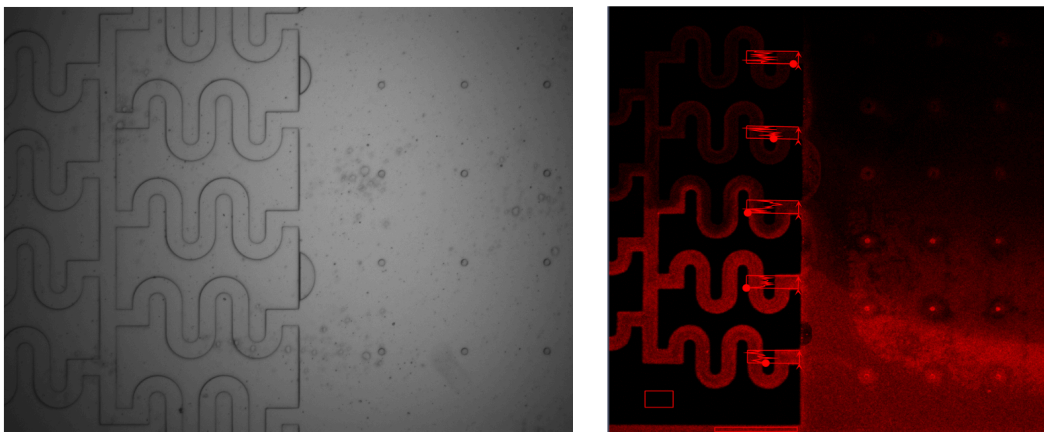
Figure 4.7: The WF (left) and LSM (right) image of the μCGG velocity study where $\phi0 = 2.8\mu L/min$. The WF image shows the section of the dMSCC device that shows the outlets of the μCGG. Two small remaining air bubbles can be seen that failed to be removed. The intensity of the rhodamine B fluorescence is shown by the red color in the LSM image. The arrows in the outlets of the μCGG indicate the line along which the intensity profile was generated by ZEN. For the area covered by the rectangles in the PDMS (black) and the bottom inlet respectively, a histogram intensity profile was generated by ZEN. The average of the intensity in these areas was used as the minimum and maximum intensity for the normalization of the data in the profiles in the μCGG outlets.

The serpentine channels inside the μCGG allow for diffusion-based mixing. As seen from equation 2.7, the time necessary for diffusion depends on the penetration depth and the diffusion coefficient. The characteristic time necessary for diffusion in these bends and the residence time (characteristic time for convection - equation 2.1) were compared. These characteristic times (2.21 s for diffusion and 0.24 s for convection) showed that indeed for this $\phi 0$ there is insufficient residence time for proper mixing. By increasing at least 9-10 times the length of the serpentine channels, the residence time is increased 9-10 times allowing for enough time for complete diffusion across the width of the channel.

Thus, in the current μCGG design, the short characteristic time for convection prevents proper mixing by diffusion. Another approach to increase the residence time is to adjust the fluid velocity in the μCGG. Therefore, a velocity study was conducted where seven different flow rates (and therefore seven different velocities) were tested. According to the expression for characteristic time for convection it is expected that by lowering the velocity, the residence time inside the double-bend is increased. Consequently, it is expected that all the concentration profiles become more linear across the length of the channel, indicating better homogenization. Furthermore, it is expected that each serpentine μCGG outlet produces a unique and homogeneous concentration as the velocity decreases and mixing improves. The normalized concentration profile for four of the seven tested velocities is shown Figure 4.8 (the results of the other three can be found in Appendix I).

(a) ϕ = 8.4 μL/min; u = 2.80 $\cdot$ 10^{-2} m/s

(b) ϕ = 2.8 μL/min; u = 9.33 $\cdot$ 10^{-3} m/s

(c) ϕ = 0.5 μL/min; u = 1.67 $\cdot$ 10^{-3} m/s

(d) ϕ = 12 nL/min; u = 4.00 $\cdot$ 10^{-6} m/s
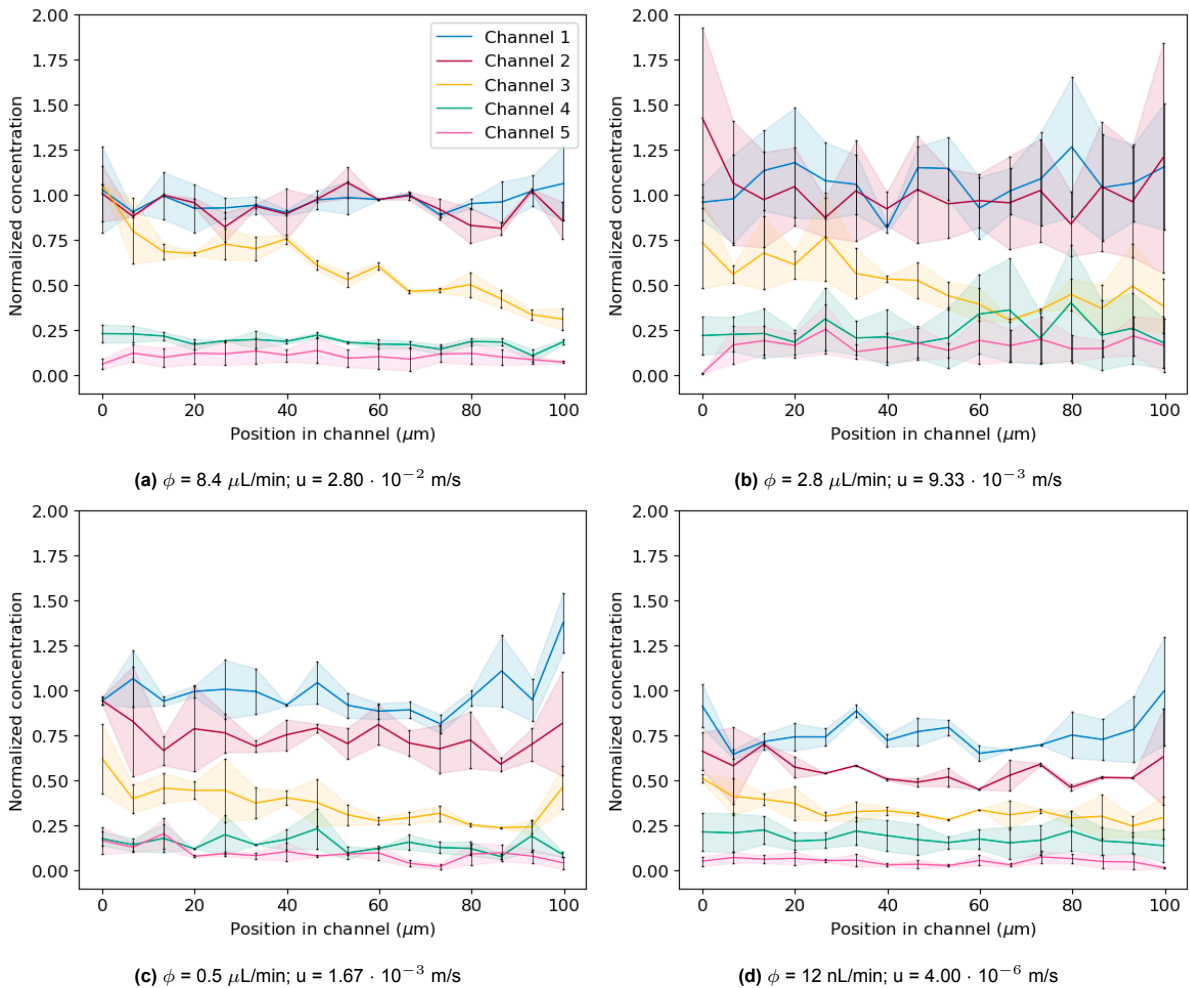
Figure 4.8: Experimental data from the μCGG velocity study. The results from four out of seven examined velocities are plotted as the average normalized concentration of the duplicates. The error bars indicate the spread of the duplicates. This area of spread is shaded in the corresponding color as a guide to the eye. High intensity outliers at the boundaries of the channels likely caused by rhodamine B staining of the PDMS.

These expected trends are indeed observed. The lower the flow rate (or velocity), the more homogeneous concentration profiles are observed. This effect is especially visible in the 3rd μCGG outlet. Also, the observed intensity profiles of the bottom two channels (channel 1 and 2) and the bottom two channels (channel 4 and 5) become more distinct. Although the smallest velocities (0.2 μL/min, 0.05 μL/min (Appendix I), and 12 nL/min) show the best results with unique and homogeneous concentration profiles at all five μCGG outlets, these velocities resulted in complications while handling the pump system. Therefore, 0.5 μL/min was chosen as the final velocity in the μCGG used in further experimentation.
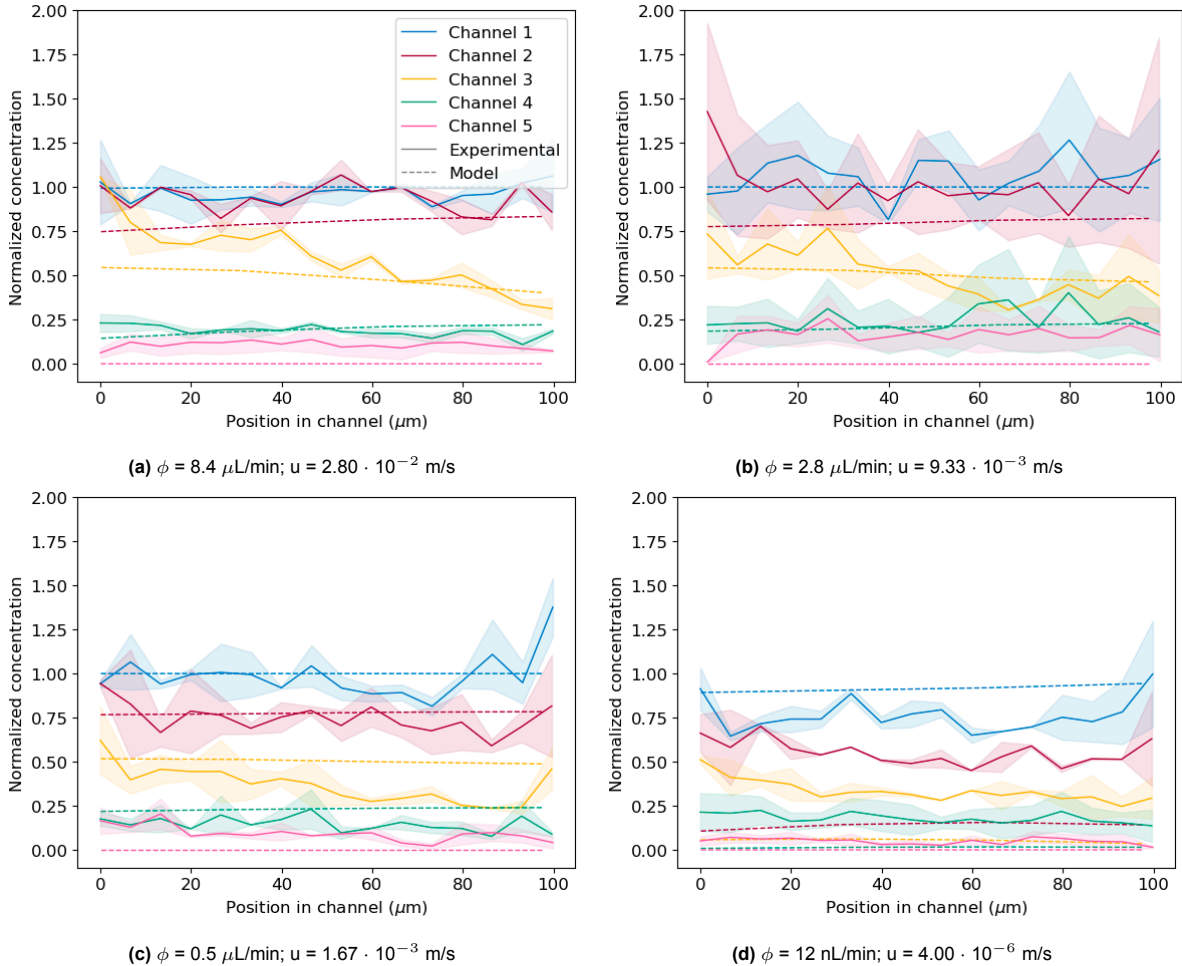
Figure 4.9: Experimental data from the μCGG velocity study compared to the model data. The results from four out of seven examined velocities are plotted as the normalized concentrations across the channel length. As a guide to the eye, the spread of the duplicates is shaded in the corresponding color. The normalized concentration calculated by the model is indicated with a dashed line in the corresponding color.

The normalized concentration profiles from the experiments were compared to those calculated with the adjusted 2D model (see Figure 4.9). The observed trends from the experimental data are also visible in the model data. For a flow rate of 8.4 μL/min, the concentrations of channels 1 and 2 and those of channels 4 and 5 are not as distinguished, and the concentration in channel 3 is not homogeneous. As the flow rate decreases to 0.5 μL/min the homogenization per channel and the spread between the concentrations of each of the channels is significantly improved. However, the normalized concentration values from the model calculations do not correspond directly to those from the LSM measurements. For the model predictions for $\phi0$ = 12 nL/min, the model predictions and the experimental data do not correspond. The RMSE of the model compared to the experimental data was calculated for each of the four μCGG flow rates and is given in Table 4.1. The smaller the RMSE, the higher the model prediction accuracy. The RMSE for $\phi0 = 8.4$ μL/min, $\phi0 = 2.8$ μL/min, and $\phi0 = 0.5$ μL/min is similar. The

RMSE for $\phi 0 = 12$ nL/min is 0.25, which is almost double the RMSE of the other $u0$ conditions. The RMSEs are relatively high as they are all higher than 10% of the maximum normalized concentration. Furthermore, these values confirm that for $\phi 0 = 12$ nL/min the prediction accuracy is especially poor. It should be noted that the RMSE is based on absolute errors. Even though the relative errors of the data points may be similar, the absolute errors may differ across the data. Thus the RMSE inherently assigns a variable weight to the different data points, which introduces bias into the prediction accuracy measurements. For example, in this case the errors of channels 1 and 2 are likely to have a higher weight as their absolute errors are higher than errors of channels 4 and 5.

Table 4.1: RMSE calculated for the four different μCGG velocity studies.

$\phi 0$	RMSE
8.4 μL/min	0.12
2.8 μL/min	0.15
0.5 μL/min	0.11
12 nL/min	0.25

Thus, this 2D model in COMSOL Multiphysics cannot be used to make highly accurate predictions about the concentration at a given location. This might be caused by the discretization method used by COMSOL Multiphysics (FEM) to solve the system of equations, which may result in numerical diffusion. Another reason for the discrepancy between the model and experimental data could be the diffusion coefficient used in the model ($D_{RB} = 3.6 \cdot 10^{-10}$ m^2/s). This value was derived from a relation in a paper by Abdul et al., 2005, but was not experimentally verified. Finally, the discrepancies could arrive from errors in the experimental setup and/or procedures. For example, the tracer molecule that was used (rhodamine B) stains the PDMS which may affect the measurements in an unexpected way. For informed decision making for dMSCC design it is desired to have higher prediction accuracy. Therefore, it was decided to explore the μCGG further with 2D models both in COMSOL Multiphysics and Ansys Fluent to see of prediction accuracy could be improved. This is further elaborated in section 4.3.4.

4.2.2. Ratio study with the new mixer velocity

To validate the model's capabilities to predict the dynamic system that moves the gradient across the chamber, a velocity ratio study was conducted (similar to the conditions in the stationary study). The measured intensities from the experiments and calculated concentrations from the model were assessed in lines 520, 1060, 1600, and 2140 (see Figure 3.7; the results of the other velocity ratios can be found in Appendix J). The results were normalized and plotted in Figure 4.10. In the experimental data, it can be seen that the normalized concentration exceeds 1. This is likely caused by the fact that the data were normalized to an average maximum intensity and no corrections could be performed for the location-specific exposure of the images. Also, it should be noted that the sudden peaks observed in experimental data across the lines at 500 μm, 1000 μm, 1500 μm, and 2000 μm correspond with the locations of the pillars and are therefore caused by rhodamine B staining of the PDMS pillars.

(a) $\phi 1 = 25.2\ \mu$L/min; $\phi 1 = 2.8\ \mu$L/min

(b) $\phi 1 = 14.0\ \mu$L/min; $\phi 1 = 14.0\ \mu$L/min

(c) $\phi 1 = 2.8\ \mu$L/min; $\phi 1 = 25.2\ \mu$L/min
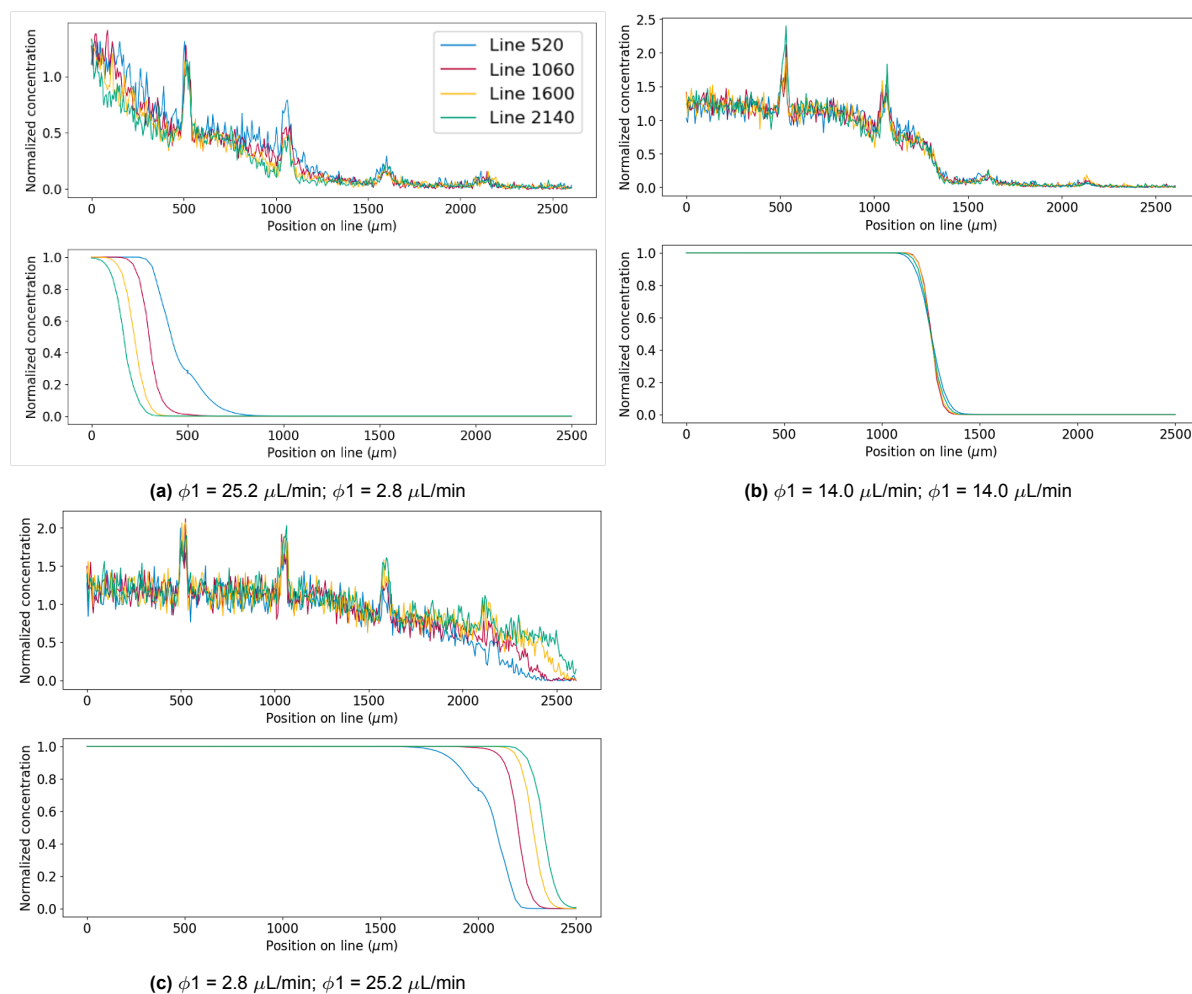
Figure 4.10: Results of the velocity ratio study. In each subfigure, the top graph shows the normalized concentration (it is assumed that the normalized intensity directly relates to the normalized concentration of rhodamine B). The bottom graph shows the corresponding model data (normalized concentration). Each subfigure corresponds with a different ratio between u1/u2 (the same ratios as A-C in Figure 4.1).

The experimental results show that indeed by changing the velocity ratio between the top and bottom inlet, the gradient is shifted across the width of the chamber. This is in line with the predicted results by the 2D COMSOL model. Furthermore, the results in four lines at four different locations were analyzed. In line 520, closest to the μCGG, the gradient is wider and not yet at the 'steady state location' [1]. In line 2140, the gradient is thinner and reaches the steady state location. This trend is also observed in the graphs depicting the model data.

Figure 4.11 shows the experimental and model results for all three ratios in line 2140 only. This plot shows that the prediction capabilities of the model for the chamber are much better compared to that for the μCGG. Only when pushing the gradient to the bottom of the chamber (towards position: 0 μm) the model and experimental data differ significantly: the gradient observed during the experiments is much wider than that calculated by the model. Also, this gradient is much wider than when the ratio pushes the gradient to other positions in the chamber. This is likely caused by PDMS staining with rhodamine B at the bottom part of the chamber during the experimental procedures (such as flushing at high fluid velocities to remove air bubbles). Although during these procedures a large ratio of u1/u2 is used to keep the rhodamine B as much away from the main body of the chamber, measurements at the bottom of the chamber are likely still influenced by staining.

---

[1] From the surface plots A and C in Figure 4.1, it is visible that some space is required for the gradient to be pushed to the desired location. This desired location is referred to as the 'steady state location'.
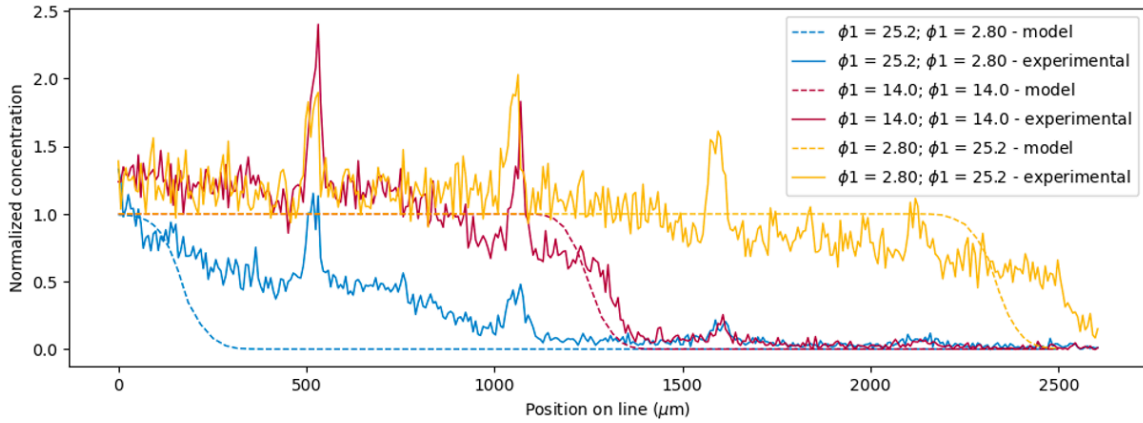
Figure 4.11: Experimental and model results in line 2140 for the three different velocity ratios (u1/u2).

For the velocity ratio study, the RMSE of the model compared to the experimental data was also cal-
culated. These values are shown in Table 4.2. From these values it seems that prediction accuracy
is reduced (higher RMSE) when the gradient is pushed more towards the upper side of the chamber
(as $\phi 1$ decreases and $\phi 2$ increases). This is likely caused by the fact that at more positions across the
lines the normalized concentration should be at the maximum. As mentioned previously, the RMSE
is based on absolute errors and these errors for the maximum concentrations prediction are generally
higher than for the minimum concnetration predictions (even though the relative errors are similar).
Thus, these errors have a bigger weight in the RMSE calculations, which is why the values seem to
increase as the ratio between $u1$ and $u2$ decreases. This is likely also the explanation as to why the
RMSEs are also higher than those calculated for the model predictions in the μCGG velocity ratio study.

Table 4.2: RMSE calculated for the three different velocity ratios between the top and bottom inlet.

$\phi 1$ (μL/min)	$\phi 2$ (μL/min)	RMSE
25.2	2.8	0.15
14.0	14.0	0.52
2.8	25.2	0.78

4.3. Optimization of the design

4.3.1. Adjusting the width of the chamber

One of the prerequisites of the new design was to improve amplitude control *without* compromising
the oscillation frequency that is already achieved in devices in the literature. The current switching fre-
quency of discretized levels is in the range of 5 seconds to a few minutes (Ho et al., 2022, Täuber et al.,
2022). Therefore, the time required for a steady state after each step ($\sim$30 s) in the time-dependent
study using the step function (section 4.1.3) is rather high. A possible solution to reduce this switching
time could be to adjust the width of the chamber.

In an early iteration of the current base case geometry, the width of the chamber was smaller because
the μCGG was not yet incorporated. Applying the step function (section 3.3.1 and Appendix E), the
observed change in concentration over time in point 1 shows that within only 2.5 seconds a steady state
is reached (see Figure 4.12). The dynamics in this geometry are therefore much faster compared to
the 30 seconds necessary to establish a 50 mol/m^3 change in the base case model. This suggests that
placing the inlets (connected to a μCGG) closer together increases the speed with which concentration
oscillations can be achieved. It should be noted that the absence of the μCGG in this geometry might
affect the results. However, it is expected that adding the μCGG only affects the required initialization
time.
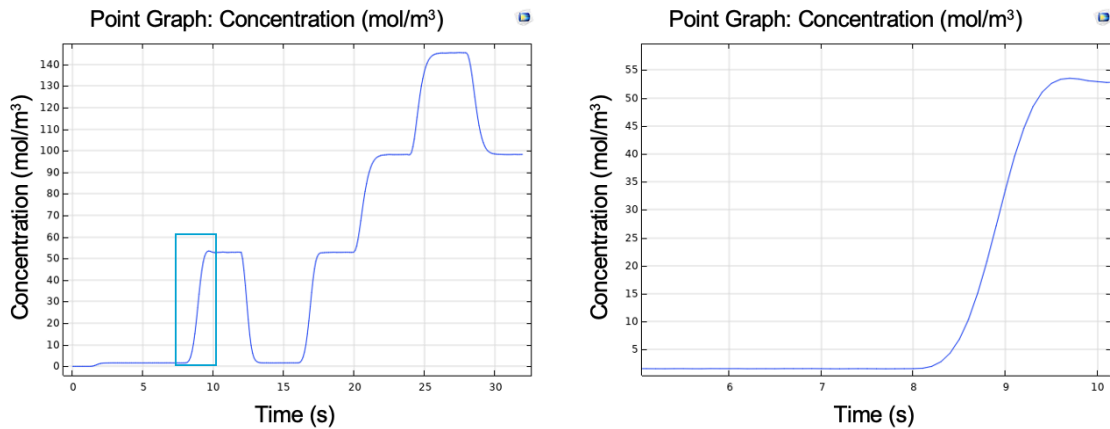
Figure 4.12: The observed concentration in point 1 of the adjusted geometry that has a chamber width of 1300 μm in a time dependent study (left). A zoom of the first step in the concentration profile (indicated with a blue box in the left graph) showing that a steady state concentration is already established after 2.5 seconds (right).

4.3.2. Adjusting the spacing between the μCGG outlets

Another limitation of the base case geometry is the width of the gradient that is established. In the base case model, the width of the gradient is only ~400 μm. The 2D cultivation chambers used by the Grünberger group are monolayer growth chambers (MGCs) which are ~80 μm wide (Täuber et al., 2020, Ho et al., 2022, Grünberger et al., 2015). These cultivation chambers are open on two sides to minimize the time necessary for the diffusion of solutes into the cultivation chamber. Therefore, a very different concentration would be observed at one side of the MGC compared to the other side. By widening the gradient, less severe differences would be observed between the two sides of an MGC. One possibility to increase the width of the gradient would be to increase the spacing between the μCGG outlets. In the base case geometry, this spacing is 500 μm. Variations to this design were made which have a spacing of 750 μm, 1000 μm, and 1500 μm. The effect of this adjusted spacing was analyzed with the models with 500 μm and 750 μm spacing. The results in Figure 4.13 show that the width of the gradient in the base case model (500 μm spacing) is 766 μm wide and the gradient in the adjusted geometry (750 μm spacing) is 977 μm. Thus the wider spaced μCGG outlets do result in a wider concentration gradient. However, the difference is only 210 μm while the total width of the chamber increases by 1500 μm. Considering the effect of the total chamber width on the oscillation frequency capabilities of the system, an alternative to increase the gradient width is preferred.

(a) Spacing: 500 μm

(b) Spacing: 750 μm
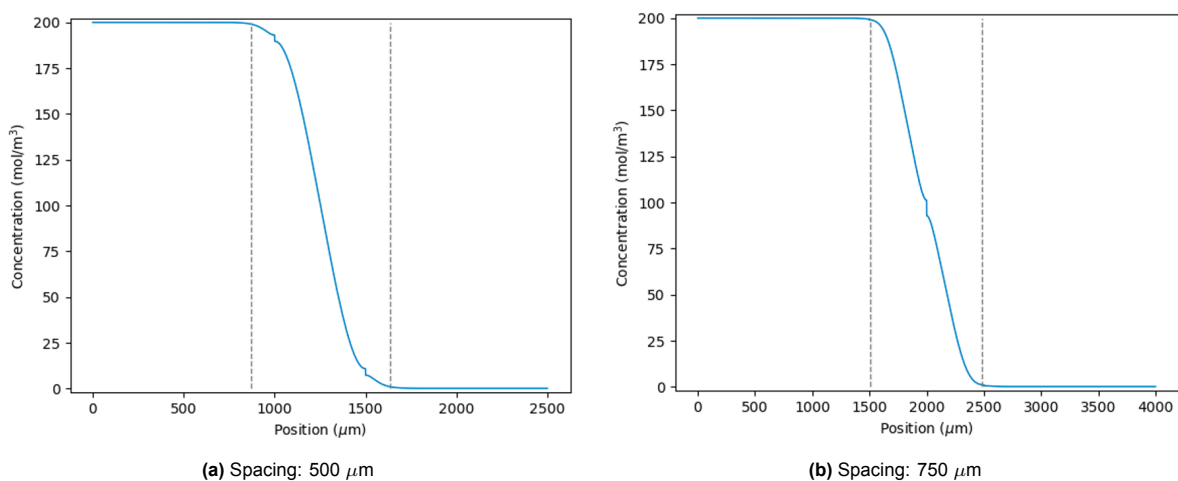
Figure 4.13: The concentration in line 4, for both the base case model (500 μm spacing) and the adjusted model (750 μm spacing). A stationary study was conducted where $u0 = 6.66 \cdot 10^{-4}$ m/s and $u1 = u2 = 3.33 \cdot 10^{-3}$ m/s. The grey dashed lines indicate the start and end of the gradient in the chamber.

4.3.3. Adjusting the ratio between velocities $u0$ and u_{max}

To see if the width of the established gradient can be increased by increasing the ratio of $u0$ / u_{max}, a stationary study was conducted with the base case model where three different $u0$ were tested while keeping u_{max} constant. The concentrations observed in line 2140 are shown in Figure 4.14. This graph clearly shows that the gradient is approximately three times wider when this ratio is increased from $1.67 \cdot 10^{-3}$ m/s to $9.33 \cdot 10^{-3}$ m/s. However, it was seen that the higher the ratio between $u0$ and u_{max}, the harder it becomes to switch between the maximum and minimum concentration. To quantify this effect, it is suggested that a sensitivity analysis of the ratio $u0/u_{max}$ could be conducted. Furthermore, from the experimental study where different μCGG velocities were tested (section 4.2.1), it was seen that the μCGG does not mix well when $u0$ becomes too high. Thus, when a wider gradient is desired, the μCGG geometry should be adjusted to improve mixing capabilities or u_{max} should be changed rather than $u0$ to avoid mixing complications. Finally, it should be noted that increasing the ratio between $u0$ and u_{max} may also affect the response time of the chip which should be investigated before making such adjustments.
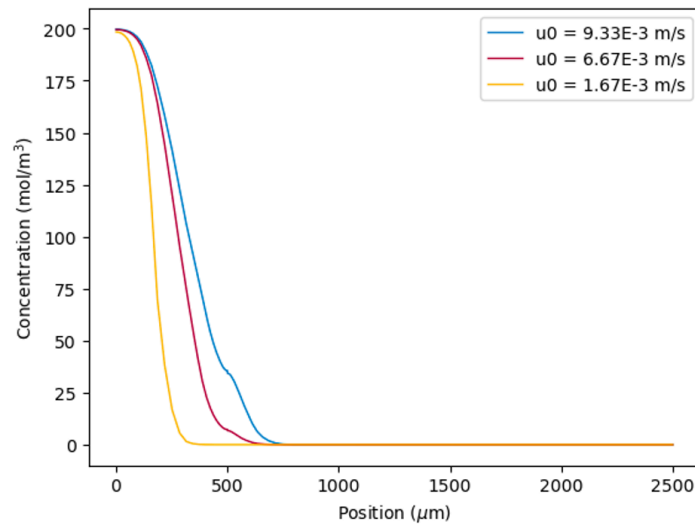
Figure 4.14: The concentration measured in line 2140 for the three different $u0$ that were analyzed in a stationary study.

4.3.4. μCGG modelling in Ansys Fluent

The accuracy of the COMSOL Multiphysics model with regards to the μCGG and the limitations of the μCGG geometry are further explored in this section. The μCGG was modelled separately in both COMSOL Multiphysics and Ansys Fluent, and a stationary study was conducted. The surface plots of both models (Figure 4.15) show that concentration profile in Ansys Fluent resemble much better the rhodamine B intensity profile observed in during experiments (see LSM image in Figure 4.16). As can be seen from Figure 4.16, the top two μCGG outlets have similar concentrations, the bottom two outlets also have similar concentrations, and the middle inlet shows a gradient between the maximum and minimum concentration. This is similar to the results obtained with Ansys Fluent, while the COMSOL Multiphysics model predicts a different concentration at every outlet that is more homogeneous.
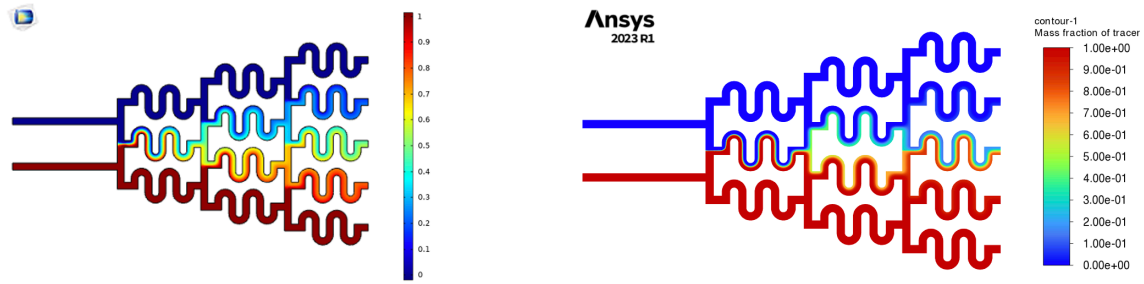
Figure 4.15: Surface plot of the concentration profile of the μCGG model in both COMSOL Multiphysics (left) and Ansys Fluent (right) where $\phi 0 = 2.8 \mu L/min$.
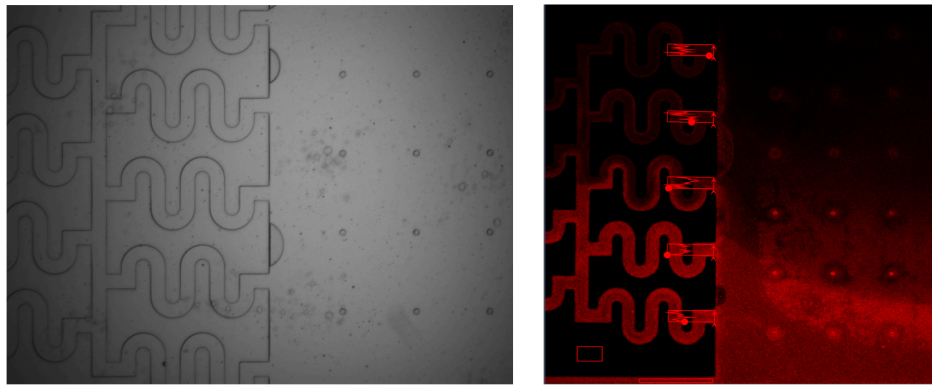
Figure 4.16: Figure 4.7 revisited. The WF (left) and LSM (right) image of the μCGG velocity study where $\phi 0 = 2.8 \mu L/min$.

Figure 4.17 compares these experimental results with the models quantitatively per channel. Here it can be seen that for channel 1, both COMSOL Multiphysics and Ansys Fluent predict the experimental values well. For channel 2, the Ansys Fluent model corresponds better with the experimental data. For channel 3, the experimental data seems to be in between the predictions of the COMSOL Mulit-physics model and the Ansys Fluent model. However, Ansys Fluent does capture the presence of the concentration gradient across the channel better. Whereas COMSOL Multiphysics shows a more homogeneous concentration distribution across the channel. For channel 4, COMSOL Multiphysics seems to predict the concentration better than Ansys Fluent. For channel 5, both models have a similar inaccuracy in their prediction.

These observed trends are confirmed and summarized by the RMSE values of each channel (Table 4.3). The overall RMSE values show that COMSOL Multiphysics actually has a higher prediction accuracy than Ansys Fluent. However, there are some unexpected results in the experimental data that influence the RMSE calculations. In channels 4 and 5 (Figure 4.17d and 4.17e), the experimental data shows a normalized concentration that is $\sim$0.2 across the channel. This similarity between the two channels is likely caused by PDMS staining, resulting in background noise that is captured in the measurements. Thus, contrary to the COMSOL Multiphysics model, the concentration profiles of channel 4 and 5 should be similar. This effect is captured by the Ansys Fluent model. To get RMSE results that better capture the expected trends, future experimental and/or modelling studies should take this into account by using another tracer molecule that is less prone to stain the PDMS or by performing correction calculations on either the model or experimental data.

Table 4.3: RMSE calculated for the μCGG model in both COMSOL Mulitphysics and Ansys Fluent.

Channel	RMSE COMSOL Multiphysics	RMSE Ansys Fluent
1	0.11	0.11
2	0.21	0.10
3	0.09	0.14
4	0.08	0.23
5	0.17	0.17
All	0.14	0.14

(a) Channel 1

(b) Channel 2

(c) Channel 3

(d) Channel 4

(e) Channel 5
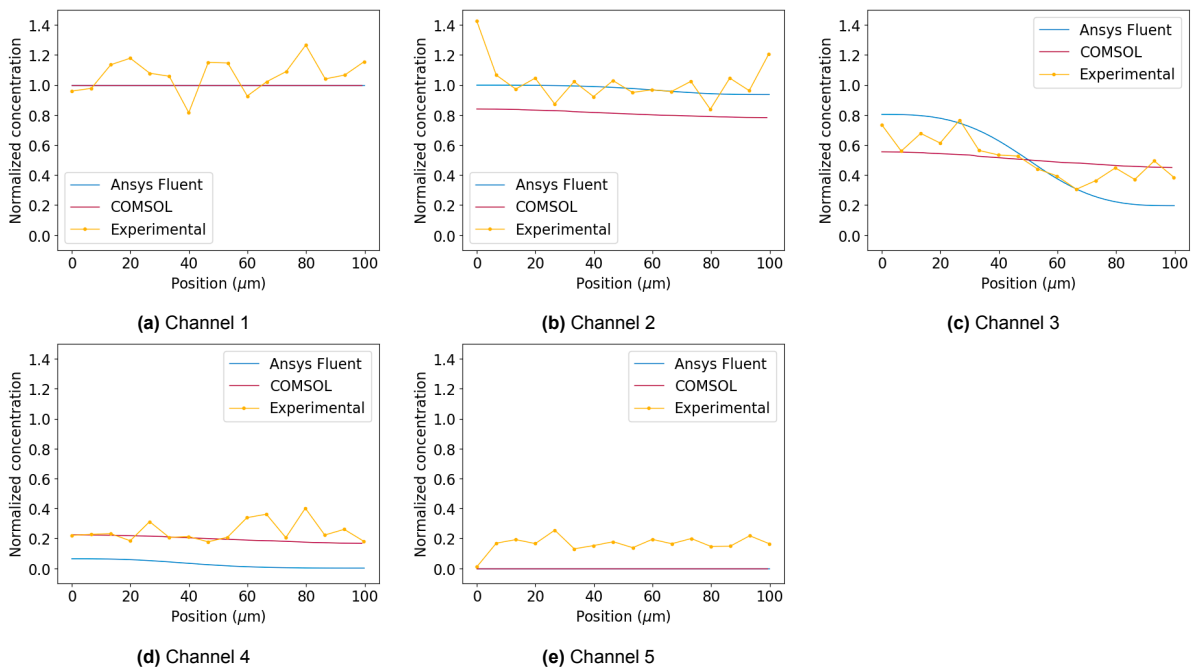
Figure 4.17: COMSOL vs Ansys Fluent: $\phi0$ = 2.8 μL/min; u0 = 9.33 $\cdot$ 10^3 m/s

Previous results have shown that the current design of the μCGG has limitations that prevent proper mixing under certain circumstances. To identify the combinations of the diffusion coefficient (D_i) and μCGG velocity ($u0$) for which the μCGG design can be used, a DoE was conducted with the Ansys Fluent model of the μCGG. The DoE calculated the normalized difference in concentration across the concentration profile in outlet 3. The more homogeneous the concentration at the outlet of the channel, the higher the correlation number. These results are shown in Figure 4.18. Here it can be seen that as expected, when the diffusion coefficient is higher (read: faster diffusion), and the fluid velocity is lower (read: more time for mixing), the more homogeneous the concentration at the outlet of channel 3, and vice versa. From Figure 4.18 for diffusion coefficient and velocity combinations in the purple region, the use of the current μCGG design results in well mixed outlet concentrations (in channel 3). When the combination of diffusion coefficient and desired fluid velocity lies within the colored regions, proper mixing no longer occurs resulting in heterogeneous concentration profiles at the outlets of the μCGG. For future studies where the diffusion coefficient and fluid velocity of the μCGG are sub-optimal for the current design, the serpentine channel geometry can be elongated to increase residence time and thereby improve mixing.
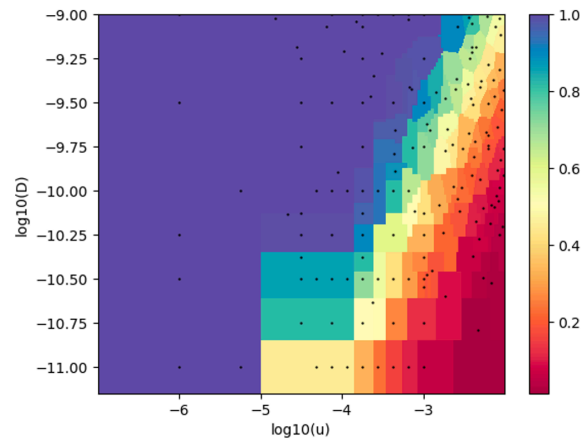
Figure 4.18: Heat map of the design space of the DoE showing the log10 of the diffusion coefficient on the y-axis and the log10 of the fluid velocity on the x-axis. The black points indicate the design points that were used in the in the DoE. The color of the heat map corresponds with the normalized ratio of the minimum and maximum concentration value observed at the outlet of channel 3.

5

Conclusions

In this thesis, the research question *'What is necessary to mimic environmental lifelines at a microfluidic scale?'* was addressed by identifying a new design for a dMSCC device that may improve on the amplitude control of existing devices while maintaining the high temporal resolution. This new dynamic μCGG based design was analyzed this with a 2D model, which was experimentally validated. The following can be concluded from this research:

1. The stationary and time-dependent studies show that the mechanism of the dMSCC design, that pushes a gradient across the chamber by changing ratio of the fluid velocity at the top and bottom inlets, indeed works and can be used to create concentration profiles that mimic discrete and smooth lifelines at a desired location in the chamber. However, the response time of 30 seconds is relatively high compared to those from dMSCC devices in literature.

2. The mesh independence study shows that results obtained with different mesh refinements deviate only by 2% compared to the most refined mesh. It should be noted that, when more complex geometric structures are placed in the design, this deviation in the obtained results is highest.

3. The experimental results showed that the 2D COMSOL Multiphysics model predicts observed trends not very well at the outlets of the μCGG with RMSEs ranging between 0.1 and 0.25 (>10% of the experimental data). Inside the chamber, the observed trends are captured well by the model, although the RMSEs are much larger than for the outlets of the μCGG (ranging from 0.1 to 0.75). However, these high values are caused by discrepancies in the experimental data and should therefore be further investigated.

4. Furthermore, the μCGG velocity study revealed that by increasing the fluid velocity inside the μCGG, more heterogeneity of the concentration profile is observed in the third outlet of the μCGG, while the concentration profiles in channel 1 and 2 are the same as well as the concentration profiles in channel 4 and 5. Thus, a higher μCGG velocity results in a not well-mixed situation, preventing the μCGG from generating the desired gradient. This is likely caused by the distance of the serpentine channels that is too short to achieve enough residence time for mixing.

Based on these results, some optimization studies were conducted to improve the design. The following conclusions were derived:

1. Decreasing the width of the chamber from 3700 μ to 3100 μm increases the response time of the chip from 30 s to 2.5 s.

2. Increasing the space between the μCGG outlets from 500 μm to 750 μm increases the width of the gradient by three-fold and increasing the fluid velocity inside the μCGG from $6.67 \cdot 10^{-3}$ m/s to $9.33 \cdot 10^{-3}$ m/s while keeping u_{max} constant also increases the width of the gradient approximately three-fold. However, the latter solution is preferred since this will not affect the response time of the chip.

3. The μCGG was separately modelled in both COMSOL Multiphysics and Ansys Fluent, to see if higher prediction accuracy could be reached. It was found that although observed experimental trends are better captured by the Ansys Fluent model, the prediction accuracy of the Ansys Fluent model were lower (RMSE=0.15) than that of the COMSOL Multiphysics model (RMSE=0.14).

4. A DoE revealed that the current μCGG design can be used for fluid velocities inside the μCGG preferably lower than $1 \cdot 10^{-5}$ m/s and tracers with diffusion coefficient preferably as high as possible.

6

Recommendations

In the results and discussion chapter, recommendations for future research are made that may improve on the work performed in this thesis. For the time-dependent studies a delay was observed at the far end of the chamber. In order to gain deeper insights into the underlying causes of these delays and potentially develop strategies to mitigate them, it is recommended to conduct further time-dependent studies, focusing on other locations of interest, such as point 2, analogous to the approach undertaken in the current investigation for point 1. Furthermore, the slight delays that were observed in point 1 could be prevented by increasing initialization times with 2-5 seconds.

The experimental validation process revealed that the length of the serpentine channels was inadequate to facilitate sufficient residence time for effective mixing. To avoid potential complications arising from this limitation, it is recommended to extend the length of the channels. Also, when comparing the experimental results with the model, the RMSE was used as a metric to assess the prediction accuracy. Nevertheless, it is worth noting that the RMSE, being based on absolute errors, inherently assigns varying weights to different data points, potentially introducing bias in the analysis. To prevent this potential bias, it is recommended to do a statistical analysis to find a more appropriate measure that accounts for the relative significance of data points. By adopting such an approach, a more robust and equitable assessment of the prediction accuracy can be achieved. Furthermore, it was found that the prediction accuracy of the COMSOL Multiphysics model was not extremely high. Several factors potentially contributing to this limited accuracy can be considered, such as the utilization of parameters, including the diffusion coefficient, which were not experimentally validated. Hence, it is recommended that these are experimentally validated to improve reliability of the model predictions. Also, a thorough evaluation of the experimental protocols is essential to ensure accurate and precise results. Especially the use of rhodamine B as tracer molecule, which is prone to stain the PDMS material. Finally, the flux-based pump system could be replaced with a more robust pump system (e.g. pressure-driven) to improve control over the experiments.

Optimization studies have demonstrated that decreasing the width of the chamber leads to an increase in the response time of the chip. Moreover, adjusting either the width between the outlets of the μCGG or the ratio between the velocity within the μCGG and the maximum velocity results in an increased width of the gradient. It is therefore recommended for future research to implement these findings. If the latter optimization approach, involving an increase in the gradient width through adjusting the velocity ratio, is chosen, it is recommended to conduct a sensitivity analysis to assess the impact on both the temporal resolution of the device and the control of concentration amplitude.

This thesis primarily focused on the experimental validation of stationary studies. However, considering the ultimate objective of the dMSCC device, which is to replicate microbial lifelines over time, it is highly recommended to conduct experimental validation of the mechanism in time-dependent studies. This would provide crucial insights into the device's performance and its ability to accurately mimic dynamic environmental conditions.

Furthermore, this thesis does not consider the design and implementation of a cell trap, such as a cultivation chamber. By exploring the design and implementation of a cell trap, the research would

encompass a more holistic understanding of the dMSCC device, improving its functionality and applicability in facilitating cellular cultivation and lifeline analysis. Therefore, it is recommended to conduct further research into this aspect as the next step.

To conclude, this thesis focuses only on a single dMSCC device design, which was conceptualized to address the research objective of enhancing amplitude control while preserving temporal resolution compared to existing devices. However, as highlighted in the introduction, there are a multitude of limitations to dMSCC devices that are still subject to improvement. Consequently, it is highly recommended to assess the feasibility of this design in mitigating those aforementioned limitations and compare it with alternative dMSCC device designs. Recognizing that a singular approach may not be universally applicable, these comparative analyses will help identify the most suitable design for specific applications, acknowledging the need for tailored solutions.

References

Abdul, R. S., Betsey, P., & S, S. P. (2005). Rapid Diffusion of Fluorescent Tracers into Staphylococcus epidermidis Biofilms Visualized by Time Lapse Microscopy. *Antimicrobial Agents and Chemotherapy*, *49*(2), 728–732. https://doi.org/10.1128/AAC.49.2.728-732.2005

Bahnemann, J., & Grünberger, A. (2022). Microfluidics in Biotechnology: Overview and Status Quo. In J. Bahnemann & A. Grünberger (Eds.), *Microfluidics in biotechnology* (pp. 1–16). Springer International Publishing. https://doi.org/10.1007/10{_}2022{_}206

Blöbaum, L., Haringa, C., & Grünberger, A. (2022). Microbial lifelines in bioprocesses: From concept to application. *Biotechnology Advances*, 108071. https://doi.org/https://doi.org/10.1016/j.biotechadv.2022.108071

COMSOL. (2022a). Choosing the Right Linear System Solver. https://doc.comsol.com/5.5/doc/com.comsol.help.comsol/comsol_ref_solver.27.118.html

COMSOL. (2022b). Fully Coupled. https://doc.comsol.com/5.5/doc/com.comsol.help.comsol/comsol_ref_solver.27.149.html

COMSOL. (2022c). Settings for the Discretization Sections. https://doc.comsol.com/5.5/doc/com.comsol.help.comsol/comsol_ref_equationbased.23.019.html

de Coninck, H., Revi, A., Babiker, M., Bertoldi, P., Buckeridge, M., Cartwright, A., Dong, W., Ford, J., Fuss, S., Hourcade, J.-C., Ley, D., Mechler, R., & Newman, P. (2022). Strengthening and Implementing the Global Response. In V. Masson-Delmotte, P. Zhai, H.-O. Portner, D. Roberts, J. Skea, P. Shukla, A. Pirani, W. Moufouma-Okia, C. Pean, R. Pidcock, S. Connors, J. Matthews, Y. Chen, X. Zhou, M. Gomis, E. Lonnoy, T. Maycock, M. Tignor, & T. Waterfield (Eds.), *Global warming of 1.5°c* (pp. 313–444). Cambridge University Press. https://doi.org/10.1017/9781009157940.006

Delvigne, F., Takors, R., Mudde, R., van Gulik, W., & Noorman, H. (2017). Bioprocess scale-up/down as integrative enabling technology: from fluid mechanics to systems biology and beyond. *Microbial Biotechnology*, *10*(5), 1267–1274. https://doi.org/10.1111/1751-7915.12803

Dusny, C., & Grünberger, A. (2020). Microfluidic single-cell analysis in biotechnology: from monitoring towards understanding. *Current Opinion in Biotechnology*, *63*, 26–33. https://doi.org/https://doi.org/10.1016/j.copbio.2019.11.001

Fogler, H. S. (2017). Models for Nonideal Reactors. In *Elements of chemical reaction engineering*. Pearson.

Formenti, L. R., Nørregaard, A., Bolic, A., Hernandez, D. Q., Hagemann, T., Heins, A.-L., Larsson, H., Mears, L., Mauricio-Iglesias, M., Krühne, U., & Gernaey, K. V. (2014). Challenges in industrial fermentation technology research. *Biotechnology Journal*, *9*(6), 727–738. https://doi.org/https://doi.org/10.1002/biot.201300236

Giridharan, V., Yun, Y., Hajdu, P., Conforti, L., Collins, B., Jang, Y., & Sankar, J. (2012). Microfluidic Platforms for Evaluation of Nanobiomaterials: A Review (H. Chen, Ed.). *Journal of Nanomaterials*, *2012*, 789841. https://doi.org/10.1155/2012/789841

Grünberger, A., Probst, C., Helfrich, S., Nanda, A., Stute, B., Wiechert, W., von Lieres, E., Nöh, K., Frunzke, J., & Kohlheyer, D. (2015). Spatiotemporal microbial single-cell analysis using a high-throughput microfluidics cultivation platform. *Cytometry Part A*, *87*(12), 1101–1115. https://doi.org/https://doi.org/10.1002/cyto.a.22779

Grünberger, A., Wiechert, W., & Kohlheyer, D. (2014). Single-cell microfluidics: opportunity for bioprocess development. *Current Opinion in Biotechnology*, *29*, 15–23. https://doi.org/https://doi.org/10.1016/j.copbio.2014.02.008

Gudiño, N. (2022). Developing scalable bioprocesses: lessons and examples from industry.

Gupta, V., Sengupta, M., Prakash, J., & Tripathy, B. C. (2017). An Introduction to Biotechnology. In V. Gupta, M. Sengupta, J. Prakash, & B. C. Tripathy (Eds.), *Basic and applied aspects of biotechnology* (pp. 1–21). Springer Singapore. https://doi.org/10.1007/978-981-10-0875-7{_}1

Haringa, C., Deshmukh, A. T., Mudde, R. F., & Noorman, H. J. (2017). Euler-Lagrange analysis towards representative down-scaling of a 22m3 aerobic S. cerevisiae fermentation. *Chemical Engineering Science*, *170*, 653–669. https://doi.org/https://doi.org/10.1016/j.ces.2017.01.014

Haringa, C., Mudde, R. F., & Noorman, H. J. (2018). From industrial fermentor to CFD-guided downscaling: what have we learned? *Biochemical Engineering Journal*, *140*, 57–71. https://doi.org/https://doi.org/10.1016/j.bej.2018.09.001

Haringa, C., Tang, W., Deshmukh, A. T., Xia, J., Reuss, M., Heijnen, J. J., Mudde, R. F., & Noorman, H. J. (2016). Euler-Lagrange computational fluid dynamics for (bio)reactor scale down: An analysis of organism lifelines. *Engineering in Life Sciences*, *16*(7), 652–663. https://doi.org/https://doi.org/10.1002/elsc.201600061

Heijen, S., Noorman, H., & van der Lans, R. (2015). Bioprocess Engineering Part III Design and Scale up of Bioreactors Chapter 17 Characteristic times. Why and how?

Hille, B. (2001). Ion channels of excitable membranes. Sinauer Associates Inc.

Ho, P., Täuber, S., Stute, B., Grünberger, A., & von Lieres, E. (2022). Microfluidic Reproduction of Dynamic Bioreactor Environment Based on Computational Lifelines. *Frontiers in Chemical Engineering*, *4*. https://doi.org/10.3389/fceng.2022.826485

Ho, P., Westerwalbesloh, C., Kaganovitch, E., Grünberger, A., Neubauer, P., Kohlheyer, D., & von Lieres, E. (2019). Reproduction of large-scale bioreactor conditions on microfluidic chips. *Microorganisms*, *7*(4). https://doi.org/10.3390/microorganisms7040105

Jeon, N. L., Dertinger, S. K. W., Chiu, D. T., Choi, I. S., Stroock, A. D., & Whitesides, G. M. (2000). Generation of Solution and Surface Gradients Using Microfluidic Systems. *Langmuir*, *16*(22), 8311–8316. https://doi.org/10.1021/la000600b

Kaiser, M., Jug, F., Julou, T., Deshpande, S., Pfohl, T., Silander, O. K., Myers, G., & van Nimwegen, E. (2018). Monitoring single-cell gene regulation under dynamically controllable conditions with integrated microfluidics and software. *Nature Communications*, *9*(1), 212. https://doi.org/10.1038/s41467-017-02505-0

Leygeber, M., Lindemann, D., Sachs, C. C., Kaganovitch, E., Wiechert, W., Nöh, K., & Kohlheyer, D. (2019). Analyzing Microbial Population Heterogeneity—Expanding the Toolbox of Microfluidic Single-Cell Cultivations. *Journal of Molecular Biology*, *431*(23), 4569–4588. https://doi.org/https://doi.org/10.1016/j.jmb.2019.04.025

Moreau, M., Di Miceli Raimondi, N., Le Sauze, N., Gourdon, C., & Cabassud, M. (2017). A new numerical method for axial dispersion characterization in microreactors. *Chemical Engineering Science*, *168*, 178–188. https://doi.org/10.1016/j.ces.2017.04.040

Nauman, E. B., & Mallikarjun, R. (1983). Generalized boundary conditions for the axial dispersion model. *The Chemical Engineering Journal*, *26*(3), 231–237. https://doi.org/https://doi.org/10.1016/0300-9467(83)80018-5

Noorman, H. J., & Heijnen, J. J. (2017). Biochemical engineering's grand adventure. *Chemical Engineering Science*, *170*, 677–693. https://doi.org/https://doi.org/10.1016/j.ces.2016.12.065

Oosterhuis, N. (1984). *Scale-up of bioreactors: A scale-down approach* (Doctoral dissertation). Delft University of Technology. Delft.

Philips, R., Kondev, J., & Theriot, J. (2009). "Rule of thumb" for density of water. In *Physical biology of the cell* (p. 26). https://bionumbers.hms.harvard.edu/bionumber.aspx?s=n&v=5&id=103775

Picioreanu, C., Noorman, H., Haringa, C., Villa, C., Troost, I., & Haaksma, C. (2019). Scale Up Scale Down - CH3181.

Picioreanu, C. (2020). Numerical Methods, Modelling, and Simulation Techniques - LM3761 - Lecture 8.

Sanka, R., Lippai, J., Samarasekera, D., Nemsick, S., & Densmore, D. (2019). 3DμF - Interactive Design Environment for Continuous Flow Microfluidic Devices. *Scientific Reports*, *9*(1), 9166. https://doi.org/10.1038/s41598-019-45623-z

Silavwe, D. D., Brink, I. C., & Wallis, S. G. (2019). Assessment of some numerical methods for estimating the parameters of the one-dimensional advection–dispersion model. *Acta Geophysica*, *67*(3), 999–1016. https://doi.org/10.1007/s11600-019-00293-3

Stein, W. D. (1990). Channels, carriers and pumps An introduction to Membrane Transport. In *Academic press inc.* (p. 32). Harcourt Brace Jovanovich.

Sweet, E., Yang, B., Chen, J., Vickerman, R., Lin, Y., Long, A., Jacobs, E., Wu, T., Mercier, C., Jew, R., Attal, Y., Liu, S., Chang, A., & Lin, L. (2020). 3D microfluidic gradient generator for combination

antimicrobial susceptibility testing. *Microsystems & Nanoengineering*, *6*(1), 92. https://doi.org/10.1038/s41378-020-00200-7

Tajsoleiman, T., Mears, L., Krühne, U., Gernaey, K. V., & Cornelissen, S. (2019). An Industrial Perspective on Scale-Down Challenges Using Miniaturized Bioreactors. *Trends in Biotechnology*, *37*(7), 697–706. https://doi.org/https://doi.org/10.1016/j.tibtech.2019.01.002

Tang, S. K. Y., & Whitesides, G. M. (2010). Basic Microfluidic and Soft Lithographic Techniques. In Y. Fainman, D. Psaltis, & C. Yang (Eds.), *Optofluidics: Fundamentals, devices, and applications* (First edition.). McGraw-Hill Education. https://www.accessengineeringlibrary.com/content/book/9780071601566/chapter/chapter2

Täuber, S., Blöbaum, L., Steier, V., Oldiges, M., & Grünberger, A. (2022). Microfluidic single-cell scale-down bioreactors: A proof-of-concept for the growth of Corynebacterium glutamicum at oscillating pH values. *Biotechnology and Bioengineering*, *119*(11), 3194–3209. https://doi.org/10.1002/bit.28208

Täuber, S., Golze, C., Ho, P., von Lieres, E., & Grünberger, A. (2020). dMSCC: a microfluidic platform for microbial single-cell cultivation of Corynebacterium glutamicum under dynamic environmental medium conditions. *Lab on a Chip*, *20*(23), 4442–4455. https://doi.org/10.1039/D0LC00711K

Täuber, S., & Grünberger, A. (2023). Microfluidic single-cell scale-down systems: introduction, application, and future challenges. *Current Opinion in Biotechnology*, *81*, 102915. https://doi.org/https://doi.org/10.1016/j.copbio.2023.102915

Timmis, K., de Vos, W. M., Ramos, J. L., Vlaeminck, S. E., Prieto, A., Danchin, A., Verstraete, W., de Lorenzo, V., Lee, S. Y., Brüssow, H., Timmis, J. K., & Singh, B. K. (2017). The contribution of microbial biotechnology to sustainable development goals. *Microbial Biotechnology*, *10*(5), 984–987. https://doi.org/https://doi.org/10.1111/1751-7915.12818

Yu, C., Yu, C., Cui, L., Song, Z., Zhao, X., Ma, Y., & Jiang, L. (2016). Facile Preparation of the Porous PDMS Oil-Absorbent for Oil/Water Separation. *Advanced Materials Interfaces*, *4*. https://doi.org/10.1002/admi.201600862

<div style="text-align: right; font-size: 3em;">A</div>

1D Time-dependent
convection-dispersion model

A.1. Model set-up

Based on the results of the characteristic time calculations, it was decided to investigate the interaction between convection and axial dispersion with a 1D model. In this model, a plug flow is assumed. Therefore, the system is simplified by reducing the 3D geometry to a 1D line which represents the channel. This is graphically shown in Figure A.1.
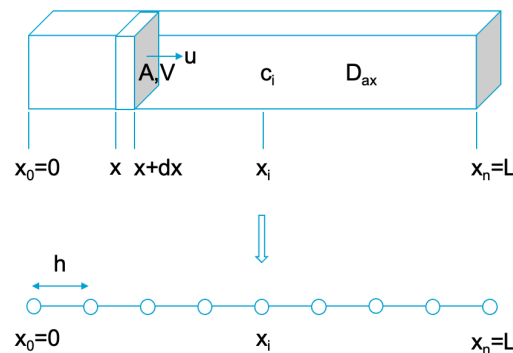
Figure A.1: Schematic overview of a plug flow in a straight microfluidic channel and its 1D representation.

The change of concentration caused by convection and dispersion to and from the infinitesimal volume *V* can be summarized into balance equation A.1.

$$V\frac{\partial C}{\partial t} = +AuC|_x - AuC|_{x+dx} - AD_{ax}\frac{\partial C}{\partial x}\Big|_x + AD_{ax}\frac{\partial C}{\partial x}\Big|_{x+dx} \quad \text{where} \quad V = Adx \quad \text{(A.1)}$$

Dividing the right-hand side by the volume ($V = Adx$) and rearranging the equation accordingly, gives the 1D second-order PDE for time-dependent convection and dispersion (equation 2.6). Here, the left-hand side is the concentration change over time. On the right-hand side, the first term is the second-order ordinary differential equation (ODE) system that accounts for the dispersion in the system. The second term is the first-order ODE system that accounts for the convection.

$$\frac{\partial c_i}{\partial t} = D_{ax}\frac{\partial^2 c_i}{\partial x^2} - u\frac{\partial c_i}{\partial x} \quad \text{(2.6 revisited)}$$

The finite differences method (FDM) is used as a discretization scheme, a method commonly applied to solve (non-)linear systems of equations. FDM applies Taylor's series expansion to obtain an approximation of the second-order ODE in the first term and the first-order ODE in the second term. For the approximation for the first-order ODE the backward difference approximation is used (equation A.2);

for the second-order ODE the centered difference approximation is used (equation A.3) (Picioreanu, 2020).

$$\frac{dC}{dx}\bigg|_{x_i} \approx \frac{C_{i+1} - C_i}{h} \tag{A.2}$$

$$\frac{d^2C}{dx^2}\bigg|_{x_i} \approx \frac{C_{i+1} - 2C_i + C_{i-1}}{h^2} \tag{A.3}$$

Substituting these approximations into equation 2.6 yields equation A.4. Together with the boundary conditions, which will be addressed in the next paragraph, a set of algebraic equations is established (equations A.4 - A.6).

$$\frac{\partial c_i}{\partial t} = D_{ax}\frac{C_{i+1} - 2C_i + C_{i-1}}{h^2} - u\frac{C_{i+1} - C_i}{h} \tag{A.4}$$

Danckwert's boundary conditions are applied to solve this system of equations (equations A.5 A.6). These conditions describe an already established flow that enters the system at the inlet ($x = 0$) and assumes a no-dispersion condition at the outlet of the system ($x = L$) (Nauman and Mallikarjun, 1983).

$$x = 0 \rightarrow uc_i - D_i\frac{\partial c_i}{\partial x} = uc_{in,i} \tag{A.5}$$

$$x = L \rightarrow \frac{\partial c_i}{\partial x_i} = 0 \tag{A.6}$$

The initial solute concentration was 0 mol/m^3. A solution to this problem is obtained with the initial value problem solver that applies the Radau algorithm (see Appendix C for the source code). The parameter settings that were used to solve the problem can be found in the source code (Appendix C).

A.2. Model verification

An analytical solution to the convection-dispersion model was used to generate synthetic data that was used to verify the 1D model. This analytical solution is given by equation A.7 (Silavwe et al., 2019).

$$\phi(x,t) = \frac{M}{A\sqrt{4\pi D_m t}}exp(-\frac{(x - ut)^2}{4D_m t}) \tag{A.7}$$

The analytical solution and the results of the 1D model were solved for the case study of the spread of a pollutant in a river, as described by Silavwe et al. (2019). The results for $x = 40$ m, $x = 60$ m, and $x = 80$ m are shown in Figure A.2. Here it can be seen that the predicted concentration at a given location over time is very similar between the 1D model and the analytical solution. The sum of squared errors (SSE) of $1.831 \cdot 10^{-3}$ g^2/(m^3)^2 confirms this. The models used in Silavwe et al. (2019) all showed SSEs ranging between $0 - 1 \cdot 10^{-2}$ g^2/(m^3)^2, thus the model is comparable to these models in literature.
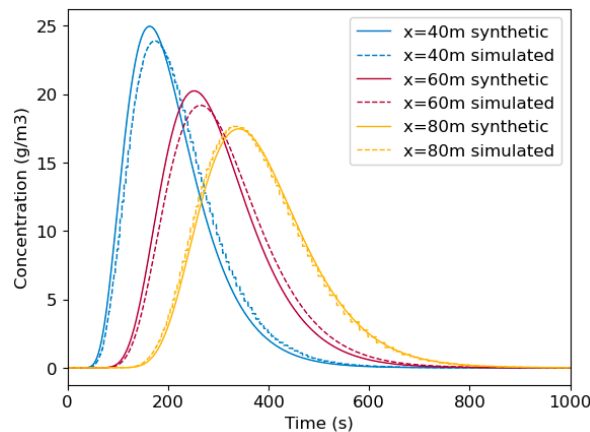
Figure A.2: The results of the 1D time-dependent convection-dispersion model. At $t = 0$, 1 kg of solute (pollutant with $D = 0.750$ m^2/s) is injected into the river model. The model shows the concentration distribution over time observed at three locations ($x = 40$ m, $x = 60$ m, and $x = 80$ m). This is compared to the analytical solution.

B

dMSCC device geometries

The geometries of the wafer designs and the models were made with AutoCAD and their dimensions are given in the Figures below.

(a) Wafer design in AutoCAD.

(b) Dimensions of the inlets of the base case design with 500 μm spacing between the μCGG outlets.
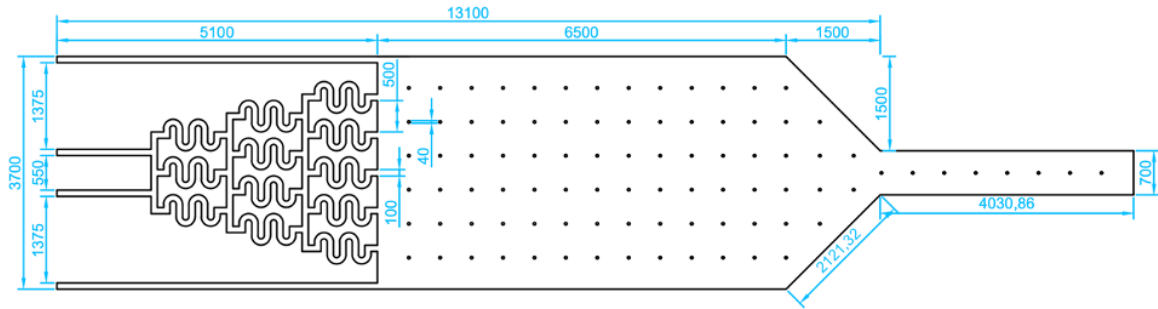
(c) Dimensions of the base case design with 500 μm spacing between the μCGG outlets.
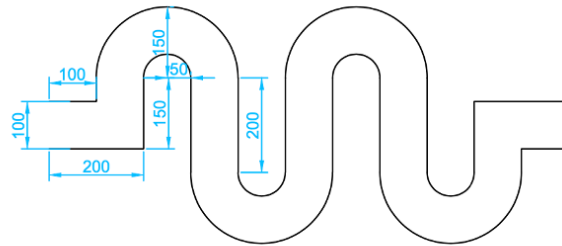
(d) Dimensions of the round bends.
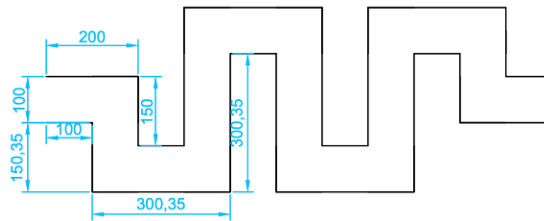
(e) Dimensions of the square bends.
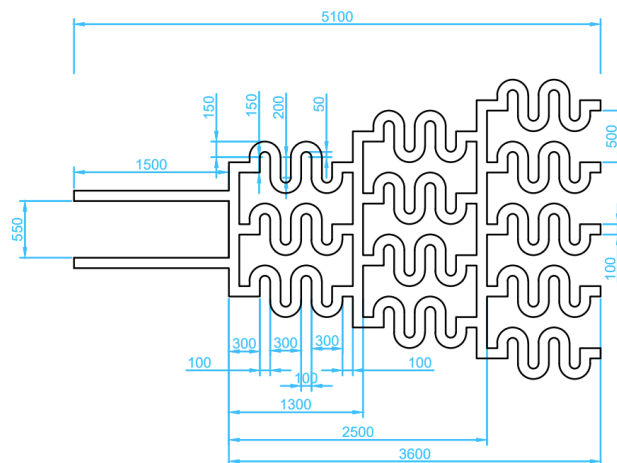
(f) Dimensions of the μCGG model with round bends.

(g) Dimensions of the design with 500 μm spacing between the μCGG outlets, but with square bends.

(h) Dimensions of the design with 500 μm spacing between the μCGG outlets, but with a short chamber.

(i) Dimensions of the design with 750 μm spacing between the μCGG outlets.
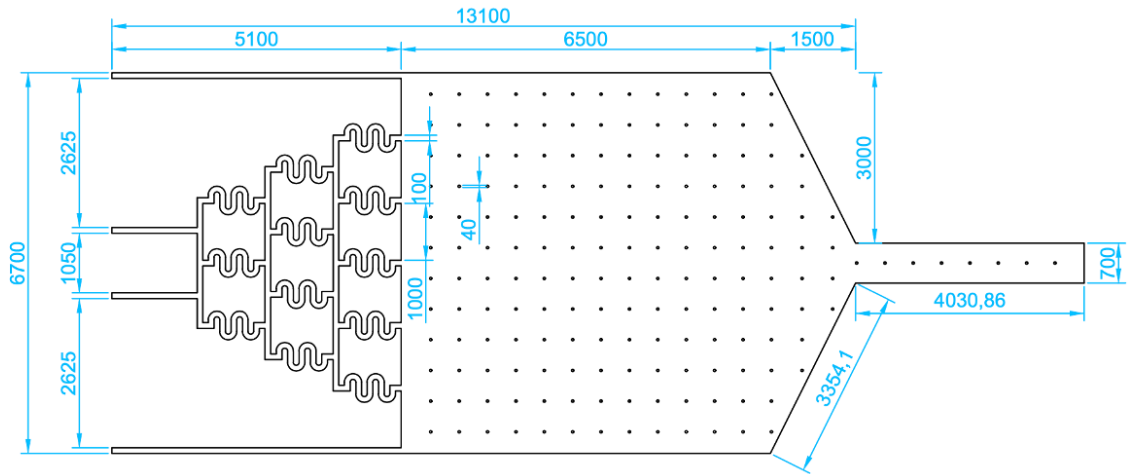
(j) Dimensions of the design with 1000 μm spacing between the μCGG outlets.
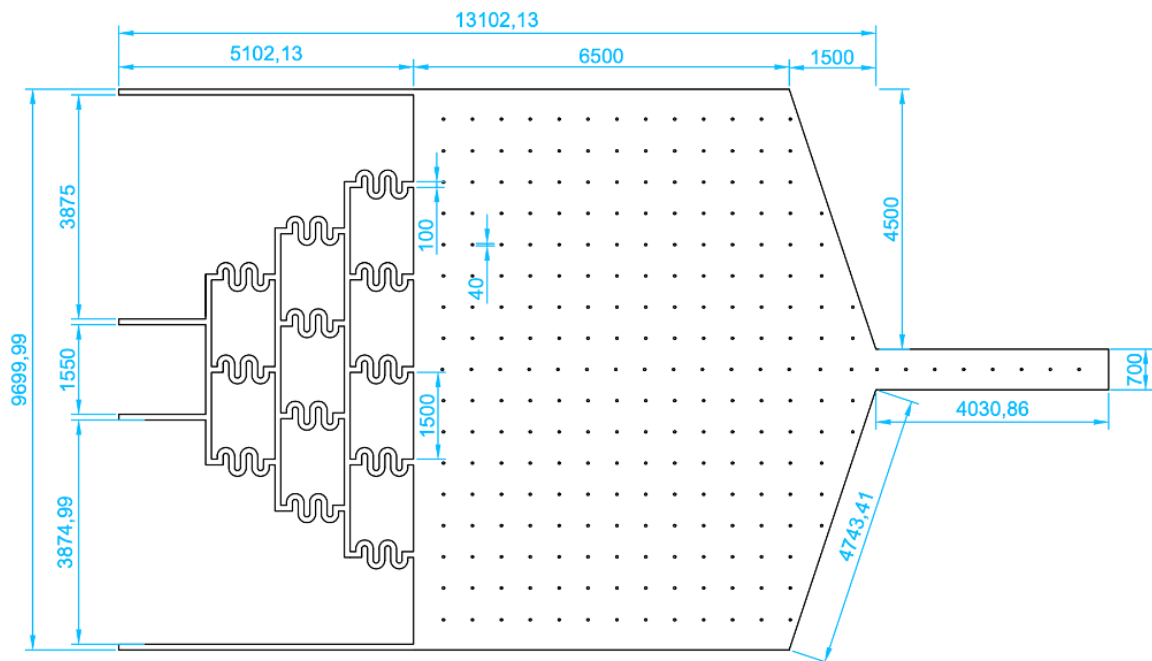
(k) Dimensions of the design with 1500 μm spacing between the μCGG outlets.

Figure B.1: Dimensions of all the different geometries used and referred to in this thesis, either for computational or laboratory work. The geometry dimensions are given in μm.

C
Source Code

C.1. Characteristic times
This is the source code for the characteristic time calculations in chapter 2.

```python
1  #%%
2  #Import libraries
3  import numpy as np
4  import matplotlib.pyplot as plt
5  from scipy.interpolate import interp1d
6
7  #Plot settings
8  colourTU= '#0C2340', '#00B8C8', '#0076C2', '#6F1D77', '#EF60A3', '#A50034', '#E03C31', '#
       EC6842', '#FFB81C', '#6CC24A', '#009B77'
9  plt.rcParams['lines.linewidth'] = 1
10 plt.rcParams.update({'font.size': 12})
11 #%%
12 #Characteristic time diffusion (penetration theory for diffusion):
13 def chartime_diffusion(delta, D):
14     t_diff = delta**2/ (np.pi*D)
15     return t_diff
16
17 #Set parameters
18 D_gluc = 6e-10 #m2/s (diffusion coefficient glucose in water at room temp, Ho et al. 2019)
19 d, dx = 200e-6, 1e-7 #max penetration depth, number of steps
20 delta = np.arange(0, d, dx) #m (range of penetration depths) (may also be a single value)
21
22 #Calculate characteristic time
23 t_diff = chartime_diffusion(delta, D_gluc)
24
25 #Calculate intersection
26 delta0 = np.sqrt(1*np.pi*D_gluc)*1e6
27 print(f'The penetration depth should be < {delta0:.6f} um to keep the characteristic time
       below 1 second.')
28
29 #Plot
30 fig, ax = plt.subplots()
31 ax.plot(delta*1e6, t_diff, color=colourTU[2])
32 ax.hlines(1, 0, d*1e6, 'grey', '--')
33 ax.set_xlabel('Penetration depth ($\mu$m)')
34 ax.set_ylabel('Characteristic time diffusion (s)')
35
36 #%%
37 #Characteristic time substrate consumption:
38 def chartime_consumption(d_cs, rs_max):
39     ts_conversion = d_cs / rs_max
40     return ts_conversion
41
42 #Set parameters
43 MW_gluc = 180.156 #g/mol
44 cs = np.linspace(0, 200, 2000)  #mmol/L (max change in concentration, Ho et al. 2019)
45 km = 10**-1*MW_gluc              #g/g/s --> mmol/L/s (NMMST, maximum rate coefficient)
46 rs_max = km                      #Monod equation to calculate rate
47
```

```
48  #Calculate characteristic time:
49  ts_conversion = chartime_consumption(cs, rs_max) #s
50
51  #Plot
52  fig2, ax2 = plt.subplots()
53  ax2.plot(cs, ts_conversion, color=colourTU[2])
54  ax2.set_xlabel('$\Delta$ c$_s$ (mmol/L)')
55  ax2.set_ylabel('Characteristic time consumption (s)')
56
57  #%%
58  #Characteristic time convection (Heijen et al. 2015):
59  def chartime_convection(L, u):
60      t_conv = L / u
61      return t_conv
62
63  #Set parameters
64  L = np.linspace(0, 1000/1e6, 1000+1) #m
65  u = [1e-2, 6.66e-3, 1e-3] #m/s
66
67  #Calculate characteristic times for convection (for all three velocities)
68  t_conv = np.zeros((np.size(u), np.size(L)))
69  for i in range(len(u)):
70      t_conv[i] = chartime_convection(L, u[i])
71
72  #Plot
73  fig3, ax3 = plt.subplots()
74  ax3.plot(L*1e6, t_conv[0,:], '-', color=colourTU[2], label=f'u = {u[0]:.2e} $\mu$m/s')
75  ax3.plot(L*1e6, t_conv[1,:], '-', color=colourTU[5], label=f'u = {u[1]:.2e} $\mu$m/s (Ho et
        al., 2019)')
76  ax3.plot(L*1e6, t_conv[2,:], '-', color=colourTU[8], label=f'u = {u[2]:.2e} $\mu$m/s')
77  ax3.legend()
78  ax3.set_xlabel('Length of channel ($\mu$m)')
79  ax3.set_ylabel('Characteristic time convection (s)')
80  ax3.set_ylim(-0.1,1.35)
81
82  # %%
83  #Calculate characteristic time axial dispersion
84  def chartime_axialdispersion(L, u, Dm, dH):
85
86      t_conv = chartime_convection(L,u)          #Calculate characteristic time convection
87      D_ax = Dm + (u**2 * dH**2)/(192 * Dm)      #Calculate axial dispersion coefficient
88      L_plug = np.sqrt(np.pi*D_ax*t_conv)        #Calculate smearing distance
89      t_ax = L_plug / u                          #Calculate characteristic time axial dispersion
90
91      return L_plug, t_ax, t_conv
92
93  #Set parameters:
94  dH = np.linspace(0,250*1e-6,250+1)
95  R = 0.5*dH
96  pi = np.pi
97  u = [1e-2, 6.66e-3, 1e-3] #m/s
98  L = 1000e-6
99  Dm = 6e-10 #m2/s (glucose in water)
100
101 L_plug = []
102 t_ax = []
103 t_conv2 = []
104
105 for i in range(len(u)):
106     L_plug1, t_ax1, t_conv1 = chartime_axialdispersion(L, u[i], Dm, dH)
107     L_plug.append(L_plug1)
108     t_ax.append(t_ax1)
109     t_conv2.append(t_conv1)
110
111 fig4, ax4 = plt.subplots()
112 ax4.plot(dH*1e6, t_ax[0], color=colourTU[2], label=f'u = {u[0]:.2e} $\mu$m/s')
113 ax4.plot(dH*1e6, t_ax[1], color=colourTU[5], label=f'u = {u[1]:.2e} $\mu$m/s (Ho et al.,
        2019)')
114 ax4.plot(dH*1e6, t_ax[2], color=colourTU[8], label=f'u = {u[2]:.2e} $\mu$m/s')
115 ax4.legend()
116 ax4.set_ylabel('Characteristic time axial dispersion (s)')
```

```
117 ax4.set_xlabel('Hydraulic diameter ($\mu$m)')
118
119 #%%
120 #Calculate Reynolds number
121 def Reynolds(rho, u, mu, dH):
122     Re = (rho * u * dH)/mu
123     return Re
124
125 #Set parameters
126 u_lin = np.linspace(0, 1E-2, 1000+1)
127 dH_const = 100E-6
128 dH_lin = np.linspace(0, 250E-6, 250+1)
129 u_const = 6.66E-3
130
131 rho = 1000 #kg/m3, water 20C
132 mu = 1e-3 #Pa s (N/m2), water 20C
133
134 #Calculate Reynolds numbers
135 Re_u = Reynolds(rho, u_lin, mu, dH_const)
136 Re_dH = Reynolds(rho, u_const, mu, dH_lin)
137
138
139 #Plots
140 fig5, ax5 = plt.subplots()
141 ax5.plot(dH_lin*1e6, Re_dH, color=colourTU[2])
142 ax5.set_ylabel('Reynolds number')
143 ax5.set_xlabel('Hydraulic diameter ($\mu$m)')
144
145 fig6, ax6 = plt.subplots()
146 ax6.plot(u_lin, Re_u, color=colourTU[2])
147 ax6.set_ylabel('Reynolds number')
148 ax6.set_xlabel('Fluid velocity (m/s)')
149 ax6.set_ylim(-0.1,1.599)
```

C.2. 1D time-dependent convection-dispersion model

This is the source code for the 1D convection-dispersion model used in the time-scale exploration study (chapter 2).

```
1  # Import libraries
2  import numpy as np
3  import matplotlib.pyplot as plt
4  import scipy.integrate as spi
5  from scipy.interpolate import interp1d
6
7  # Plot settings
8  plt.rcParams['lines.linewidth'] = 1
9  plt.rcParams.update({'font.size': 12})
10
11 colourTU= '#0C2340', '#00B8C8', '#0076C2', '#6F1D77', '#EF60A3', '#A50034', '#E03C31', '#
       EC6842', '#FFB81C', '#6CC24A', '#009B77'
12 colorTU_new = [colourTU[2], colourTU[5], colourTU[8], colourTU[10], colourTU[4], colourTU[0],
        colourTU[7], colourTU[1]]
13
14 # PDE function
15 def funpde(t,C): # System of partial differential equations
16
17     # Variables definition
18     dcdt    = np.zeros(p)
19
20     # --- Boundary conditions ---
21     #Inlet concentration
22     c_in = phi_0(t)
23     # Mobile phase boundary conditions @ x = 0
24     C[0] = (u*h/D)*(c_in+ D/u/h*C[1] - C[1])
25     # Mobile phase boundary conditions @ x = L
26     C[p-1] = C[p-2]
27
28     # --- Time stepping ---
29     for i in range(1,p-1):   # only internal points 1..p-2 (without boundary points)
```

```python
30          # Discretized PDE (Finite Differences)
31          dcdt[    i] = D*(C[    i+1]-2*C[    i]+C[    i-1])/h/h - u*(C[    i]-C[    i-1])/h
32
33      return dcdt
34
35  # Set parameters
36  M = 1e-9        # kg
37  D = 3E-10       # m2/s
38  u = 6.66E-3     # m/s
39  L = 1000E-6     # m
40  A = 5000E-6     #m2
41  MW_gluc = 0.180 #kg/mol
42
43  # Time scale settings
44  ti = 0.0001     # s
45  tf = 0.3  # s
46  dt = 0.0001     # s
47  ts = np.linspace(ti, tf, int((tf-ti)/dt+1)) #s
48
49  dx = np.array((2e-6, 50e-6, 100E-6, 250E-6, 500E-6, 750E-6, 1000E-6))#, 43, 44, 45, 50, 60,
        70, 80))
50
51  # Taylor solution (analytical) (Silavwe et al. 2019)
52  phi = np.zeros((np.size(dx), np.size(ts)))
53  for i in range(len(dx)):
54      phi[i] = M / (A*np.sqrt(4*np.pi*D*ts)) * np.exp(-(dx[i]-u*ts)**2/(4*D*ts))
55
56  # Plot Taylor solution
57  fig, ax = plt.subplots()
58  for i in range(len(dx)):
59      ax.plot(ts, phi[i]/MW_gluc, '-', label=f'x={dx[i]*1e6}$\mu$m', color=colorTU_new[i])
60  ax.set_xlabel('Time (s)'); ax.set_ylabel('Concentration phi (mol/m$^3$)')
61  ax.legend()
62
63  # Set parameters for solving the PDE system
64  # Initial concentrations
65  CA_0_x = 0                  # mol/m3
66
67  # Inlet concentrations
68  Cin_A = 200                 # mol/m3 (mM)
69  c_s_in = Cin_A
70
71  # Meshing
72  n = 100                     # Number of intervals
73  p = n+1                     # Nodes
74  h = L/n                     # Mesh size
75  x = np.linspace(0,L,n+1)
76
77  # Set the initial conditions
78  CA = np.zeros(p) + CA_0_x   # mol/m3
79  iv = CA
80
81  # Inlet concentration (Taylor solution at x=2um from Silavwe et al. 2019)
82  phi_0_arr = np.array(phi[0,:])
83  phi_0 = interp1d(ts, phi_0_arr)
84
85  # Solver
86  sol2 = spi.solve_ivp(funpde, [ti,tf], iv, t_eval=ts, rtol=1e-12, atol=1e-12, method='Radau')
87
88  # Retrieve solutions
89  t2 = sol2.t
90  CA = sol2.y
91
92  # Plot model data
93  fig2, ax2 = plt.subplots()
94
95  ax2.plot(t2,CA[10,:]/MW_gluc,'-', color=colourTU[2], label='x=100$\mu$m simulated')
96  ax2.plot(t2,CA[25,:]/MW_gluc,'-', color=colourTU[5], label='x=250$\mu$m simulated')
97  ax2.plot(t2,CA[50,:]/MW_gluc,'-', color=colourTU[8], label='x=500$\mu$m simulated')
98  ax2.plot(t2,CA[75,:]/MW_gluc,'-', color=colourTU[10], label='x=750$\mu$m simulated')
99  ax2.plot(t2,CA[p-1,:]/MW_gluc,'-', color=colourTU[4], label='x=1000$\mu$m simulated')
```

```
100
101 ax2.legend()
102 ax2.set_xlabel('Time (s)')
103 ax2.set_ylabel('Concentration (mol/m3)')
```

The following is the source code for the verification of the 1D time-dependent convection-dispersion model as discussed in Appendix A.

```
1  #%%
2  #Import libraries
3  import numpy as np
4  import matplotlib.pyplot as plt
5  import scipy.integrate as spi
6  from scipy.interpolate import interp1d
7
8  # Plot settings
9  plt.rcParams['lines.linewidth'] = 1
10 plt.rcParams.update({'font.size': 12})
11
12 colourTU= '#0C2340', '#00B8C8', '#0076C2', '#6F1D77', '#EF60A3', '#A50034', '#E03C31', '#
       EC6842', '#FFB81C', '#6CC24A', '#009B77'
13 colorTU_new = [colourTU[2], colourTU[5], colourTU[8], colourTU[10], colourTU[4], colourTU[0],
        colourTU[7], colourTU[1]]
14
15 # PDE function
16 def funpde(t,C): # System of partial differential equations
17
18     # Variables definition
19     dcdt    = np.zeros(p)
20
21     # --- Boundary conditions ---
22     #Inlet concentration
23     c_in = phi_0(t)
24     # Mobile phase boundary conditions @ x = 0
25     C[0] = (u*h/D)*(c_in+ D/u/h*C[1] - C[1])
26     # Mobile phase boundary conditions @ x = L
27     C[p-1] = C[p-2]
28
29     # --- Time stepping ---
30     for i in range(1,p-1):    # only internal points 1..p-2 (without boundary points)
31         # Discretized PDE (Finite Differences)
32         dcdt[    i] = D*(C[    i+1]-2*C[    i]+C[    i-1])/h/h - u*(C[    i]-C[    i-1])/h
33
34     return dcdt
35
36 # Taylor solution (analytical) (Silavwe et al. 2019)
37 # Set parameters
38 M = 1 #kg/m2
39 # Kinetic parameters Silavwe et al. 2019
40 D = 0.750               # m2/s
41 u = 0.225               # m/s
42 L = 40                  # m
43 A = 1 #m2
44
45 # Time scale settings
46 ti = 0.001      # s
47 tf = 5000  # s
48 dt = 1     # s
49 ts = np.linspace(ti, tf, int((tf-ti)/dt+1)) #s
50
51 # Distances
52 dx = np.array((40, 50, 60, 70, 80))
53
54 # Taylor solution (analytical) (Silavwe et al. 2019)
55 phi = np.zeros((np.size(dx), np.size(ts)))
56 for i in range(len(dx)):
57     phi[i] = M / (A*np.sqrt(4*np.pi*D*ts)) * np.exp(-(dx[i]-u*ts)**2/(4*D*ts))
58
59
60 fig, ax = plt.subplots()
61 for i in range(len(dx)):
```

```python
62      ax.plot(ts, phi[i]*1e6, '-', label=f'x={dx[i]}m', color=colorTU_new[i])

64  ax.set_xlabel('Time (s)'); ax.set_ylabel('Concentration phi ($\mu$g/L)')
65  ax.legend()

67  # Set parameters for solving the PDE system
68  # Initial concentrations
69  CA_0_x = 0                  # mol/m3

71  # Inlet concentrations
72  Cin_A = 200                 # mol/m3 (mM)
73  c_s_in = Cin_A

75  # Meshing
76  n = 40                      # Number of intervals
77  p = n+1                     # Nodes
78  h = L/n                     # Mesh size
79  x = np.linspace(0,L,n+1)

81  # Set the initial conditions
82  CA = np.zeros(p) + CA_0_x   # mol/m3
83  iv = CA

85  # Inlet concentration (Taylor solution at x=2um from Silavwe et al. 2019) & Taylor solutions
        for plotting
86  phi_40_arr = np.array(phi[0,:])
87  phi_40 = interp1d(ts, phi_40_arr)
88  phi_0 = phi_40

90  phi_80_arr = phi[-1,:]
91  phi_80 = interp1d(ts, phi_80_arr)

93  phi_60_arr = phi[2,:]
94  phi_60 = interp1d(ts, phi_60_arr)

96  # Solver
97  sol2 = spi.solve_ivp(funpde, [ti,tf], iv, t_eval=ts, rtol=1e-8, atol=1e-8, method='Radau')

99  # Get solutions
100 t2 = sol2.t
101 CA3 = sol2.y[0,  :]      #x=40m
102 CA4 = sol2.y[21, :]      #x=60m
103 CA2 = sol2.y[p-1, :]     #x=80m

105 # Plot model results
106 fig2, ax2 = plt.subplots()
107 ax2.plot(ts, phi_40(ts)*1e3, color=colourTU[2], label='x=40m synthetic')
108 ax2.plot(t2,CA3*1e3,'--', color=colourTU[2], label='x=40m simulated')
109 ax2.plot(ts, phi_60(ts)*1e3, color=colourTU[5], label='x=60m synthetic')
110 ax2.plot(t2,CA4*1e3,'--', color=colourTU[5], label='x=60m simulated')
111 ax2.plot(ts, phi_80(ts)*1e3, '-', color=colourTU[8], label='x=80m synthetic')
112 ax2.plot(t2,CA2*1e3,'--',color=colourTU[8], label='x=80m simulated')
113 ax2.set_xlim(0, 1000)
114 ax2.legend()
115 ax2.set_xlabel('Time (s)')
116 ax2.set_ylabel('Concentration (g/m3)')

118 #Calculate SSE:
119 phi_stack = np.vstack((phi_40_arr[0:1000], phi_60_arr[0:1000], phi_80_arr[0:1000]))
120 CA_stack = np.vstack((CA3[0:1000], CA4[0:1000], CA2[0:1000]))
121 phi_40_60_80 = phi_stack
122 CA_40_60_80 = CA_stack
123 SSE = (phi_40_60_80-CA_40_60_80)**2
124 SSE = np.sum(SSE)
125 dx = L/n
126 print(f'The SSE using dx={dx}m = {SSE:.3e}.')
```

C.3. Stationary and time-dependent studies

The following source code was used to interpolate the data of the stationary parametric sweep and generate the step and sine functions respectively.

```python
#%%
import numpy as np
import matplotlib.pyplot as plt
from scipy.interpolate import interp1d
colourTU= '#0C2340', '#00B8C8', '#0076C2', '#6F1D77', '#EF60A3', '#A50034', '#E03C31', '#
    EC6842', '#FFB81C', '#6CC24A', '#009B77'

t2 = np.array((0, 80, 110, 140, 170, 200, 230, 260, 290, 320, 350, 380, 410, 440, 470, 500,
    530, 560, 590))
c2 = np.array((0, 0,   50, 100, 150, 200, 100,   0,  75, 150, 125, 100,   0, 200,   0, 100,
    110, 100,  90))

tf = np.linspace(0,590, 5901)
step_fun = interp1d(t2, c2, kind='next')
c3 = step_fun(tf)

#Plot input
fig, ax = plt.subplots()
ax.plot(tf, c3, '-', color=colourTU[2])
ax.set_xlabel('Time (s)'); ax.set_ylabel('Concentration (mol/m$^3$)')

stepdata = np.vstack((tf, c3))
# stepdata = stepdata.T
#%%
np.savetxt('stepdata_final.txt', stepdata)
# %%
# df = np.loadtxt('max_velocity_study_data_c.txt', comments='%')
df = np.loadtxt('Parametric_sweep-conc_vs_ratio_3.txt', comments='%')
ratio_u1u2 = df[:,0]
c = df[:,1]
f_s = interp1d(ratio_u1u2, c, kind='linear')
f_s2 = interp1d(c, ratio_u1u2, fill_value='extrapolate', kind='linear')

ratio = f_s2(c3)


fig2, ax2 = plt.subplots()
ax2.plot(tf, ratio, color=colourTU[2])
ax2.set_yscale('log')
ax2.set_xlabel('Time (s)'); plt.ylabel('Ratio u1/u2')

fig3, ax3 = plt.subplots()
ax3.plot(ratio_u1u2, c, '.', color=colourTU[1], label='Model data')
ax3.plot(ratio_u1u2, f_s(ratio_u1u2), '--', color=colourTU[5], label='Linear interpolation
    function')
ax3.set_xscale('log')
ax3.set_ylabel('Concentration (mol/m$^3$)');plt.xlabel('Ratio u1/u2')

RatioDataSet = np.vstack((tf, ratio))
RatioDataSet = RatioDataSet.T
# %%
np.savetxt('ratio_step_data_final.txt', RatioDataSet)
```

```python
#%%
#Import libraries
import numpy as np
import matplotlib.pyplot as plt
from scipy.interpolate import interp1d
colourTU= '#0C2340', '#00B8C8', '#0076C2', '#6F1D77', '#EF60A3', '#A50034', '#E03C31', '#
    EC6842', '#FFB81C', '#6CC24A', '#009B77'

#%%
#The input used by Ho et al. 2019
pi = np.pi
f = 20 #Hz (between 100 and 0.001)
t = np.linspace(0, 100, 1000) #s
```

```python
13  c_s_in = np.array( 200 * ((1/2) * np.sin(2*pi*f*t-(pi/2)) + 1/2) )#mmol/L
14
15  #Get initialization time
16  t2 = np.array((0, 80))
17  c2 = np.array((0, 0))
18
19  tf = np.linspace(0,80, 801)
20  step_fun = interp1d(t2, c2, kind='next')
21  c3 = step_fun(tf)
22
23  #Add initialization phase to the sinus input
24  t_new = np.linspace(0, 180, 1801)
25  c_new = np.hstack((c3, c_s_in))
26
27  #Plot input
28  fig, ax = plt.subplots
29  ax.plot(t_new, c_new, color=colourTU[2])
30  ax.set_xlabel('Time (s)'); ax.set_ylabel('Concentration (mol/m$^3$)')
31
32  #Get parametric sweep data
33  df = np.loadtxt('Parametric_sweep-conc_vs_ratio_3.txt', comments='%')
34  ratio_u1u2 = df[:,0]
35  c = df[:,1]
36
37  #Interpolate the data
38  f_s = interp1d(ratio_u1u2, c, kind='linear')
39  f_s2 = interp1d(c, ratio_u1u2, fill_value='extrapolate', kind='linear')
40
41  #Plot interpolation data
42  fig2, ax2 = plt.subplots()
43  ax2.plot(ratio_u1u2, c, '.', color=colourTU[2], label='Model data')
44  ax2.plot(ratio_u1u2, f_s(ratio_u1u2), '--', color=colourTU[5], label='Linear interpolation
        function')
45  ax2.xscale('log')
46  ax2.ylabel('Concentration (mol/m$^3$)');plt.xlabel('Ratio u1/u2')
47
48  #Get the desired ratio over time
49  ratio = f_s2(c_new)
50
51  #plot the ratio over time
52  fig3, ax3 = plt.subplots()
53  ax3.plot(t_new, ratio, color=colourTU[2])
54  ax3.set_yscale('log')
55  ax3.set_xlabel('Time (s)'); ax3.set_ylabel('Ratio u1/u2')
56  # %%
57  RatioDataSet = np.vstack((t_new, ratio))
58  RatioDataSet = RatioDataSet.T
59  # %%
60  np.savetxt('ratio_sin_data_final.txt', RatioDataSet)
61  # %%
```

C.4. Data analysis Ansys mixer DoE - 2D interpolation

```python
1   import numpy as np
2   import matplotlib.pyplot as plt
3   from scipy.interpolate import griddata
4   import pandas as pd
5
6
7   #Import raw data
8   df = pd.read_csv(r'design_points_2.csv', header=2)
9   df = np.array(df)
10
11  df2 = pd.read_csv(r'design_points_4.csv', header=2)
12  df2 = np.array(df2)
13
14  #New data frames for data conversions of raw data
15  df1 = df
16  df3 = df2
```

```python
17
18  #Data conversions to match points; UDS = user-defined scalar
19  #design points 4:
20  for i in range(len(df2[:,0])):
21      df3[i,1] = 10**(df2[i,1])          #u = exponent
22      df3[i,2] = 10**(df2[i,2])/1000     #D = gamma/rho; rho=1000; gamma = UDS
23
24  #design points 2:
25  for i in range(len(df[:,0])):
26      df1[i,3] = 1/df[i,3]               #Normalize output
27      df1[i,2] = df[i,2]/1000            #D = gamma/rho; rho=1000; gamma = UDS
28
29
30  #add the data points together
31  df_total = np.vstack((df1, df3))
32
33  x = df_total[:,1]; y = df_total[:,2]; z = df_total[:,3]
34
35  #Function interpolation
36  def interpolate_logspace(x, y, z, x_new, y_new):
37      # Convert data to logarithmic scale
38      x_log = np.log10(x)
39      y_log = np.log10(y)
40      z_log = np.log10(z)
41
42      # Create a grid for interpolation
43      xi, yi = np.meshgrid(np.log10(x_new), np.log10(y_new))
44
45      # Perform linear interpolation in logarithmic space
46      zi_log = griddata((x_log, y_log), z_log, (xi, yi), method='nearest')
47
48      # Convert interpolated values back to linear scale
49      zi = 10 ** zi_log
50
51      return zi, x_log, y_log
52
53  #Get new x, y space for interpolation function
54  x_new = np.linspace(min(x), max(x), num=100)
55  y_new = np.linspace(min(y), max(y), num=100)
56
57  #Call 2d interpolation function
58  zi, x_log, y_log = interpolate_logspace(x, y, z, x_new, y_new)
59
60  #Plot data linear space (log axis)
61  plt.rcParams['lines.linewidth'] = 1
62  fig, ax1 = plt.subplots()
63  plot = ax1.pcolormesh(x_new, y_new, zi, shading='auto', cmap='Spectral', vmin = min(z), vmax
        = max(z))
64  ax1.scatter(x, y, color='k', marker='.', s=2)
65  ax1.set_xscale('log'); ax1.set_yscale('log')
66  ax1.set_xlabel('Velocity (m/s)');ax1.set_ylabel('Diffusion coefficient (m$^2$/s)')
67  fig.colorbar(plot, ax=ax1)
68
69  #Plot data log space (linear axis)
70  plt.rcParams['lines.linewidth'] = 1
71  fig, ax1 = plt.subplots()
72  plot = ax1.pcolormesh(np.log10(x_new), np.log10(y_new), zi, shading='auto', cmap='Spectral',
        vmin = min(z), vmax = max(z))
73  ax1.scatter(x_log, y_log, color='k', marker='.', s=2)
74  # ax1.set_xscale('log'); ax1.set_yscale('log')
75  ax1.set_xlabel('log10(u)');ax1.set_ylabel('log10(D)')
76  fig.colorbar(plot, ax=ax1)
```

Mesh independence study
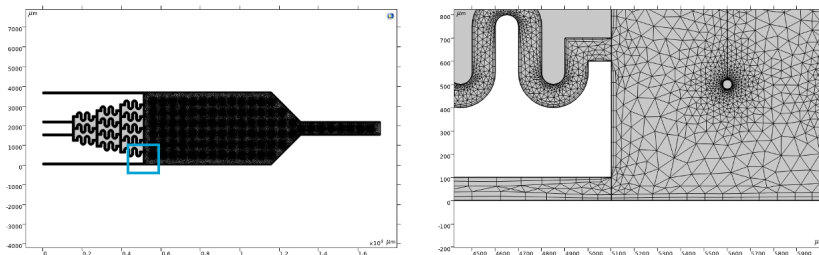
(a) Coarse mesh.
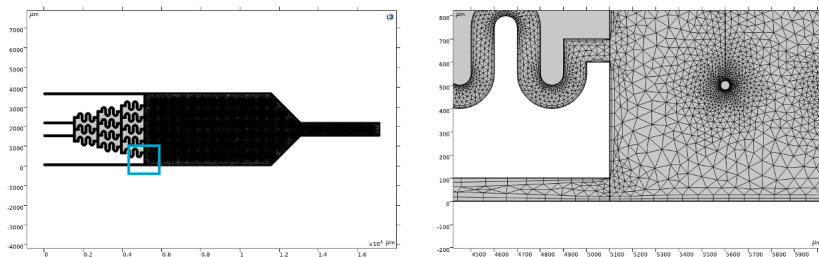
(b) Normal mesh.
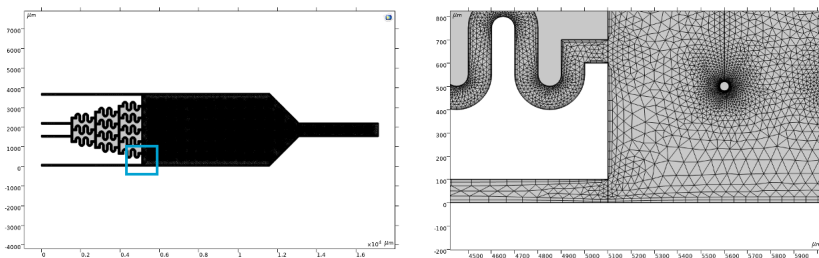
(c) Fine mesh.
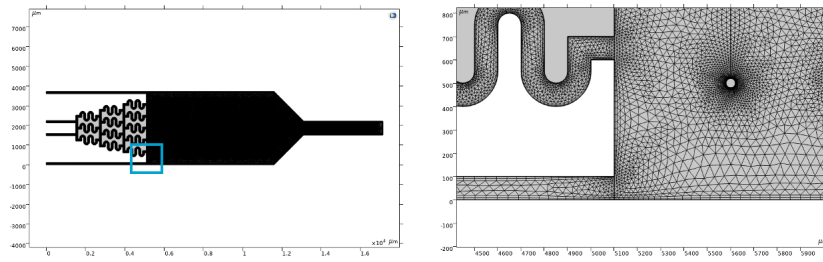
(d) Finer mesh.

Figure D.1: Overview of the different meshes used in the mesh independence study. Each subfigure shows the mesh across the entire domain and an enlarged section (indicated with a blue square) that shows the elements within the mesh with greater detail. The element sizes can be found in the Materials and Methods (section 3).
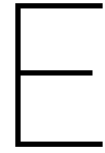
Complete step and sine function

The step function used in the time dependent study is described by equation E.1:

$$
\begin{cases}
c = 0 \ mol/m^3 & 0 \le t < 80 \ s \\
c = 50 \ mol/m^3 & 80 \le t < 110 \ s \\
c = 100 \ mol/m^3 & 110 \le t < 140 \ s \\
c = 150 \ mol/m^3 & 140 \le t < 170 \ s \\
c = 200 \ mol/m^3 & 170 \le t < 200 \ s \\
c = 100 \ mol/m^3 & 200 \le t < 230 \ s \\
c = 0 \ mol/m^3 & 230 \le t < 260 \ s \\
c = 75 \ mol/m^3 & 260 \le t < 290 \ s \\
c = 150 \ mol/m^3 & 290 \le t < 320 \ s \\
c = 125 \ mol/m^3 & 320 \le t < 350 \ s \\
c = 100 \ mol/m^3 & 350 \le t < 380 \ s \\
c = 0 \ mol/m^3 & 380 \le t < 410 \ s \\
c = 200 \ mol/m^3 & 410 \le t < 440 \ s \\
c = 0 \ mol/m^3 & 440 \le t < 470 \ s \\
c = 100 \ mol/m^3 & 470 \le t < 500 \ s \\
c = 110 \ mol/m^3 & 500 \le t < 530 \ s \\
c = 100 \ mol/m^3 & 530 \le t < 560 \ s \\
c = 90 \ mol/m^3 & 560 \le t \le 590 \ s
\end{cases}
\tag{E.1}
$$

The sine function used in the time dependent study is described by equation E.2:

$$
\begin{cases}
c = 0 \ mol/m^3 & 0 \le t < 80 \ s \\
c = 200 \left(\frac{1}{2} \cdot sin \left(2\pi \cdot f \cdot t - \frac{\pi}{2} \right) + \frac{1}{2} \right) & 80 \le t \le 180 \ s
\end{cases}
\tag{E.2}
$$

The step function used in the time dependent study with the adjusted geometry with a chamber width of 1300 μm is described by equation E.3:

$$
\begin{cases}
c = 0 \ mol/m^3 & 0 \le t < 8 \ s \\
c = 50 \ mol/m^3 & 8 \le t < 12 \ s \\
c = 0 \ mol/m^3 & 12 \le t < 16 \ s \\
c = 50 \ mol/m^3 & 16 \le t < 20 \ s \\
c = 100 \ mol/m^3 & 20 \le t < 24 \ s \\
c = 150 \ mol/m^3 & 24 \le t < 28 \ s \\
c = 100 \ mol/m^3 & 28 \le t < 32 \ s
\end{cases}
\tag{E.3}
$$

F
Experimental set-up

F.1. Overview of the experimental set-up
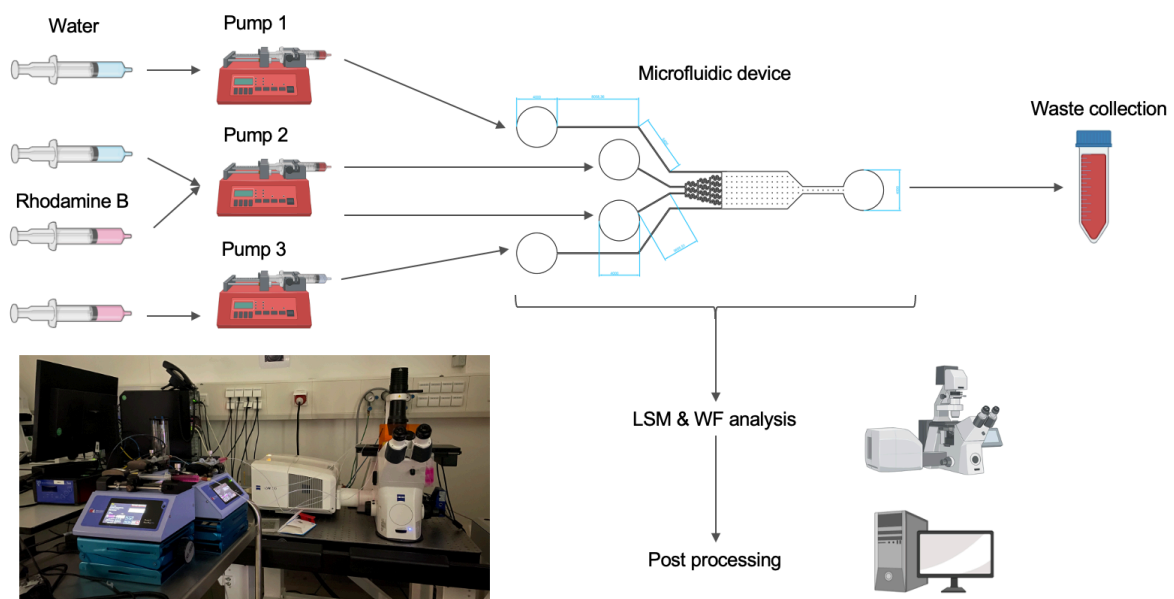
Figure F.1: Schematic overview of the experimental set-up. One syringe filled with water is connected to pump 1, one syringe filled with water and one filled with rhodamine B is connected to pump 2, and one syringe filled with rhodamine B is connected to pump 3. The pumps are connected to the four inlets of the chip. The outlet is connected to a waste collection tube. A Zeiss laser scanning microscope is used for imaging and ZEN Blue software, Microsoft Excel and Python are used for post-processing of the data. The bottom left corner depicts the actual laboratory set-up.

F.2. Velocity calculation errors

For the experiments, the velocities used in the model base case were converted to fluxes (since the syringe pumps used were flux based). For this, equation F.1 was used. However, during these calculations, the cross-sectional area (A) of the tubing was assumed. However, there is approximately a factor 10 difference between this circular cross-section and that of the rectangular cross-section of a channel in the microfluidic device. Therefore, the velocities that were calculated were approximately a factor 10 higher than anticipated and resulted in a lack of mixing in the μCGG. An overview of this calculation difference is given in Table F.1.

$$\phi = Au \tag{F.1}$$

Table F.1: Overview of experimental velocity calculation errors. The flux was calculated using the dimensions of the tubing. However, this flux corresponds with a much higher actual velocity considering the difference between the cross-sectional area of the tubing and the microfluidic channels.

Quantity	Tubing	Microfluidic channel
H, W		$50\mu m, 100\mu m$
r	$150\mu m$	
A	$A = \pi r^2 = 7.07 \cdot 10^4 \mu m^2$	$A = HW = 5 \cdot 10^3 \mu m^2$
u (intended)	$6.66 \cdot 10^4 \mu m/s$	
ϕ	$2.8\mu L/min$	$2.8\mu L/min$
u (actual)		$9.3 \cdot 10^3 \mu m/s$

G

Animation QR codes

Animations are available for both the time-dependent study with the constant inlet velocity as well as with the changing inlet velocities according to the step and sine functions. The .gif files with the animations will be presented during the defence and can be requested with the author or Dr. Cees Haringa (after this thesis is concluded).
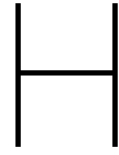
Time-dependent study - velocity

During the second time-dependent study, a step function determined the ratio of the velocities in the top and bottom inlets. This velocity change over time can be seen in the respective channels. However, in the chamber, the fluid flows come together and the difference in velocity difference disappears towards the end of the chamber. Thus, the effect of velocity changes, although minor, is only felt towards the beginning of the chamber where the gradient is pushed across up and down. This can be seen in Figure (H.1).
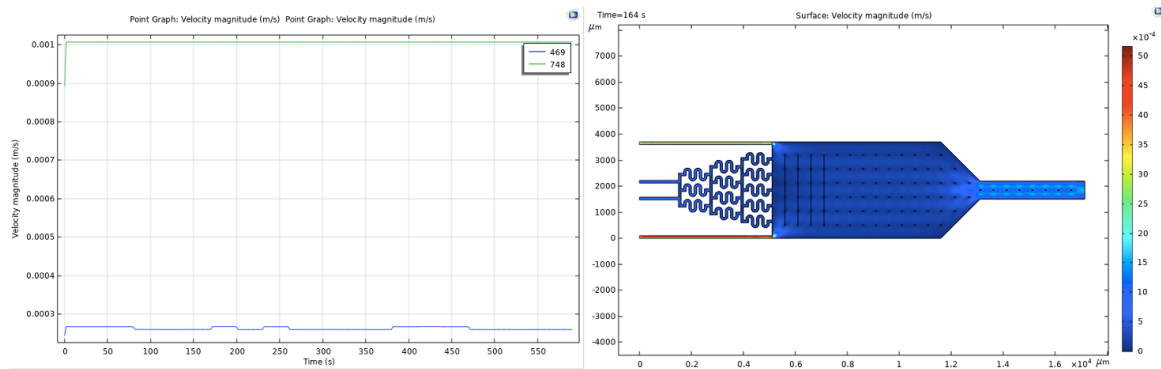
Figure H.1: The velocity in point 1 (blue) and point 2 (green) over time (left). A slight shift of the velocity in point 1 is observed as the step function changes the inlet velocities over time. This change in velocity over time is no longer observed at the end of the chamber in point 2. The surface plot of the velocity in the entire domain at t=164s (right). The high velocities in the top and bottom inlets have only a small effect on the velocity in the chamber.

μCGG velocity study

I.1. Experimental data ϕ = 1.4, 0.2, 0.05 μL/min

(a) ϕ = 1.4 μL/min; u = 4.67 $\cdot$ 10^{-3}
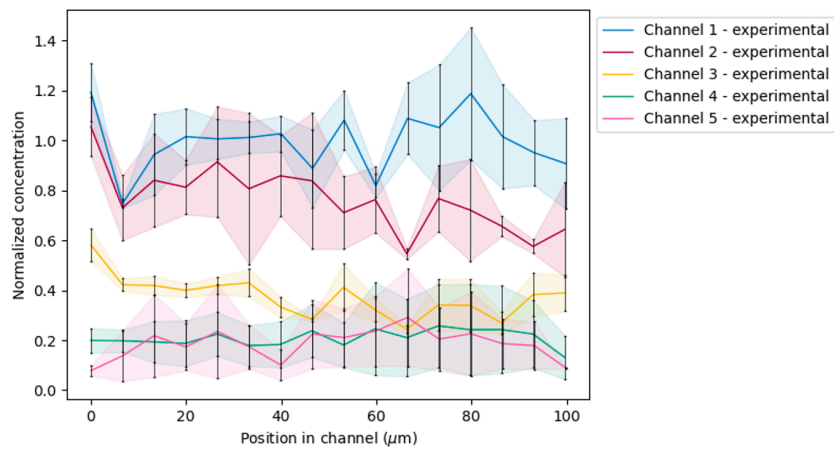
(b) ϕ = 0.2 μL/min; u = 6.67 $\cdot$ 10^{-4}
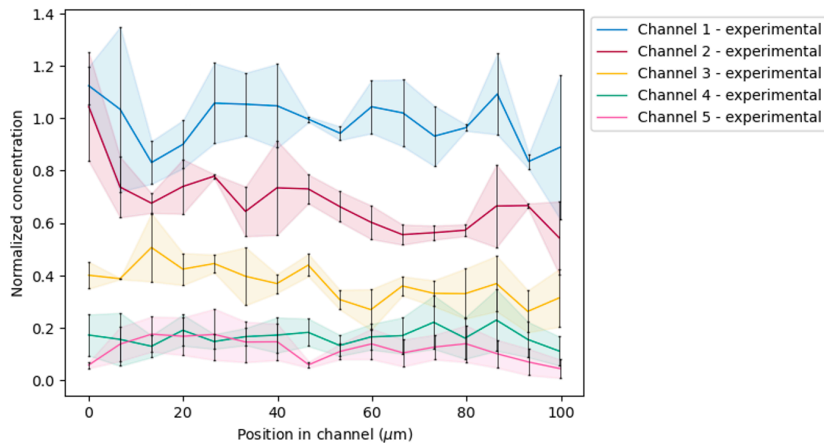
(c) ϕ = 0.05 μL/min; u = 1.67 · 10^{-4}
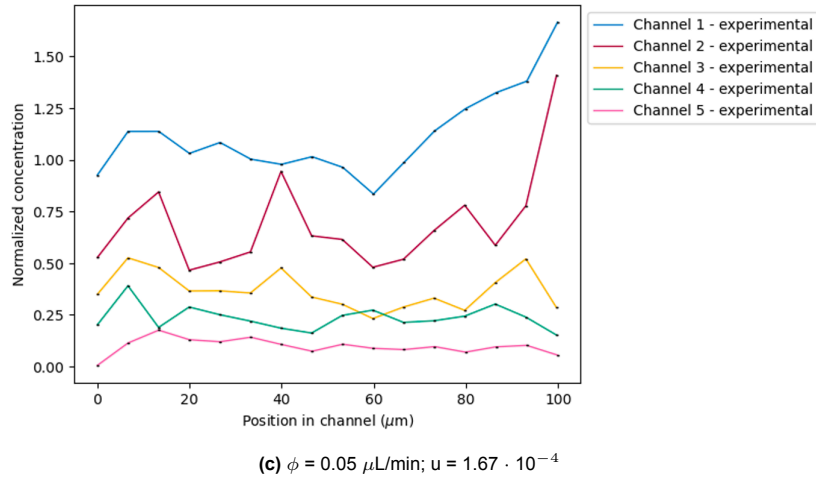
Figure I.1: Experimental data from the μCGG velocity study. The results from three out of seven examined velocities are plotted as the normalized concentration against the channel length. Note that no error region or error bars are indicated for Figure I.2c, since this measurement was accidentally not conducted in duplicate. However, results are still shown here as it falls in line with the observed trends.

I.2. Comparison model and experimental data ϕ = 1.4, 0.2, 0.05 μL/min
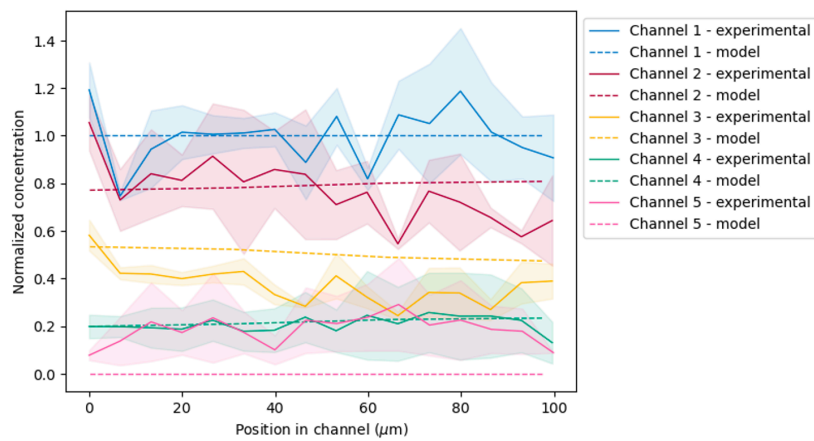
(a) ϕ = 1.4 μL/min; u = 4.67 · 10^{-3}
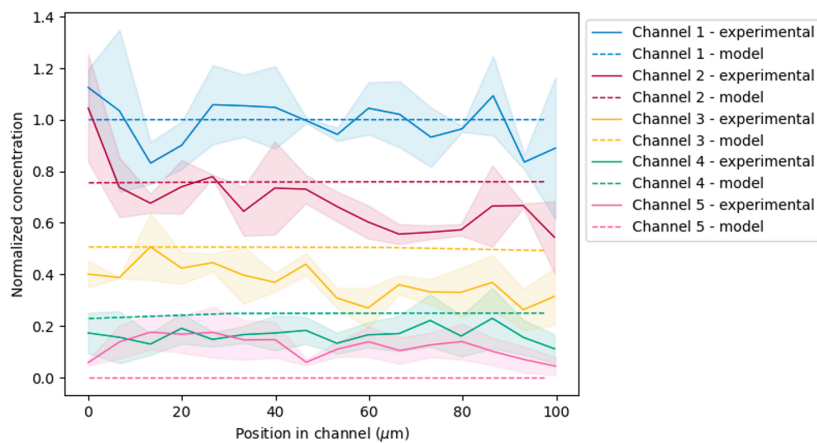
(b) ϕ = 0.2 μL/min; u = 6.67 · 10^{-4}
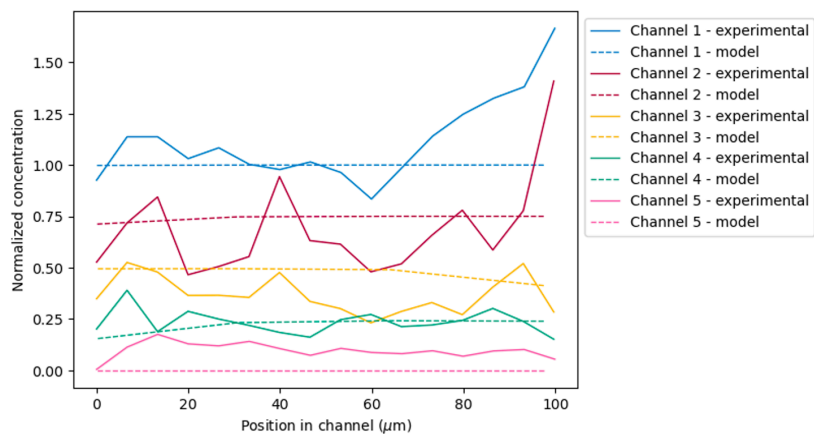
(c) ϕ = 0.05 μL/min; u = 1.67 · 10^{-4}

Figure I.2: Experimental data from the μCGG velocity study compared to the model data. The results from three out of seven examined velocities are plotted as the normalized concentration against the channel length. Note that no error regions are indicated for Figure I.2c since this measurement was accidentally not conducted in duplicate. However, results are still shown here as it falls in line with the observed trends.

J
Velocity ratio study

(a) $\phi1 = 25.2$ μL/min; $\phi1 = 2.8$ μL/min

(b) $\phi1 = 22.4$ μL/min; $\phi1 = 5.6$ μL/min

(c) $\phi1 = 19.6$ μL/min; $\phi1 = 8.4$ μL/min

(d) $\phi1 = 16.8$ μL/min; $\phi1 = 11.2$ μL/min

(e) $\phi1 = 14.0$ μL/min; $\phi1 = 14.0$ μL/min

(f) $\phi1 = 11.2$ μL/min; $\phi1 = 16.8$ μL/min

(g) $\phi 1 = 8.4$ μL/min; $\phi 1 = 19.6$ μL/min

(h) $\phi 1 = 5.6$ μL/min; $\phi 1 = 22.4$ μL/min

(i) $\phi 1 = 2.8$ μL/min; $\phi 1 = 25.2$ μL/min

Figure J.1: Ratio study